Development of a Lattice-Boltzmann model in curvilinear coordinates for the acoustic simulation of the Cochlea

Ali Mauricio Velasco Sabogal

Universidad Nacional de Colombia
Facultad de Ciencias, Departamento de Física
Bogotá, Colombia
2017

Development of a Lattice-Boltzmann model in curvilinear coordinates for the acoustic simulation of the Cochlea

Ali Mauricio Velasco Sabogal

Thesis submitted in partial fulfilment of the requirements for the degree of:
Master in science - Physics

Thesis advisor:
Dr. rer. nat. José Daniel Muñoz Castaño
Co-advisor:
PhD. Miller Mendoza Jimenez

Line of investigation:
Lattice-Boltzmann models in curvilinear coordinates.
Research Group:
Simulations of physical systems group.

Universidad Nacional de Colombia
Facultad de Ciencias, Departamento de Física.
Bogotá, Colombia
2017

Acknowledgements

Author
Ali Mauricio Velasco

Resumen

Los modelos de lattice-Boltzmann han sido una herramienta muy poderosa para simular dinámica de fluidos, difusión, ondas mecánicas y electrodinámica. Sin embargo, su aplicabilidad ha estado restringida debido a que la mayoría de ellos han sido construidos en coordenadas cartesianas, lo que les impide aprovechar las simetrías del sistema para reducir las dimensiones del dominio computacional o considerar de manera natural geometrías complejas con fronteras curvas, de las cuales la Cóclea, el órgano auditivo principal en los mamíferos, es un ejemplo paradigmático. Este trabajo diseña e implementa un modelo de lattice-Boltzmann novedoso para la simulación de ondas acústicas en coordenadas curvilíneas generales. El método mantiene en el computador la estructura estándar de un sistema cartesiano con los mismos vectores velocidad en todas las celdas, pero reescala los campos macroscópicos y añade forzamientos para reproducir en el límite continuo la ecuación de ondas en coordenadas generalizadas. El modelo de segundo orden que resulta calcula perfectamente los modos normales de vibración de un cilindro, una trompeta y un toro, mantiene en el espacio real la isotropía en la propagación de las ondas y puede ser aplicado a cualquier sistema de coordenadas. Con este método en mano se realizó la simulación de la Cóclea. Ésta fue parametrizada como un tubo de sección transversal variable en forma de cardioide que se enrolla en espiral, y fue ajustada para tener las dimensiones reales de una Cóclea humana. Como resultado, se encontró que la geometría de la Cóclea es suficiente para reproducir el efecto de separación espacial de las frecuencias. A altas frecuencias, la presión neta sobre la membrana Basilar oscila con mayor amplitud cerca de las ventanas, y frecuencias más bajas desplazan la ubicación de la amplitud máxima hacia el ápex. Entre más baja sea la frecuencia, más cerca del ápex se ubica este máximo de amplitud. Estos resultados ilustran el alto desempeño, flexibilidad y confiabilidad del método propuesto, que constituye una valiosa contribución al desarrollo de esquemas de lattice-Boltzmann más poderosos.

Palabras clave: Cóclea, Membrana Basilar, Acústica, Ondas, Simulación, lattice-Boltzmann, Coordenadas generales.

Abstract

Lattice-Boltzmann models have been very powerful tools to simulate fluid dynamics, diffusion processes, mechanical waves and electrodynamics. Nevertheless, their applicability has been

restricted due to the fact that most of them are build on Cartesian coordinates, which hinders them to take advantage of system's symmetries to reduce the dimensions of the computational domain or to naturally addressing complex systems with curved boundaries, from which the Cochlea, the main auditory organ in mammals, is a paradigmatic example. This work designs and implements a novel lattice-Boltzmann model for the three-dimensional simulation of acoustic waves in general curvilinear coordinates. The method keeps in the computer the standard structure of a Cartesian system with the same velocity vectors in all cells, but it rescales the macroscopic fields and adds forcing terms to reproduce in the continuous limit the wave equation on general coordinates. The resulting second order method perfectly finds the vibrational normal modes of a Cylinder, a Trumpet and a Torus, keeps the isotropic wave propagation in real space and can be applied to any coordinate system. With this method in hand the simulation of the Cochlea was addressed. The Cochlea was parametrized as a tampered coiled tube with a cardioid as cross section and, it was scaled to have the real dimensions of a human Cochlea. As result, we found that the geometry of the Cochlea itself is enough to reproduce the effect of spatial frequency segregation: At high frequencies the net pressure on the Basilar membrane oscillates with larger amplitude close to the windows, and lower frequencies shift the location of maximal amplitude to the apex. The lower the frequency is the closer to the apex that maximum is located. Those results illustrate the high performance, flexibility and reliability of the proposed method, which constitutes a valuable contribution to the development of more powerful lattice-Boltzmann schemes.

Keywords: Cochlea, Basilar Membrane, Acoustics, Waves, Simulation, lattice-Boltzmann, General coordinates.

Contents

1. Introduction

Cochlea is an important part of the auditory system of the mammals, because it is responsible for the frequency differentiation and the conversion of the sound waves into electric signals that can be processed in the brain. Degradation of the inner cochlear structures is related with hearing losses and some important auditory problems. Therefore, a thorough understanding of the cochlea is of main importance in the design of hearing aid devices as well as in the prevention and correction of such auditory problems. Due the complex geometry and the variety of processes that are present inside the cochlea, some processes like the cochlear amplification [1] remain without a satisfactory explanation and are being object of research in many science fields like neuroscience and biophysics. This research can be accomplished through experiments, analytical works or simulations. The geometry of the cochlea and its main parts are shown in Fig. **1-1**
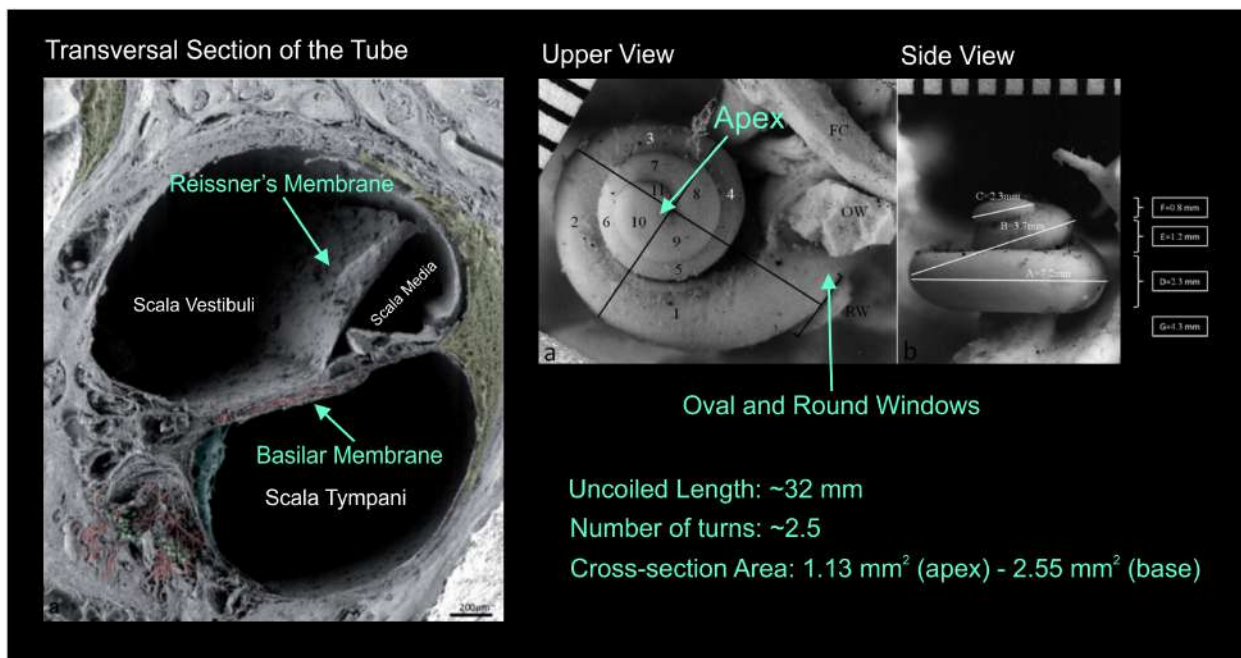

Figure 1-1.: Anatomy of the Cochlea. Source: [13]

One of the first and most important experimental researches in the study of the Cochlea was made by Georg von Békésy [2], who deeply investigated the cochlea through passive

measurements and physical models [3]. His results, which deserved him the Noble prize, are the basis of the current knowledge in hearing research. However, due to the passive nature of his measures there are some processes in the cochlea that were not observed at that time, like cochlear amplification and otoacustic emissions, among others [4]. Meanwhile, since the Cochlea is embedded into the densest part of the temporal bone, measurements in-vivo are very difficult. Recent measurements using micro-computed tomography (μTC) have achieved to give a very detailed three-dimensional model of the Cochlea, which constitutes a very helpful information for future theoretical and computational research, even though the Reissner's membrane couldn't be observed[5]. One of the complications in experimental studies of the Cochlea is that the frequency range is too small to be accurately measured with the current technology; moreover, preparing experimental samples to observe some unstudied characteristics of Cochlea uses to be a great challenge. On the other side, analytical descriptions of the Cochlea are also not simple, due to presence of a great amount of different processes inside and, even though some physical principles have been well understood for almost 60 years, most of the mathematical models employed are too simple. Very often, the Cochlea is modelled as a fluid-filled tube with a uniform Basilar membrane dividing its length. Due to its intricate geometry and its coupling of processes of different nature, it is almost impossible to completely solve a realistic model of the cochlea by using analytical models only.

A powerful tool to overcome some of the difficulties in the study of such a complex system is the computational approach, which has gained considerable relevance in recent years. Nevertheless, a fully detailed model of the Cochlea can be still very expensive in computational resources and time, due to the intricate geometry. For that reason, it has been necessary to simplify the model in some ways: considering the cochlea as a bi-dimensional tube, taking the cochlea as unwrapped ignoring the effect of the coiling in the cochlear response or assuming that the Scala media is merged with the Scala Vestibula, since the separation membrane (Reissner's membrane) is very complaint and moves simultaneously with the fluids.

Lattice-Boltzmann models constitute a relatively recent alternative for the solution of partial differential equations. As any cellular automata does, a lattice-Boltzmann divides space into cells and time into discrete steps, but includes a discrete set of velocities at each cell connecting to the neighbouring ones. The cell saves the probabilities of finding a molecule of a (real or fictitious) fluid in such position and with each discrete velocity. Those probabilities evolve by following the transport Boltzmann equation, usually in the Bhatnagar-Groos-Krook approximation [6] i.e. exponentially decaying to equilibrium functions , before travelling to the neighbouring cells. Since every cell works independently, the model is directly parallelizable and can be easily implemented on GPUs, with computing times two to three orders of magnitude faster than multiple core CPUs. The lattice-Boltzmann model has been a successful approach for the simulation of a wide range of systems such as fluid mechanics, capillarity,

diffusion, and acoustics, too. Thus, it can be a good alternative for the acoustic simulation of the Cochlea. Nevertheless, its implementation in systems with complex geometries has been very difficult, since cells until now were restricted to rectangular shapes, limiting their accuracy to model curved surfaces, like in the Cochlea.

Various procedures has been proposed to extend the lattice-Boltzmann method to perform simulations in a more general set of coordinates and overcome the restrictions imposed by Cartesian cubic cells. The first proposal was done by Nannelli and Succi in 1992 [7], where the cells can be irregular quadrilaterals, and, later in 1997, He and Doolen [8] constructed a lattice-Boltzmann model in polar coordinates. Nevertheless, additional interpolation steps were needed in these two approaches. More recently, Li *et. al.*[9] in 2010 and Reijers, Gelderblom and Toschi,[10] in 2015 developed lattice-Boltzmann models for fluids in axisymmetric coordinate systems. However, these models result to be very demanding in computational resources and, the simulations shown excesively large dissipative effects. In 2012 Budinsky developed a more general model for the two-dimensional shallow water and Navier-Stokes equations[11]. In that scheme, the equations are written in general coordinates, and the additional geometric terms (written by means of the Jacobian and Jacobian spacial derivatives) are introduced as forcing terms in the collision. As result, this proposal does not need further discretization or interpolation steps. Simultaneously, M. Mendoza [12] proposed in his doctoral thesis a procedure to construct lattice-Boltzmann models in curvilinear coordinates that has shown very good results by simulating hydrodynamics in cylindrical and spherical coordinates, and even when the metric is randomly generated (Campylotic). In this two last models all information about the curvilinear coordinate system is included in the equilibrium distribution function and the forcing term, which make them very versatile and easy to implement.

In this work we extend the model proposed by Mendoza to simulate acoustic waves in general coordinates. The model is tested in different curved systems like cylinders, trumpets and torus, and the results are in excellent agreement with the theoretical expectations. Finally, a very realistic model of the Cochlea is geometrically and physically constructed to simulate its response to several frequencies and, to look for the frequency segregation there. The work is organized in eight chapters. Chapter 2 explains the anatomy and physiology of the Cochlea and its main functional mechanisms. Chapter 3 introduces the LBM for the wave equation in Cartesian coordinates, and show some examples to illustrate the versatility of the model. In Chapter 4 we show our first trials to build the proper functional form of the equilibrium distribution function in order to keep both isotropy and stability. The final model is described and tested in Chapter 5 by simulating the pressure waves inside a Pipe, a Trumpet and a Torus. The Cochlea is modelled and its frequency response is tested in Chapter 6. Next, an additional novel model constructed to couple wave simulations in LBM with rigid movable objects is presented and tested in Chapter 7 Even though in this work we only study the

pressure waves on the membrane, the immersed boundary model will allow us to study the bidirectional interactions between the acoustic waves in the fluid and the membrane in future research. The main results, implications and outlook are summarized in Chapter 8.

2. What is the Cochlea?

The cochlea is the main part of the inner ear in mammals and play a key role in the audition since it is responsible for the frequencies differentiation and the conversion of the sound waves into electric signals that can be processed by the brain, in this process, the cochlea also amplifies the sound signal to ease the transduction. Fig. **2-1** shows a sample obtained by injecting a solidifying material into a real human cochlea (Corrosion Casting Technique).
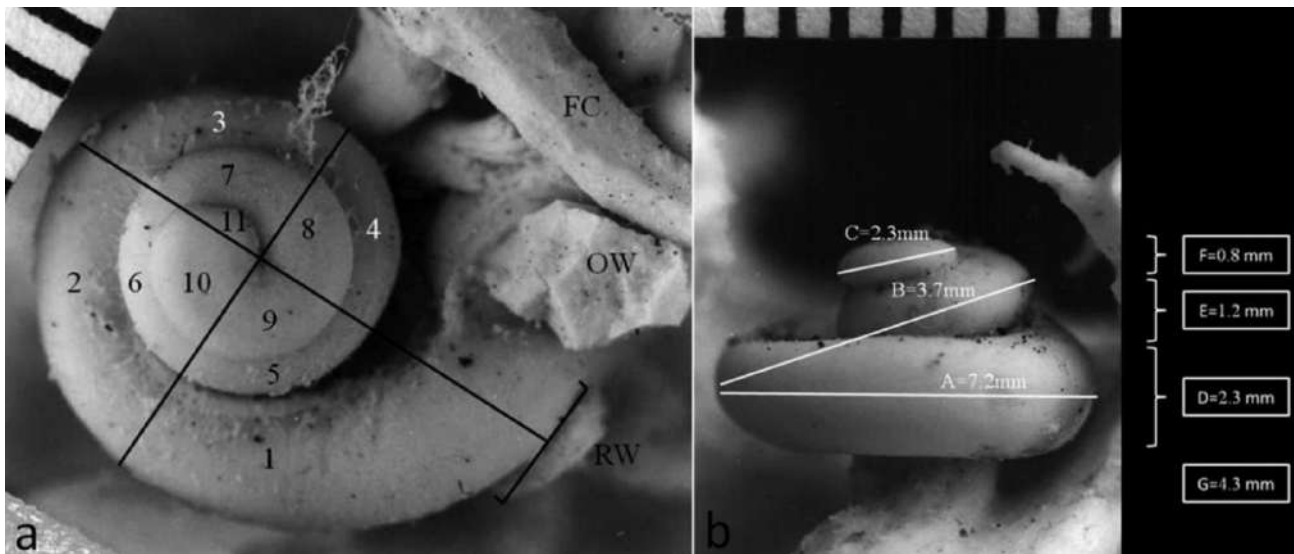
Figure 2-1.: Corrosion casting of a human cochlea top view (left) and side view (right)
Source: [13]

2.1. Anatomy

The human cochlea is a coiled fluid-filled tube that makes 2.5-2.75 turns around the osseous spiral lamina and surrounded by the temporal bone, its transversal section is similar to a cardioid, the internal structure is longitudinally divided in three parallel channels: the Scala tympani, the Scala vestibula and the Scala media whose ratio of cross-section is 8:5:3, respectively (Fig. **2-2**). The Scala tympani and the Scala vestibula are filled with a liquid (called $p$erilymph) and are connected through a hole (called the $h$elicotrema) in the

apex (the end) of the cochlea. The Scala media in turn is filled with another liquid (the *endolymph*) richer in ions, and contains the organ of Corti, which is the sensory organ of hearing, which transforms the acoustic waves into electric signals. The membrane dividing the scala Vestibuli from the scala media is called *R*eissner's membrane, and the one dividing the scala media from the scala Tympani is called the *B*asilar membrane, supporting the organ of Corti. The connection between the middle ear bones (the stapes) and the inner ear is achieved through the *o*val window, an aperture covered with a membrane that is located at the base of the cochlea in the Scala vestibula. Consequently, since the system is filled of fluid, it is necessary to have a second window to maintain a constant volume. This is called the *r*ound window and is located at the base of the Scala tympani.[14]
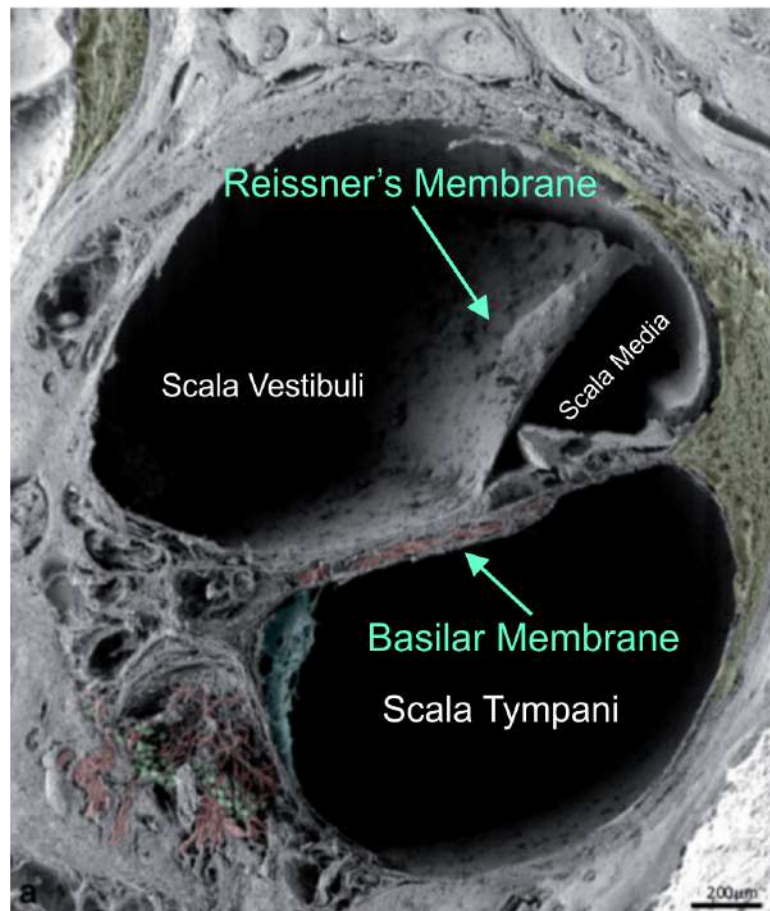
Figure 2-2.: Transversal view of the cochlea. Source: [13]

The cross-section area of the cochlea varies from 2.55 mm^2 at the base to 1.13 mm^2 at the apex and its length is in the range [32, 34] mm. Contrary, the width of the Basilar Membrane is 0.1mm at the base and 0.5mm at the apex, while its thickness goes from 7.5×10^{-3} mm

at the base to 2.5×10^{-3} mm at the apex, the thickness of the Reissner's membrane is 6.6×10^{-3} mm at the base and 4.4×10^{-3} mm at the apex. Fig. **2-3** is a scheme of an uncoiled cochlea to exemplify its dimensions.

Windows   Apex
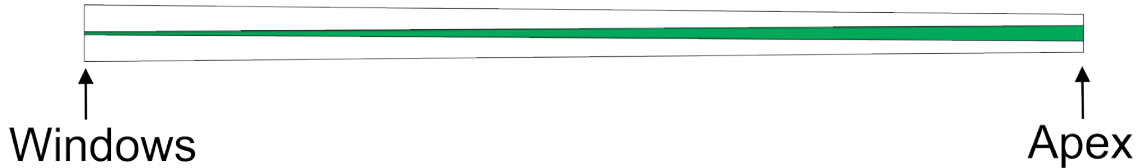
Figure 2-3.: Scheme of a top view of an uncoiled cochlea at 5:1 scale where the green strip represents the Basilar Membrane

2.2. Physiology

The sound waves are transmitted by the stapes to the oval window, which starts to vibrate. Due the fluid displacement, the round window vibrates too, with similar amplitude but in counter phase. This phase-shifted vibrations generate pressure differences over the Scala media and particularly over the Basilar membrane that leads to a traveling wave along the Basilar membrane. The characteristic vibration of the Basilar membrane in response to pressure differences was widely studied by Bekesy [2], who discovered that the amplitude of the travelling wave is located below an envelope. The distance from the stapes to the maximum of this envelope depends on the frequency of the stimulus, i.e. high-frequency stimuli generate travelling waves whose maxima amplitudes locate near the base of the cochlea, while low-frequency stimuli localize their maxima at the end of the cochlea, near the helicotrema. This localization of the maximum of the vibration is the main mechanism of frequency differentiation as follows: The organ of Corti has a huge amount of hair cells along the cochlea that responds to the vibration and sends electrical impulses to the brain via the auditory nerve. The group of hair cells that will be activated corresponds to the region where the maximum amplitude of the travelling wave is located; therefore, the stimuli sent to the brain contains information about the frequencies of the original sound wave.

2.3. Past Numerical Studies on the Cochlea

For almost 30 years there have been four main computational approaches and solution methods to model the cochlea: finite differences, finite elements, (Wentzel-Kramers-Brillouin) WKB approximation, and immersed boundary methods.
In 1992, Beyer [15] developed and implemented an implicit immersed boundary method for the simulation of a two-dimensional and unwrapped cochlea by immersing the whole

structure of the cochlea in a rectangular fluid domain and by solving the Navier-Stokes equations via finite differences. The boundaries, that represents the cochlear structure, are included in the computational model as another set of discrete points coupled to the grid of the fluid. The boundaries in the coupling act over the fluid by applying forces, while the fluid in turn moves the non-rigid boundaries with its local velocity. With this method, Beyer was able to simulate traveling waves inside the cochlea and study the phase shifts present in the vibration of the Basilar membrane, finding a good agreement with experimental data.

In 2000, Parthasarathi et. al. [16] proposed an analytical-computational method using the Galerkin approximation to variational equations in a finite elements framework to simulate the behavior of the cochlea, and found important differences between 2D and 3D models. But, in order to decrease computational costs, they consider a very simplified geometry and let more complicated geometries for future studies. In the same year Givelberg et. al. [17] took into account a more realistic geometry by simulating a three dimensional coiled cochlea by running in parallel computers the immersed boundary method. Nevertheless, the micro-mechanics of the Basilar membrane remains at this point without computational study, since in the methods described above the organ of Corti, the Basilar membrane and the Tectorial membrane are merged in a single membrane.

In 2005 Cai and coworkers [18] formulated an analytic-computational method based on the WKB aproximation to simulate a very detailed cochlea, being one of the most realistic models by now. Cai et. al. used a curvilinear coordinate system, later approximated to cylindrical coordinates, to study the effect of coiling in the cochlea at the apex. As a result, they found that the wrapped geometry of the cochlea has a great effect on the relative movement between the Tectorial and Basilar membranes. Nevertheless, due to the approximations of the analytical model they were able to study this behaviour at the apex of the cochlea only.

More recently, in 2013 Edom, et. al. [19] studied a rectangular bidimensional cochlea in the immerse boundary framework by using Runge-Kutta in time domain and finite differences in the spacial domain. The aim of the work of Edom et. al. was to study the influence of the rocking movement of the stapes on the mechanical behaviour of the cochlea, in comparison with its piston-like movement. They found the interesting result that the rocking movement could lead to hearing when the piston-like movement is not possible, for example, due to the round window atresia. Also in 2013, Ren et. al. [20] simulated an unwrapped and tampered cochlea using finite elements and taking into account both the longitudinal and transversal coupling of the Basilar membrane. They found that the transmission time of the travelling wave depends on the input frequency, with lower frequencies having longer transmission times.

In 2014 Sabo and collaborators[21] have developed a novel model of the cochlea that takes into account the acoustic pressure waves and pressure difference over the Basilar membrane instead of the movement of the fluid. In this model, they take the pressure distribution as an input through the oval window, so they are able to stimulate the cochlea with more realistic sounds, like a spoken sentence. An important contribution of Sabo et. al. is the consideration

of the Tectorial and Basilar membranes and the introduction of the population of outer hair cells as a parameter, because they can study the effect of the outer hair cells on the overall behaviour of the cochlea and compare the response to a complex sound of a healthy cochlea and a damaged cochlea with a low population of hair cells. Additionally, Sabo et. al. provide a detailed set of physical parameters that can be very useful for future simulations.

Despite the variety of points of view, methods, and approximations mentioned above, the intricate geometry of the cochlea is a remaining problem, since modelling the coiling and a realistic transversal section can be quite complicated through numerical methods like finite differences or finite elements. Thus, a lattice-Boltzmann model on curvilinear coordinates can be a great alternative to solve this geometric problem and improve the realism in simulations of the cochlea.

3. Lattice-Boltzmann method for acoustics in Cartesian coordinates

3.1. About lattice-Boltzmann methods

Lattice-Boltzmann models (LBMs) are relatively new computational tools based on Boltzmann's kinetic theory and cellular automata[22, 23] which have been succesfully used to simulate[24]. Furthermore, LBM have been recently extended to simulate more general systems, as long as they can be described as a set of conservation laws. In that sense, it has been possible to construct and implement LBMs to solve diffusion[25], mechanical waves[26] and electrodynamics[27]. In comparison with other numerical schemes (like finite-differences or finite-element methods) all variables needed to compute for the next time step are stored locally in the computational space, making them perfect to run parallel on graphic cards. Due to its versatility and parallel nature, lattice-Boltzmann methods have gained the interest of a wide range of research areas and industrial applications.

Standard LBMs, like the one described in this section, divides the two (three) dimensional computational domain into a regular lattice of square (cubic) cells and assigns a set of λ discrete velocities $\vec{\xi}_i$ to each lattice node (Fig. 3.1). Each velocity has an associated weight w_i, whose values are chosen to maintain the spatial isotropy in the computational domain. Those weights should fulfil the following conditions:

$$\sum_i w_i = 1 \quad ,$$
$$\sum_i w_i \xi_i^\alpha = 0 \quad ,$$
$$\sum_i w_i \xi_i^\alpha \xi_i^\beta = \delta^{\alpha\beta} c_s^2 \quad , \tag{3-1}$$
$$\sum_i w_i \xi_i^\alpha \xi_i^\beta \xi_i^\gamma = 0 \quad ,$$
$$\sum_i w_i \xi_i^\alpha \xi_i^\beta \xi_i^\gamma \xi_i^\delta = c_s^4 \left(\delta^{\alpha\beta}\delta^{\gamma\delta} + \delta^{\alpha\gamma}\delta^{\beta\delta} + \delta^{\alpha\delta}\delta^{\beta\gamma} \right) \quad .$$

Here, ξ_i^α is the α-th velocity component of the velocity ξ_i ($\alpha \in \{x, y, z\}$) and c_s^2 is a constant related with the information propagation speed along the lattice. Typical values of such

weights are also shown in Fig. 3.1.

Each node locally stores the information of the system at the point $\vec{x}$ in λ probability distribution functions $f_i(\vec{x}, t)$, which, in the case of fluids, are proportional to the probability to find a molecule moving with velocity $\vec{\xi_i}$ in position $\vec{x}$ at time t. The physical information of the system, i. e. the fields of macroscopic variables, are obtained by computing the statistical moments of those distribution functions. For the case of acoustic waves, we have

$$P = \sum_i f_i^{eq} \quad , \quad \vec{J} = \sum_i f_i^{eq} \vec{\xi_i} \quad , \quad \Pi^{(0)} = \sum_i f_i^{eq} \vec{\xi_i} \otimes \vec{\xi_i} \quad , \tag{3-2}$$

where P is the pressure, the vector field $\vec{J}$ is proportional to the time derivative of the mean molecular displacement and $\Pi^{(0)}$ is proportional to the isotropic stress. The physical meaning of these quantities and the functional form of f_i^{eq} become evident when the macroscopic conservation laws are set.
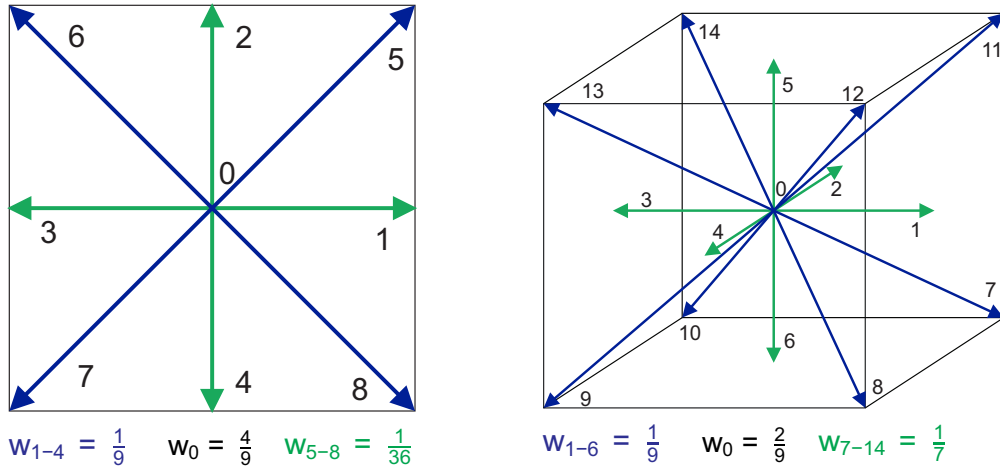
Figure 3-1.: Discrete sets D2Q9, with $\lambda = 9$ velocities in two dimensions, (left) and D3Q15, with $\lambda = 15$ velocities in three dimensions (right). In DXQY, X represents the dimension of the velocity set, whereas Y is the number of velocities in the discretization.

The equilibrium distribution functions evolve in space and time by following the Boltzmann's transport equation,

$$f_i\left(\vec{x} + \vec{\xi_i}\delta_t,\, t + \delta_t\right) - f_i(\vec{x},\, t) = \Omega(f) \,, \tag{3-3}$$

the process can be divided in two parts, collision and advection. In the collision part, the cells locally interact with each other and update their value to a new one f_i^{new} according to a collision rule described by the operator $\Omega(f)$ which, in the macroscopic limit, will lead the overall behaviour of the system. In 1954, Bhatnagar, Gross and Krook [6] proposed a

simplify, less detailed form of the collision operator. In their proposal, the collision process adds to the distribution function the difference between the current value and the value it would have at the equilibrium f_i^{eq}, divided by a relaxation parameter τ. That is, if the distribution functions were not transported to the next cells, this equation would represent an exponential decay to equilibrium,

$$f_i^{new}(\vec{x},\, t) = f_i(\vec{x},\, t) - \frac{\delta_t}{\tau}\left[f_i(\vec{x},\, t) - f_i^{eq}(\vec{x},\, t)\right], \tag{3-4}$$

where δ_t is the time step. In the advection part, these new values are spread to the neighbouring cells in the λ directions determined by the velocities set,

$$f_i\left(\vec{x} + \vec{\xi}_i\delta_t,\, t + \delta_t\right) = f_i^{new}(\vec{x},\, t) \quad . \tag{3-5}$$

After the advection-collision step the macroscopic variables are updated and then used to find new values of f_i^{eq}.

Note that, because the equilibrium state leads the macroscopic behaviour of the system, it should be defined in such a way that the macroscopic conservation laws can be successfully retrieved. Sec. 3.2.2 shows how to find f_i^{eq} to simulate the wave equation.

3.2. Constructing the lattice-Boltzmann method for the wave equation

The first approach to simulate the wave equation by LBMs was proposed in 1998 by Chopard, Luthi and Wagen [28]. The model introduces the equilibrium distribution function and the macroscopic variables to reproduce the wave equation, and with simple modifications runs on almost every velocity set, including D2Q5 and D3Q7. Later, in 2000 Guangwu [26] proposed to redefine the first macroscopic momentum of the LBM as the temporal derivative of the wave pressure. This also leads to the pressure wave equation, but an additional integration step is needed. In addition, some approaches use the standard LBM for the Navier-Stokes equation (NSE) to simulate waves by measuring the pressure waves present in such dynamics, but with some restrictions and at a very high computational cost, for instance, in 2011 Li and Shan [29] simulated the NSE with a Multiple Relaxation Time lattice-Boltzmann and studied the decay of pressure signals due to viscous, thermal and acoustic dampings. Their model requires very high order approximations, which make it very demanding on computational resources, and applies only for low frequencies. In 2015 Sun *et. al.* [30] used a forced lattice-Boltzmann model to solve the NSE for the fluid inside a fully saturated porous medium, and studied the propagation of a pressure front there. The absorption coefficients derived from the simulations coincide well with the theoretical expectations, bur not with the experiments, due perhaps to the need of extra factors like thermal dissipation and flexibility of the porous medium. In 2016, Salomons, Lohman and Zhou [31], studied various cases

of outdoor acoustics in 2D with a Multiple Relaxation Time lattice-Boltzmann model for the NSE, but the restrictions of minimal viscosity in the model avoids them to obtain the almost non-dissipative behavior found in the real air. These limitations in using NSE-LBMs to simulate acoustic waves favour the use of simpler schemes specifically designed for the wave equation, as the one proposed by Chopard *et. al.* Now, let us describe the way to construct this lattice-Boltzmann for acoustic simulations.

3.2.1. Chapman-Enskog Expansion

Constructing a given lattice-Boltzmann scheme to solve any particular set of conservation laws reduces to find the proper form of the equilibrium distribution functions f_i^{eq} which leads to those conservation laws via the Eq. (3-8) in the macroscopic limit. The Chapman-Enskog expansion allow us to show that, in fact, the wave equation properly written as a set of conservation laws can be retrieved from the lattice-Boltzmann scheme and, help us to define f_i^{eq} to achieve such conservation laws.

The Chapman-Enskog expansion [32] is a standard scheme to find the set of macroscopic differential equations the system fulfils in the continuous limit, that is when both the cell size δx and the time step δt go to zero. It consists of three elements. The first element is a Taylor expansion of the left side of the evolution rule (Eq. (3-3)), which at second order reads:

$$f_i\left(\vec{x} + \vec{\xi_i}\delta_t,\, \vec{\xi_i},\, t + \delta_t\right) - f_i\left(\vec{x},\, \vec{\xi_i},\, t\right) =$$
$$\delta_t\left[\frac{\partial}{\partial t} + \vec{\xi_i}\cdot\nabla\right]f_i\left(\vec{x},\, \vec{\xi_i},\, t\right) + \frac{\delta_t^2}{2!}\left[\frac{\partial}{\partial t} + \vec{\xi_i}\cdot\nabla\right]^2 f_i\left(\vec{x},\, \vec{\xi_i},\, t\right) \qquad (3\text{-}6)$$

 The second element is a perturbative expansion of both the distribution functions f_i and the differential operators $\frac{\partial}{\partial t}$ and ∇,

$$f_i = f_i^{(0)} + \epsilon f_i^{(1)} + \epsilon^2 f_i^{(2)}\,,$$
$$\nabla = \epsilon\nabla_1\,, \qquad\qquad\qquad\qquad\qquad\qquad (3\text{-}7)$$
$$\frac{\partial}{\partial t} = \epsilon\frac{\partial}{\partial t_1} + \epsilon^2\frac{\partial}{\partial t_2}\,.$$

The perturbative parameter ϵ is known as the Knudsen number, the rate between the mean free path between collisions and the macroscopic scales of the system. In a lattice-Boltzmann, the collisions occur from cell to cell, so the mean free path is the cell size itself, and $\epsilon = \delta x/x$ and, $\epsilon \to 0$ is the continuous limit. The third element is the assumption that the macroscopic fields cannot be affected by the cell size, if it is small enough; therefore, they must be function of f_i^0 only,

$$P = \sum_i f_i^0 \quad,\quad \vec{J} = \sum_i f_i^0\vec{\xi_i} \quad,\quad \Pi^{(0)} = \sum_i f_i^0\vec{\xi_i}\otimes\vec{\xi_i} \quad. \qquad (3\text{-}8)$$

By replacing (3-7) and (3-6) into (3-4) and considering terms up to second order, we obtain

$$
-\frac{\delta_t}{\tau}\left[f_i^{(0)} + \epsilon f_i^{(1)} + \epsilon^2 f_i^{(2)} - f_i^{eq}\right] =
$$
$$
\delta_t\left[\epsilon\frac{\partial}{\partial t_1} + \epsilon^2\frac{\partial}{\partial t_2} + \epsilon\vec{\xi_i}\cdot\nabla_1\right]f_i^{(0)} + \delta_t\left[\epsilon\frac{\partial}{\partial t_1} + \epsilon\vec{\xi_i}\cdot\nabla_1\right]\epsilon f_i^{(1)} + \frac{\delta_t^2}{2!}\left[\epsilon\frac{\partial}{\partial t_1} + \epsilon\vec{\xi_i}\cdot\nabla_1\right]^2 f_i^{(0)}
$$
$$
\tag{3-9}
$$

equating order by order, one obtains:

- 0th order:

$$
f_i^{(0)} = f_i^{(eq)}\quad. \tag{3-10}
$$

- 1st order:

$$
-\frac{1}{\tau}f_i^{(1)} = \left[\frac{\partial}{\partial t_1} + \vec{\xi_i}\cdot\vec{\nabla}_1\right]f_i^{(0)}\quad. \tag{3-11}
$$

- 2nd order:

$$
-\frac{1}{\tau}f_i^{(2)} = \delta_t\left[\frac{\partial}{\partial t_1} + \vec{\xi_i}\cdot\nabla_1\right]f_i^{(1)} + \frac{\partial}{\partial t_2}f_i^{(0)} + \frac{\delta_t^2}{2!}\left[\frac{\partial}{\partial t_1} + \vec{\xi_i}\cdot\nabla_1\right]^2 f_i^{(0)}\quad. \tag{3-12}
$$

By replacing Eq. (3-11) into Eq. (3-12), this last equation can be simplified to

$$
-\frac{1}{\tau}f_i^{(2)} = \delta_t\left(1 - \frac{1}{2\tau}\right)\left[\frac{\partial}{\partial t_1} + \vec{\xi_i}\cdot\nabla_1\right]f_i^{(1)} + \frac{\partial}{\partial t_2}f_i^{(0)}. \tag{3-13}
$$

Here, in order to avoid viscous effects and additional dissipations, and maintaining the model linear in the velocities, we can choose $\tau = 0.5$. In [28] Chopard, Luthi and Wagen showed that, unlike the case for fluid dynamics, this choice is not unstable in the lattice-Boltzmann model for acoustics; instead, it assures the time reversibility, increases the stability and allows us to obtain the wave equation exactly.

With this choice, the sum of the products of 3-11 multiplied by ϵ and 3-13 by ϵ^2 is

$$
-\frac{1}{\tau}\left(\epsilon f_i^{(1)} + \epsilon^2 f_i^{(2)}\right) = \frac{\partial}{\partial t}f_i^{(0)} + \vec{\nabla}\cdot\left(\vec{\xi_i}f_i^{(0)}\right)\quad, \tag{3-14}
$$

where we used the fact that the vectors $\vec{\xi}$ are the same for all cells i.e. they are independent on the position. Now, by adding on the whole set of discrete velocities and taking the limit $\epsilon \to 0$, we find a first conservation law

$$
\frac{\partial P}{\partial t} + \nabla\cdot\vec{J} = 0\quad. \tag{3-15}
$$

Similarly, multiplying Eq. (3-14) by $\vec{\xi_i}$ and then adding give us a second conservation law

$$\frac{\partial \vec{J}}{\partial t} + \nabla \cdot \vec{\Pi}^{(0)} = 0 \quad . \tag{3-16}$$

The same procedure can be followed to construct an infinite set of conservation laws of higher order, just multiplying by $\vec{\xi_i}$ more times before adding. Nevertheless, Eqs.(3-15) and (3-16) are enough to obtain the wave equation via the proper definition of the equilibrium distribution functions. Note that if we handle to obtain

$$\Pi_{ij}^{(0)} = c^2 P \delta_{ij} \quad , \tag{3-17}$$

Eq. (3-16) and the time derivative of Eq. (3-15) become

$$\frac{\partial \vec{J}}{\partial t} + c^2 \nabla P = 0 \quad , \tag{3-18}$$

$$\frac{\partial^2 P}{\partial t^2} + \nabla \cdot \left(\frac{\partial \vec{J}}{\partial t} \right) = 0 \quad . \tag{3-19}$$

Now, by replacing Eq. (3-18) into Eq. (3-19) we obtain

$$\frac{\partial^2 P}{\partial t^2} - c^2 \nabla^2 P = 0 \quad , \tag{3-20}$$

that is, the wave equation for the pressure P in Cartesian coordinates, with c the wave velocity. In addition, because the pressure in an acoustic wave is related with the mean displacement D of the particles in the fluid through the relation $P = -B \nabla \cdot \vec{D}$ with B the bulk modulus [33], Eq. 3-15 indicates that the macroscopic quantity $\vec{J}$ is related with the displacement velocity via

$$\vec{J} = B \frac{\partial \vec{D}}{\partial t} \quad . \tag{3-21}$$

3.2.2. Equilibrium distribution function

Our task now is to find a proper functional form of the discrete equilibrium distribution functions f_i^{eq} to satisfy the condition (3-17) and the Eqs. (3-8). This can be done by two main ways: The first of one is to formulate an Anzatz for f_i^{eq} as a weighted series with increasing orders of $\vec{\xi}$ and to find the proper coefficients that fulfil the given restrictions. This procedure is called Moment matching. The second alternative is to discretize a proposed continuous equilibrium function in the velocity space by means of an Hermite series. The first approach is easier to follow, but hide some important information of the system behaviour. The Hermite polynomials procedure let us to find additional terms and will be more useful to increase the system stability, as we show in below.

Moment Matching

Finding a proper Anzatz for f_i^{eq} seems to be very tricky. However, most velocity sets fulfil the identities (3-1). This includes $\sum_i \mathrm{w}_i \xi_i^\alpha \xi_i^\beta = \delta^{\alpha\beta} c_s^2$, which is very similar to the expression $\Pi^{(0)} = \sum_i f_i^{eq} \xi_i^\alpha \xi_i^\beta$. This suggests the following functional form for the equilibrium function:

$$f_i^{eq} = \begin{cases} \mathrm{w}_0 A & \text{if} \quad i = 0 \\ \mathrm{w}_i \left(B + C\vec{\xi}_i \cdot \vec{J} \right) & \text{if} \quad i \neq 0 \end{cases}, \tag{3-22}$$

where A, B and C are constants to be determined. The term $C\mathrm{w}_i \vec{\xi}_i \cdot \vec{J}$ has been added to fulfil the equation. $\vec{J} = \sum_i f_i^{eq} \vec{\xi}_i$.

First, let us replace Eq. (3-22) into the third part of Eq. (3-8). By using the relations (3-1), we have

$$\begin{aligned} \Pi^{(0)} = \sum_i f_i^{eq} \vec{\xi}_i \otimes \vec{\xi}_i &= \sum_i \sum_\gamma \mathrm{w}_i \left(B + C\xi_i^\gamma J^\gamma \right) \xi_i^\alpha \xi_i^\beta \\ &= \sum_i \mathrm{w}_i \left(B\xi_i^\alpha \xi_i^\beta + \sum_\gamma C\xi_i^\gamma J^\gamma \xi_i^\alpha \xi_i^\beta \right) \\ &= B \sum_i \mathrm{w}_i \xi_i^\alpha \xi_i^\beta + \sum_\gamma C J^\gamma \sum_i \mathrm{w}_i \xi_i^\gamma \xi_i^\alpha \xi_i^\beta \\ &= B \sum_i \mathrm{w}_i \xi_i^\alpha \xi_i^\beta = B c_s^2 \delta^{\alpha\beta} \, ; \end{aligned} \tag{3-23}$$

thus, $B = c^2 P / c_s^2$. In the same way, we need $\vec{J} = \sum_i f_i^{eq} \vec{\xi}_i$, which leads to

$$\begin{aligned} J^\alpha = \sum_i \sum_\gamma \mathrm{w}_i \left(\frac{c^2 P}{c_s^2} + C\xi_i^\gamma J^\gamma \right) \xi_i^\alpha \\ = \sum_i \mathrm{w}_i \left(\frac{c^2 P}{c_s^2} \xi_i^\alpha + \sum_\gamma C\xi_i^\gamma J^\gamma \xi_i^\alpha \right) \\ = \frac{c^2 P}{c_s^2} \sum_i \mathrm{w}_i \xi_i^\alpha + \sum_\gamma C J^\gamma \sum_i \mathrm{w}_i \xi_i^\gamma \xi_i^\alpha \\ = C \sum_\gamma J^\gamma \sum_i \mathrm{w}_i \xi_i^\gamma \xi_i^\alpha = C \sum_\gamma J^\gamma c_s^2 \delta^{\gamma\beta} = C c_s^2 J^\alpha \, . \end{aligned} \tag{3-24}$$

This result indicates that $C = c_s^{-2}$. The value of A can be found from

$$f_0^{eq} = P - \sum_{i=1}^\lambda f_i^{eq} \, . \tag{3-25}$$

Summing up these results, we obtain the equilibrium distribution function

$$
f_i^{eq} = \begin{cases} P + \frac{c^2}{c_s^2} P \left(\mathrm{w}_0 - 1 \right) & if \quad i = 0 \\ \frac{\mathrm{w}_i}{c_s^2} \left(c^2 P + \vec{\xi}_i \cdot \vec{J} \right) & if \quad i \neq 0 \end{cases} .
\tag{3-26}
$$

This equation builds a diagonal tensor $\Pi^{(0)}$ (Eq. 3-17) and satisfies the definition of the macroscopic quantities P and $\vec{J}$ (Eq. (3-8)).

Gauss cuadratures and Hermite polynomials approximation

An alternative approach to find the equilibrium distribution function is a discretization of the countinuos Boltzmann's equation in the velocities space, starting from the knowledge of the continuous distribution function. As a result, the moments of the distribution function, which are directly related with the macroscopic fields, are no longer complex weighted integrals but simpler sums over a discrete set of velocities. Furthermore, a discrete form of the distribution function can be obtained from a truncated Hermite series expansion. This procedure give us the lattice-Boltzmann equation.

Let us start by considering the conservation laws from the continuous Boltzmann equation. The statistical moments of the distributions are conserved under the collision process [34]. Therefore, its value is the same whether they are computed from f or from its equilibrium value f^{eq},

$$
\begin{aligned}
\int f d^3\xi &= \int f^{eq} d^3\xi = P \,, \\
\int \vec{\xi} f d^3\xi &= \int \vec{\xi} f^{eq} d^3\xi = \vec{J}, \\
\int \vec{\xi} \otimes \vec{\xi} f d^3\xi &= \int \vec{\xi} \otimes \vec{\xi} f^{eq} d^3\xi = \Pi^{(0)} \,.
\end{aligned}
\tag{3-27}
$$

Our aim is to find a simpler form for these relations, but preserving the values of the macroscopic fields P, $\vec{J}$ and $\Pi^{(0)}$. In fluids, which are the macroscopic systems the Boltzmann equation is intended to model, the equilibrium distribution is Maxwell-Boltzmann, which is a Gaussian distribution,

$$
f^{eq} = \frac{\rho}{(\sqrt{2\pi RT})^{\mathcal{D}}} e^{-(\vec{U}-\vec{\xi})^2/2RT} \,,
\tag{3-28}
$$

Where ρ is the fluid density and $\vec{U}$ its velocity, $R = k_B/m$ is the ideal gas constant, with k_B the Boltzmann constant and m, the mass of the particles; T, the temperature and $\mathcal{D}$, the system dimension. The clue is given by regarding that the continuous distribution function has the same functional form of the weight function for Hermite Polynomials,

$$
w(x) = \frac{1}{\sqrt{2\pi}} e^{-x^2/2} \,,
\tag{3-29}
$$

which are defined by

$$\mathcal{H}^{(n)}(x) = (-1)^n \frac{1}{w(x)} \frac{d^n}{dx^n} w(x) , \tag{3-30}$$

and are orthogonal with the dot product

$$f \cdot g = \int_{-\infty}^{\infty} w(x) f(x) g(x) dx . \tag{3-31}$$

For the case of the wave equation, nevertheless, there is not a continuous distribution function that can be taken as a starting point to find its discrete version for LBM. Hence, we have to propose an appropriate continuous form to successfully retrieve the wave equation in the macroscopic limit. Because the wave speed c is the macroscopic speed and c_s is the speed for the particles, one can propose

$$f^{eq}\left(\vec{\xi}\right) = \frac{P}{(\sqrt{2\pi RT})^D} e^{-((c-c_s)\vec{\xi})^2/2RT} . \tag{3-32}$$

Since the Hermite polynomials are orthogonal and form a basis, we can write any function $f(x)$ as a multidimensional Hermite polynomial series of the form

$$f(x) = w(x) \sum_{n=0}^{\infty} \frac{1}{n!} \vec{a}^{(n)} \cdot \vec{\mathcal{H}}^{(n)}(x) , \tag{3-33}$$

where, the coefficients $\vec{a}^{(n)}$ can be obtained as

$$\vec{a}^{(n)} = \int f(x) \vec{\mathcal{H}}^{(n)}(x) dx . \tag{3-34}$$

That is valid on each direction in velocity space,

$$f^{eq}\left(\vec{\xi}\right) = w\left(\vec{\xi}\right) \sum_{n=0}^{\infty} \frac{1}{n!} \vec{a}^{(n)} \cdot \vec{\mathcal{H}}^{(n)}\left(\vec{\xi}\right) . \tag{3-35}$$

Note that one of the reasons for choosing Hermite polynomials is that the series coefficients directly correspond with the statistical moments of the distribution i. e. the system macroscopic quantities.

$$a^{(0)eq} = \int f^{eq} d^d\xi = \rho = \int f d^d\xi , \tag{3-36}$$

$$a^{(1)eq} = \int \xi^\alpha f^{eq} d^d\xi = J^\alpha = \int \xi^\alpha f d^d\xi . \tag{3-37}$$

Next, the expansion can be truncated up to certain order N

$$f^{eq}\left(\vec{\xi}\right) \approx w\left(\vec{\xi}\right) \sum_{n=0}^{N} \frac{1}{n!} \vec{a}^{(n)} \cdot \vec{\mathcal{H}}^{(n)}\left(\vec{\xi}\right) \tag{3-38}$$

As we will show below, an expansion up to second order of the equilibrium distribution function is enough to exactly recover the macroscopic wave equation. Then, we can write

$$f^{eq}\left(\vec{\xi}\right) = w\left(\vec{\xi}\right)\left[a^0\mathcal{H}^0 + a^1\mathcal{H}^1 + a^2\mathcal{H}^2\right]. \tag{3-39}$$

Another important feature of the Hermite polynomials is called Gauss-Hermite Cuadrature, which allow us to find exactly the value of an integral of a weighted polynomial of grade n, $P^{(n)}$, by considering a discrete sum over precise values ξ_i, which are actually the roots of the Hermite polynomial $\mathcal{H}^{(n)}$,

$$\int_{-\infty}^{\infty} w\left(\xi\right)P^{(n)}\left(\xi\right)d\xi = \sum_{i=1}^{N} w_iP^{(n)}\left(\xi_i\right), \tag{3-40}$$

where N must satisfy $n \geq (N+1)/2$. We can use the Eq. (3-40) to easily compute the coefficients $\vec{a}^{(n)}$ (Eq. (3-34)),

$$\vec{a}^{(n)} = \int f^{eq}\left(\xi\right)\vec{\mathcal{H}}^{(n)}(\xi)d\xi = \int w\left(\xi\right)Q\left(\xi\right)\vec{\mathcal{H}}^{(n)}(\xi)dx = \sum_{i=1}^{N} w_iQ\left(\xi_i\right)\vec{\mathcal{H}}^{(n)}\left(\xi_i\right). \tag{3-41}$$

The coefficients are

$$\begin{aligned}
a_0 &= P, & \mathcal{H}_0 &= 1, \\
\vec{a}_1 &= \frac{\vec{J}}{c_s}, & \vec{\mathcal{H}}_1 &= \frac{\vec{\xi}}{c_s}, \\
a^{\alpha\beta}2 &= \frac{P\left(c^2 - c_s^2\right)\delta^{\alpha\beta}}{2c_s^2}, & \mathcal{H}_2^{\alpha\beta} &= \left(\frac{\xi_i^\alpha\xi_i^\beta}{c_s^2} - \delta^{\alpha\beta}\right).
\end{aligned} \tag{3-42}$$

The corresponding equilibrium distribution function is

$$f_{i\neq 0}^{eq} = w_i\left[P + \frac{\vec{\xi_i}\cdot\vec{J'}}{c_s^2} + \frac{P}{2c_s^4}\left(c^2 - c_s^2\right)\delta^{\alpha\beta}\left(\xi_i^\alpha\xi_i^\beta - c_s^2\delta^{\alpha\beta}\right)\right]. \tag{3-43}$$

The expression for f_0^{eq} can be obtained from Eq. (3-25) as before. Summarizing, we have

$$f_i^{eq} = \begin{cases} w_0P\left[\frac{1}{w_0} - \frac{3c^2}{2c_s^2}\right] - P + \frac{5}{2}Pw_0 & \text{if } i = 0 \\ w_i\left[P + \frac{\vec{\xi_i}\cdot\vec{J'}}{c_s^2} + \frac{P}{2c_s^4}\left(c^2 - c_s^2\right)\delta^{\alpha\beta}\left(\xi_i^\alpha\xi_i^\beta - c_s^2\delta^{\alpha\beta}\right)\right] & \text{if } i \neq 0 \end{cases} \tag{3-44}$$

This is an alternative form of the equilibrium distribution function which also retrieves the wave equation. The advantages of obtaining the equilibrium distribution function in this form, will be deeply discussed in Section 5.1.

3.3.   Examples

The method constructed in this Chapter has been successfully implemented to simulate the wave equation in Cartesian coordinates [32]. Phenomena like diffraction, refraction, interference and Doppler effect can be simulated as a first benchmark. The aim of this section is to show these results.

In this part of the work we use a three-dimensional scheme with seven velocities (D3Q7, Fig. **3-2**), with $c_s = 1/2$ and weights w_i given by

$$\mathrm{w}_i = \begin{cases} \frac{1}{4} & \text{if} \quad i = 0 \\ \frac{1}{8} & \text{if} \quad i \neq 0 \end{cases} . \tag{3-45}$$
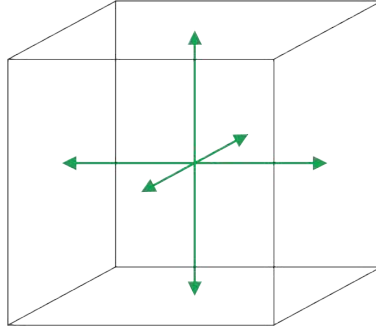

Figure 3-2.: D3Q7 velocities set.

First, we subject the system to a punctual harmonic perturbation for the pressure in the center of our three-dimensional computational domain whose dimensions L_x, L_y and L_z are respectively $100 \times 100 \times 2$ cells (this configuration allow us to study the examples as bi-dimensional without implementing a pure bi-dimensional LB scheme). The perturbation is achieved by imposing the value of the pressure P in one or more cells. For this example we define

$$P_{source} = A \sin(\omega t)\delta(x - L_x/2)\delta(y - L_y/2), \tag{3-46}$$

where the amplitude $A = 1.0$, $\omega = 2\pi c/\lambda$ with $c = 0.32$ and $\lambda = 4L_y/33$. This values will be retained for all the examples in this chapter unless another case is specified. Additionally, it is important to mention that we impose transparent boundary conditions in the borders of the domain, this can be done by making the cell at the boundary to have the same distribution functions its nearest neighbour in the normal direction inwards the border has. The evolution of the perturbation generates a spherical wave as shown in Fig **3-3**.
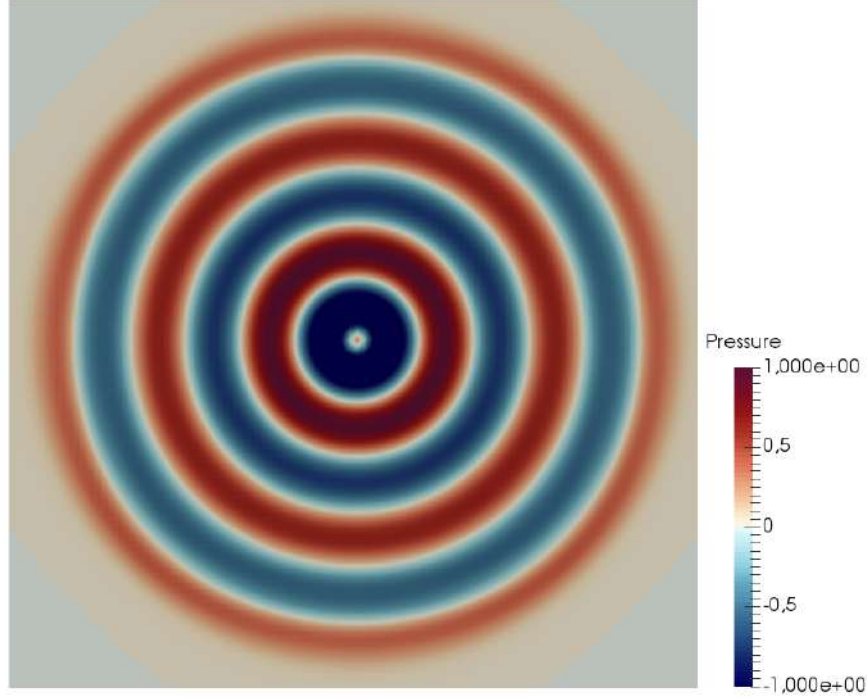
Figure 3-3.: Pressure wave generated by a point source in the center of the computational
domain after $t = 150$ time-steps.

Once we have tested the free evolution of the waves in a three-dimensional domain, a second
benchmark could be the inclusion of an obstacle on order to reproduce diffraction effects, to
that aim, we modify the pressure source to be

$$P_{\text{source}}(x, y, z, t) = A \sin(\omega t)\delta(y), \tag{3-47}$$

which generates a plane wave coming from the bottom of the domain. The obstacle is defined
by imposing certain pressure value in the cells it occupies and allow the lattice-Boltzmann
scheme to evolve only outside the obstacle. (A more detailed, formal and accurate way to
include obstacles in a lattice-Boltzmann method for waves was also developed by us and is
described in Chapter 7.

For the next example we put a slit at $y = Ly/4$ with a 5 cells width hole. The results of the
simulation Fig. **3-4** show that the initially generated plane wave becomes circular due to the
effect of the slit, i.e. the wave is diffracted by the obstacle.
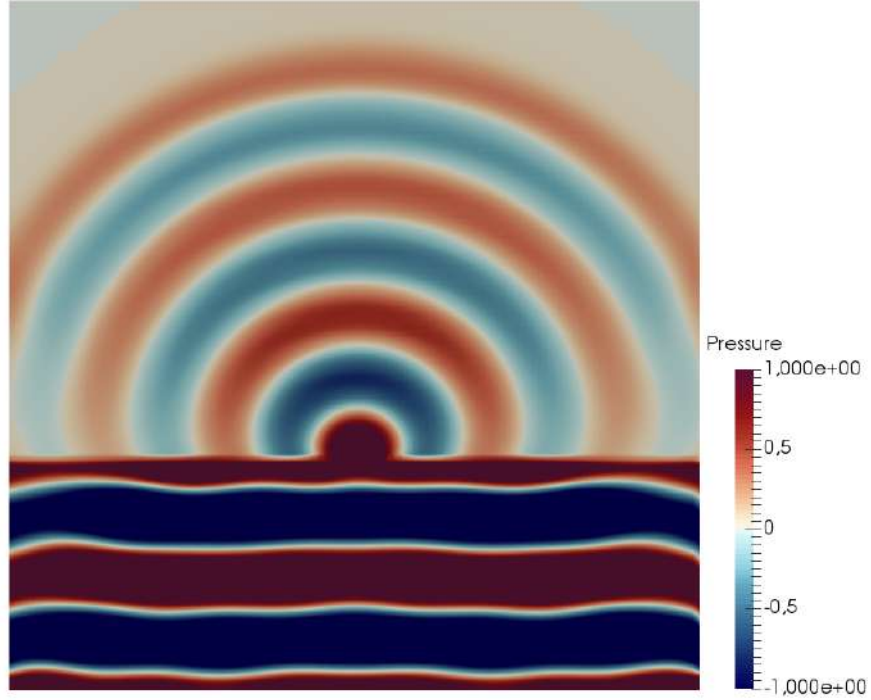
Figure 3-4.: Plane wave is diffracted while it crosses a hole, its frontwave becomes circular. $t = 150$ time-steps

Next, we place two point sources at the bottom through the condition

$$P_{\text{source}}(x, y, z, t) = A\sin(\omega t)\delta(y)(\delta(x - L_x/4) + \delta(x - 3L_x/4)), \tag{3-48}$$

As shown in Fig. **3-5** the two circular waves interact each other and generate an interference pattern.
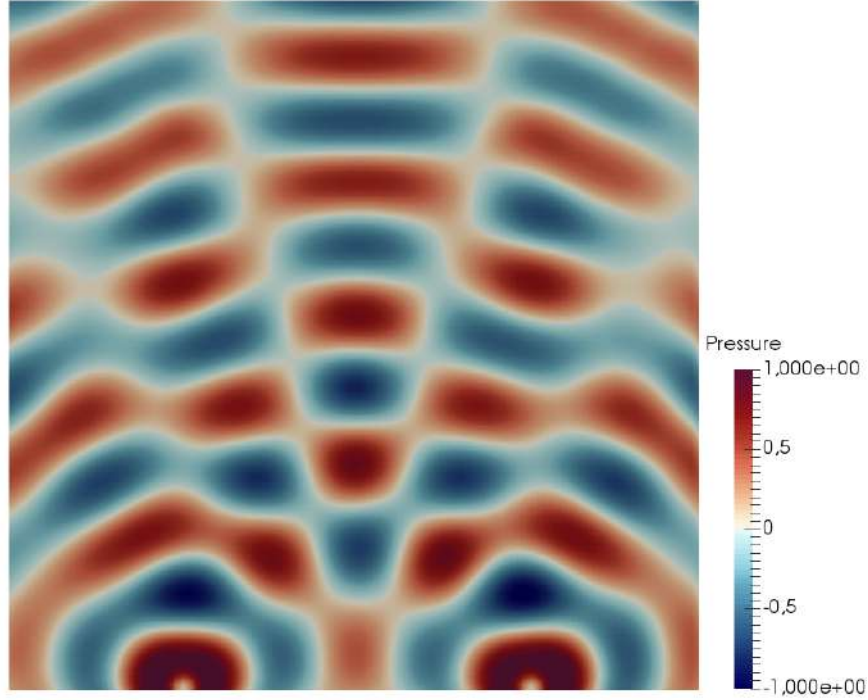
Figure 3-5.: Two circular waves evolving from the bottom show an interference pattern.

One important feature of the LBM for mechanical waves is that we can set individually the wave speed c at each cell, this allow us to simulate medium with different refractive index and refraction processes, in the next simulation, we set c according with the relation

$$c = \begin{cases} 0.32 & \text{if } y \geq \frac{x}{2} + \frac{L_x}{5} \\ 0.34 & \text{if } y < \frac{x}{2} + \frac{L_x}{5} \end{cases} \tag{3-49}$$

the line $y = \frac{x}{2} + \frac{L_x}{5}$ becomes an interface between the two different media. Results are shown in Fig. **3-6**, the circular wave is distorted due to the appearance of the second medium, as expected, the frequency of the wave is greater in the medium with greater propagation speed.
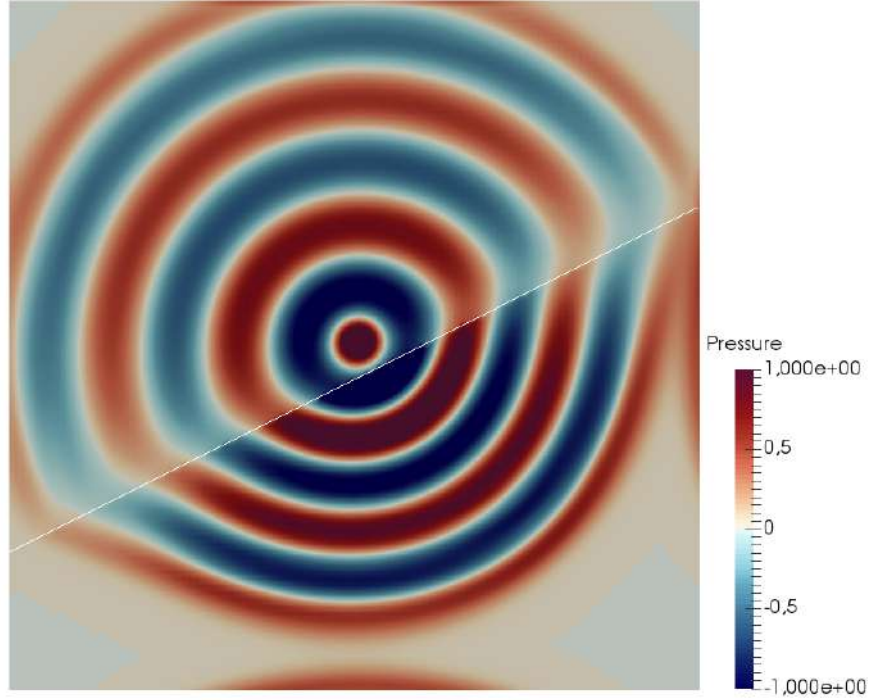
Figure 3-6.: A circular wave is refracted when crosses an interface to a medium where the propagation velocity is lower. $t = 200$ times-steps

Finally, we define a time dependent pressure source given by the equation

$$P_{\text{source}}(x, y, z, t) = A \sin(\omega t)\delta(y - L_y/2 - vt)\delta(x - L_x/2) , \tag{3-50}$$

where v is the speed of the moving source along the y direction. For the simulation shown in **3-7**, this velocity is lower than the wave propagation speed $v < c$. Note the frequency increase in the direction of the source movement and the decrease in the opposite direction as expected.
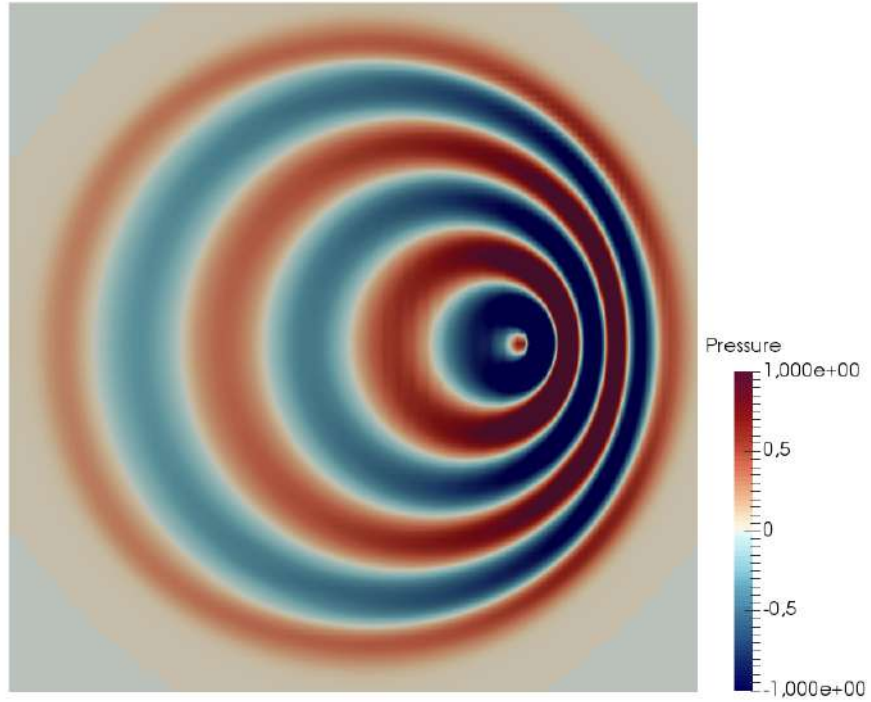
Figure 3-7.: A travelling point source shows the Doppler effect, an increase of the wave frequency in the direction of movement. $t = 200$ time-steps

4. LBM for acoustics in curvilinear Coordinates. Special Case: Symmetric Systems

4.1. Introduction

Since the theoretical derivation for lattice-Boltzmann assume an homogeneous and isotropic set of velocity vectors to move the information from node to node, the computational domain has been restricted to a rectangular array of cubic cells, forcing the use of staircase approximations on curved boundaries and imposing three-dimensional models for systems that, because of axial or spherical symmetries, were essentially two-dimensional, with an exorbitant increase in computational costs.

Various approaches have been proposed to overcome this problem. One of the first proposals was made by Nannelli and Succi in 1992 [7], consisting in a finite volume solution in two dimensions of the kinetic Boltzmann equation where the cells can be irregular quadrilaterals; but this scheme introduces a new coarse-grained distribution function (averaging the standard lattice-Boltzmann distributions) that should be retrieved through additional interpolation steps. Later, in 1997, He and Doolen [8] implemented a lattice-Boltzmann scheme in polar coordinates based on an algorithm proposed by He, Luo and Dembo [35], where that additional interpolation step is still required. In 1998 a grid refinement scheme with boundary-fittings for complicated geometries was proposed by Filippova and Hänel [36]. In this work, smaller cells are located in regions where a higher resolution is needed. Even though this strategy reduces some computational costs, the staircase approximation does not disappear and some interpolations on the curved boundaries of complex systems are still needed. Up to now, the implementation of lattice-Boltzmann models in curved general geometries has been a hard task, not only because of the insertion of additional computing steps, but mainly because each new geometry needs a new cautious discretization scheme to ensure a correct definition of the boundary conditions.

In 2010 and 2015 Li *et. al.*[9] and Reijers, Gelderblom and Toschi,[10] respectively develop a lattice-Boltzmann scheme for fluid mechanics to be implemented in axisymmetric coordinate systems. Reijers constructed a bi-phasic lattice-Boltzmann model capable to achieve density ratios up to 1000 and used it to study the propagation of pressure waves in such coordinates, but finding an excessive dissipation due to the lattice-Boltzmann viscosity. In

2012 a more general approach was developed by Budinsky for the two-dimensional shallow water and Navier-Stokes equations[11]. In that scheme, the equations are written in general coordinates, and the additional geometric terms (written in terms of the Jacobian and Jacobian spacial derivatives) are introduced as forcing terms in the collision. The main advantage of this model is that all information about the curvilinear coordinate system is included in the equilibrium distribution function and the forcing term, and no further discretization or interpolation steps are needed.

Simultaneously with the Budinsky proposal, in his doctoral thesis, M. Mendoza [12] introduced a new strategy to built lattice-Boltzmann models for fluids on any curvilinear coordinate system. The strategy takes into account how volumes and velocity vectors change from cell to cell by including the metric tensor and Christoffel symbols for those coordinates both in the equilibrium functions and as additional forcing terms. This strategy does not require neither a specific discretization scheme for each problem nor additional interpolation steps. Furthermore, since the geometry can be modified just by changing the metric tensor and Christoffel symbols, it would be possible to run simulations even on dynamical geometries. This model has been successfully used to study the Dean's instability in ellipsoidal coordinates [37], flows through randomly curved media [38], and, more recently, energy dissipations due to curvature [39].

In this chapter we extend the model by Chopard *et. al* [28, 32] to simulate acoustic waves on generalized coordinates by following the proposal of M. Mendoza [12]. Section 4.2 introduces the wave equation in generalized coordinates and how it can be recovered from two conservation laws by following a similar procedure to the one in Chapter 3. The procedure includes now a redefinition of the macroscopic fields and the inclusion of a forcing term. Section 4.3 performs a Chapman-Enskog expansion to determine the exact form of the forcing term to retrieve the desired conservation laws in the macroscopic limit. The only remaining step is to define the equilibrium distribution functions (Sec. 4.4). That, however, was not an easy task, and three different approaches were proposed and tested. The first one, described in Subsection 4.4.1 is analogous to the moment matching procedure described in Chapter 3. This model is the easiest to construct, but it is just first order in accuracy and it was only stable for systems with axial symmetry. A second form of the equilibrium distribution function was obtained via Hermite polynomials expansion (Subsection 4.4.2), giving us a more stable model with second order accuracy that allow us to perform simulations without axial symmetry. Nevertheless, it can be shown that using a D3Q7 velocity scheme does not maintain the isotropy of the system. The isotropy will be recovered in a third approach, by modifying the obtained equilibrium distribution function and defining an additional forcing term. The resulting model, which is briefly described in Subsection 5.1, will be used thereafter in this work and will be studied in more detail in the next chapters.

4.2. Macroscopic Equations

The wave equation in general coordinates reads

$$\frac{\partial^2 P}{\partial t^2} - \frac{c^2}{\sqrt{g}}\partial_\alpha\left(\sqrt{g}g^{\alpha\beta}\partial_\beta P\right) = 0 \quad, \tag{4-1}$$

where g^{kl} is the inverse of the metric tensor of the geometry and g its determinant. Here, the second term is the explicit definition of the Laplace-Beltrami operator applied on the scalar quantity P. The spatial differential operators of the corresponding conservation laws must be also defined in general coordinates. The gradient of a scalar function and the divergence of a vector or tensor field are given by [40]

$$(\nabla P)^\alpha = \partial^\alpha P = g^{\alpha\beta}\partial_\beta P \quad, \tag{4-2}$$

$$\nabla \cdot \vec{J} = \frac{1}{\sqrt{g}}\partial_\alpha(\sqrt{g}J^\alpha) \quad, \tag{4-3}$$

$$\nabla_\beta\left(\Pi^{(0)}\right)^{\alpha\beta} = \frac{1}{\sqrt{g}}\partial_\beta\left(\sqrt{g}\left(\Pi^{(0)}\right)^{\alpha\beta}\right) + \Gamma^\alpha_{\beta\gamma}\left(\Pi^{(0)}\right)^{\beta\gamma} \quad; \tag{4-4}$$

therefore, a proper extension to general coordinates of the conservation laws found in Chapter 3 ((3-15) and (3-16)) is

$$\frac{\partial\left(\sqrt{g}P\right)}{\partial t} + \partial_\alpha(\sqrt{g}J^\alpha) = 0 \quad, \tag{4-5}$$

$$\frac{\partial\left(\sqrt{g}J^\alpha\right)}{\partial t} + \partial_\beta\left(\sqrt{g}\left(\Pi^{(0)}\right)^{\alpha\beta}\right) = -\Gamma^\alpha_{\beta\gamma}\left(\Pi^{(0)}\right)^{\beta\gamma}\sqrt{g} \quad. \tag{4-6}$$

Note that, if we redefine the standard lattice-Boltzmann macroscopic quantities (the first moments of the distribution functions) such that $P \to \sqrt{g}P$, $\vec{J} \to \sqrt{g}\vec{J}$ and $\Pi \to \sqrt{g}\Pi$, Eqs. (4-5) and (4-6) has the same functional form of Eqs. (3-15) and (3-16) plus an additional source term in Eq. (4-6). This fact suggests that we can use a standard lattice-Boltzmann method on Cartesian coordinates to simulate systems described in general coordinates without changing the discretization scheme. The only modification required would be the inclusion of an additional forcing term.

Let us point out that, if we would find an equilibrium distribution function such that the stress tensor were

$$\left(\Pi^{(0)}\right)^{\alpha\beta} = c^2 P g^{\alpha\beta} \tag{4-7}$$

Eq.(4-6) would be

$$\frac{\partial \left(\sqrt{g} J^\alpha \right)}{\partial t} = -\partial_\beta \left(\sqrt{g} c^2 P g^{\alpha\beta} \right) - \Gamma^\alpha_{\beta\gamma} c^2 P g^{\beta\gamma} \sqrt{g} \quad . \tag{4-8}$$

By taking the time derivative of Eq. (4-5),

$$\frac{\partial^2 \left(\sqrt{g} P \right)}{\partial t^2} + \partial_\alpha \left(\frac{\partial \left(\sqrt{g} J^\alpha \right)}{\partial t} \right) = 0 \quad , \tag{4-9}$$

the left hand side of Eq. (4-8) can be replaced in the second term of Eq. (4-9) to obtain

$$\frac{\partial^2 \left(\sqrt{g} P \right)}{\partial t^2} - c^2 \partial_\alpha \left(\partial_\beta \left(\sqrt{g} P g^{\alpha\beta} \right) + \Gamma^\alpha_{\beta\gamma} g^{\beta\gamma} \sqrt{g} P \right) = 0 \quad . \tag{4-10}$$

This is exactly the wave equation in general coordinates (Eq. 4-1) we want to reproduce.

Next, because the macroscopic fields P, $\vec{J}$ and $\Pi^{(0)}$ in Eq. (4-9) and (4-10) appear multiplied by $\sqrt{g}$, let us redefine the statistical moments of the distribution functions as

$$\sqrt{g} P = \sum_i f_i^{eq} \quad , \tag{4-11}$$

$$\sqrt{g} J'^\alpha = \sum_i f_i^{eq} \xi_i^\alpha - \frac{\delta_t}{2} c^2 P \Gamma^\alpha_{\beta\gamma} g^{\beta\gamma} \sqrt{g} \quad , \tag{4-12}$$

$$\sqrt{g} \left(\Pi^{(0)} \right)^{\alpha\beta} = \sum_i f_i^{eq} \xi_i^\alpha \xi_i^\beta = \sqrt{g} c^2 P g^{\alpha\beta} . \tag{4-13}$$

The additional term in the macroscopic quantity $\vec{J}'$ comes from the forcing term of the conservation law (Eq. (4-6)), by following the approach of Guo _et. al._ [41]. We explain the procedure obtain the forcing term for our particular case in Sec. 4.3.

4.3.   Forcing terms

The strategy we chose to discretize the system is to maintain in the computer a standard cubic lattice with a uniform velocity set to storage the information. Thus, the Chapman-Enskog expansion for this model can be performed in that cubic space, but keeping in mind that such cubic lattice transports information between nodes placed on curved lines in the real world (Fig. **4-1**). In consequence, the only modification of the standard Chapmann-Enskog expansion described in 3.2.1 is related with the inclusion a forcing term to recover the second term in the right hand side of Eq. (4-12). In this section, we describe the procedure

to find that forcing term by following both the approach proposed by Kruger *et. al.* [34] to discretize the continuous forcing term and the Chapmann-Enskog expansion performed by Guo *et. al.* [41] to find its functional form.
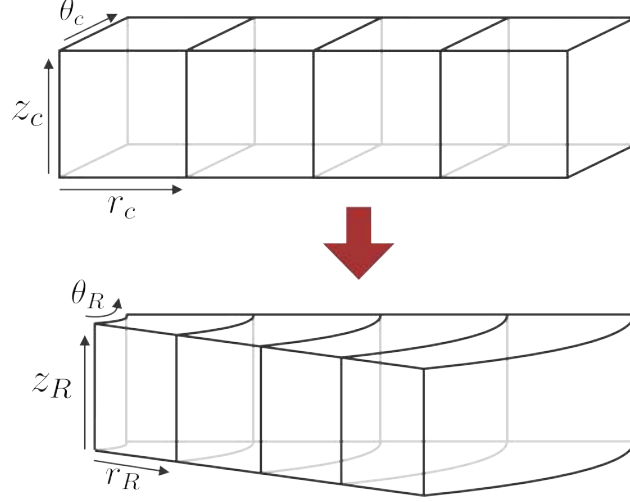

Figure 4-1.: Coordinates redefinition and transformation where the subscript C (R) indicates computer (real) coordinates

First, let us consider the continuous Boltzmann equation in Cartesian coordinates, but including a forcing term

$$\frac{\partial f}{\nabla t} + \xi^{\alpha} \nabla_{\alpha} f + \mathcal{F} \partial_{\xi^{\alpha}} f = \Omega\left(f\right) \quad . \tag{4-14}$$

Again, we want to discretize this continuous equation in the velocity space by using the properties of the Hermite Polynomials, but focusing in the forcing term. To this aim we recall the expression of a Hermite series expansion for a given function f (Eq. (3-38))

$$f\left(\vec{\xi}\right) \approx w\left(\vec{\xi}\right) \sum_{n=0}^{N} \frac{1}{n!} \vec{a}^{(n)} \cdot \vec{\mathcal{H}}^{(n)}\left(\vec{\xi}\right) = \sum_{n=0}^{N} \frac{(-1)^{n}}{n!} \vec{a}^{(n)} \cdot \nabla_{\xi}^{n} w\left(\vec{\xi}\right) \quad , \tag{4-15}$$

where we employed the expression $w(\vec{\xi})\mathcal{H}^{(n)} = (-1)^{n} \nabla_{\xi}^{n} w(\vec{\xi})$. By using the Eq. (4-15) we can also find an expansion for the third term of Eq. (4-14),

$$\vec{\mathcal{F}} \nabla_{\xi_{\alpha}} f \approx \vec{\mathcal{F}} \sum_{n=0}^{N} \frac{(-1)^{n}}{n!} \vec{a}^{(n)} \cdot \nabla_{\xi}^{n+1} w\left(\vec{\xi}\right) = -\vec{\mathcal{F}} w\left(\vec{\xi}\right) \sum_{n=1}^{N} \frac{n}{n!} \vec{a}^{(n-1)} \cdot \mathcal{H}^{(n)}\left(\vec{\xi}\right) , \tag{4-16}$$

where we have truncated the expansion up to order N. This expression let us to write a discrete forcing term F_{i} (in velocity space) by following the same procedure we used to found the discrete version of the continuous equilibrium distribution function in Sec. 3.2.2. So,

$$F_{i}\left(\vec{x}, t\right) = -\frac{w_{i}}{w(\vec{\xi})} \vec{\mathcal{F}} \cdot \nabla_{\xi} f|_{\xi_{i}} \quad , \tag{4-17}$$

where $\cdot\nabla_\xi f|_{\xi_i}$ indicates that the term is evaluated at the discrete velocities $\vec{\xi_i}$; therefore, we can write the Boltzmann equation on the discrete velocity set as

$$\partial_t f_i + \xi_i^\alpha \partial_\alpha f_i = \Omega_i + F_i \,. \tag{4-18}$$

The next step is to discretize this equation in the space and time.

The left side of the equation can be expanded as usual, obtaining

$$\partial_t f_i + \xi_i^\alpha \partial_\alpha f_i = f_i\left(\vec{x} + \vec{\xi_i}\delta_t,\, t + \delta_t\right) - f_i\left(\vec{x},\, t\right) \,, \tag{4-19}$$

while the collision term can be discretized by using a trapezoidal rule, that is

$$\int_t^{t+\delta_t} \Omega_i + F_i d\zeta = \left(\frac{\Omega_i\left(\vec{x},\, t\right) + \Omega_i\left(\vec{x} + \vec{\xi_i}\delta_t,\, t + \delta_t\right)}{2} + \frac{F_i\left(\vec{x},\, t\right) + F_i\left(\vec{x} + \vec{\xi_i}\delta_t,\, t + \delta_t\right)}{2}\right)\delta_t \,. \tag{4-20}$$

Eqs. (4-19) and (4-20) lead to

$$f_i\left(\vec{x} + \vec{\xi_i}\delta_t,\, t + \delta_t\right) - f_i\left(\vec{x},\, t\right) = \left(\frac{\Omega_i\left(\vec{x},\, t\right) + \Omega_i\left(\vec{x} + \vec{\xi_i}\delta_t,\, t + \delta_t\right)}{2}\right. \\ \left. + \frac{F_i\left(\vec{x},\, t\right) + F_i\left(\vec{x} + \vec{\xi_i}\delta_t,\, t + \delta_t\right)}{2}\right)\delta_t \,. \tag{4-21}$$

Even though it is a time-implicit scheme, it that can be transformed into an explicit one through the change of variables

$$\bar{f}_i = f_i - \delta_t \frac{\Omega_i + F_i}{2} \,, \tag{4-22}$$

obtaining

$$\bar{f}_i\left(\vec{x} + \vec{\xi_i}\delta_t,\, t + \delta_t\right) - \bar{f}_i\left(\vec{x},\, t\right) = -\frac{\delta_t}{\bar{\tau}}\left[\bar{f}_i\left(\vec{x},\, t\right) - f_i^{eq}\left(\vec{x},\, t\right)\right] + \left(1 - \frac{\delta_t}{2\bar{\tau}}\right)\delta_t F_i \,, \tag{4-23}$$

where $\bar{\tau} = \tau + \delta_t/2$. With this change of variables, the macroscopic fields are now defined as

$$\sqrt{g}P' = \sum_i \bar{f}_i + \frac{\delta_t}{2}\sum_i F_i \quad, \tag{4-24}$$

$$\sqrt{g}J'^\alpha = \sum_i \bar{f}_i\xi_i^\alpha + \frac{\delta_t}{2}\sum_i \xi_i^\alpha F_i \quad, \tag{4-25}$$

$$\sqrt{g}\left(\Pi'^{(0)}\right)^{\alpha\beta} = \left(1 - \frac{\delta_t}{2\bar{\tau}}\right)\delta_t\sum_i \bar{f}_i\xi_i^\alpha\xi_i^\beta + \frac{\delta_t}{2\bar{\tau}}\sum_i f_i^{eq}\xi_i^\alpha\xi_i^\beta + \frac{\delta_t}{2\bar{\tau}}\left(1 - \frac{\delta_t}{2\bar{\tau}}\right)\sum_i F_i\xi_i^\alpha\xi_i^\beta. \quad (4\text{-}26)$$

Note that if we set $\bar{\tau} = 0.5$ to simulate the wave equation as before, the discrete forcing term no longer appears in Eq. (4-23) and we recover the definition of the stress tensor

$$\sqrt{g}\left(\Pi'^{(0)}\right)^{\alpha\beta} = \sum_i f_i^{eq}\xi_i^\alpha\xi_i^\beta \quad (4\text{-}27)$$

Hereafter, we will skip the bar in the new variables to simplify the notation. Guo *et.al.* [41] uses a similar expression to Eq. (4-17) to propose a general form of the discrete force

$$F_i = w_i\left[A + \frac{\vec{B}\cdot\vec{\xi_i}}{c_s^2} + \frac{\mathbb{C}:(\vec{\xi_i}\vec{\xi_i} - c_s^2\mathbb{I})}{2c_s^4}\right]. \quad (4\text{-}28)$$

By fixing $\tau = 0.5$, we obtain

$$F_i = w_i\left[\frac{\vec{\mathcal{F}}\cdot\vec{\xi_i}}{c_s^2}\right], \quad (4\text{-}29)$$

The first three moments of F_i can be easily computed using the relations 3-1

$$\sum_i F_i = 0, \quad (4\text{-}30)$$

$$\sum_i F_i\xi_i^\alpha = \mathcal{F}^\alpha, \quad (4\text{-}31)$$

$$\sum_i F_i\xi_i^\gamma\xi_i^\delta = 0. \quad (4\text{-}32)$$

With these results, Eqs. (4-24) and (4-25) become

$$\sqrt{g}P' = \sum_i f_i^{eq}, \quad (4\text{-}33)$$

$$\sqrt{g}J'^\alpha = \sum_i f_i^{eq}\xi_l^\alpha + \frac{\delta_t}{2}\mathcal{F}^\alpha. \quad (4\text{-}34)$$

The remaining part in our construction is to find the functional form of $\vec{\mathcal{F}}$ such that we can retrieve the wave equation in general coordinates Eq. (4-1), which is equivalent to recover Eqs. (4-5) and (4-6). To this aim, we perform again the Chapman-Enskog expansion of 3.2.1 but including the forcing term as defined above (Eq.(4-29)) and the new definitions of the macroscopic variables, (Eqs. (4-33), (4-34) and (4-27)). For the first three orders in the Knudsen number ϵ we obtain:

- 0th order:

$$f_i^{(0)} = f_i^{(eq)} \quad , \tag{4-35}$$

- 1st order:

$$-\frac{1}{\tau} f_i^{(1)} + \delta_t F_{i1} = \delta_t \left[\frac{\partial}{\partial t_1} + \vec{\xi}_i \cdot \vec{\nabla}_1 \right] f_i^{(0)} \quad , \tag{4-36}$$

- 2nd order:

$$-\frac{1}{\tau} f_i^{(2)} - \frac{\delta_t^2}{2!} \left[\frac{\partial}{\partial t_1} + \vec{\xi}_i \cdot \vec{\nabla}_1 \right] F_{i1} = \delta_t \frac{\partial}{\partial t_2} f_i^{(0)} \quad , \tag{4-37}$$

where we have assumed that the discrete forcing term $F_{i1} = \epsilon F_{i1}$ is first order in ϵ [41]. By following the approach by Guo $et.$ $al.$, let us add Eq.(4-36) over i to obtain

$$\frac{\partial \left(\sqrt{g} P \right)}{\partial t_1} + \partial_{1\alpha} (\sqrt{g} J'^{\alpha}) = 0 \, , \tag{4-38}$$

and multiply (4-36) by $\vec{\xi}$ before adding on i gives (4-39),

$$\frac{\partial \left(\sqrt{g} J'^{\alpha} \right)}{\partial t_1} + \partial_{1\beta} \left(\sqrt{g} \left(\Pi^{(0)} \right)^{\alpha\beta} \right) = \left(\frac{1}{2\tau} \right) \mathcal{F}_1^{\alpha} \, . \tag{4-39}$$

Similarly, by considering Eq. (4-37) instead, we have

$$\frac{\partial \sqrt{g} P}{\partial t_2} = 0 \tag{4-40}$$

and

$$\frac{\partial \left(\sqrt{g} J'^{\alpha} \right)}{\partial t_2} = 0 \quad . \tag{4-41}$$

Next, by adding Eq. (4-38) plus Eq.(4-40) and Eq. (4-39) plus Eq.(4-41) we recover the desired conservation laws (Eqs. (4-5) and (4-6))

$$\frac{\partial \left(\sqrt{g} P \right)}{\partial t} + \partial_{\alpha} (\sqrt{g} J'^{\alpha}) = 0 \quad , \tag{4-42}$$

$$\frac{\partial \left(\sqrt{g} J'^{\alpha} \right)}{\partial t} + \partial_{\beta} \left(\sqrt{g} \left(\Pi^{(0)} \right)^{\alpha\beta} \right) = \mathcal{F}^{\alpha} \quad , \tag{4-43}$$

with

$$\mathcal{F}^{\alpha} = -\Gamma_{\beta\gamma}^{\alpha} \left(\Pi^{(0)} \right)^{\beta\gamma} \sqrt{g} = -\Gamma_{\beta\gamma}^{\alpha} c^2 P g^{\beta\gamma} \sqrt{g} \, . \tag{4-44}$$

The second moment of the equilibrium distribution function is, therefore,

$$\sqrt{g} J'^{\alpha} = \sum_i f_i^{eq} \xi_i^{\alpha} - \frac{\delta_t}{2} c^2 P \Gamma_{\beta\gamma}^{\alpha} g^{\beta\gamma} \sqrt{g} \quad , \tag{4-45}$$

which is exactly the Eq. (4-12).

4.4. Equilibrium distribution function

Once we found the conservation laws that lead to the macroscopic equation in general coordinates and the functional form of the forcing term which allow us to retrieve the conservation laws, the problem reduces now to find equilibrium distribution functions such that Eq. (4-11),(4-12) and (4-13) hold. As we mentioned at the beginning of this Chapter, we constructed three different approaches to the equilibrium distribution function. In the following section we describe and test two of them, leaving the third one to the next Chapter.

4.4.1. By Moment Matching

Our first approach consisted in building an equilibrium distribution function from an Ansatz and setting the constants to retrieve the macroscopic equations. This is the moment matching procedure described in Chapter 3. Let us propose the Ansatz

$$f_i^{eq} = w_i \left[A + \frac{\vec{B} \cdot \vec{\xi}_i}{c_s^2} + \frac{\mathbb{C} : (\vec{\xi}_i \vec{\xi}_i - c_s^2 \mathbb{I})}{2c_s^4} \right] , \tag{4-46}$$

which corresponds again to a power series in $\vec{\xi}$. We can use the definitions of the macroscopic variables Eqs. (4-11), (4-12) and (4-13) to find the coefficients. Let us start by computing the tensor $\Pi^{(0)}$,

$$\sqrt{g}\Pi^{(0)\gamma\delta} = \sum_i f_i^{eq} \xi_i^\gamma \xi_i^\delta = \sum_i w_i \left[A\xi_i^\gamma \xi_i^\delta + \frac{B^\alpha \xi_i^\alpha \xi_i^\gamma \xi_i^\delta}{c_s^2} + \frac{C^{\gamma\delta}}{2c_s^4} \left(\xi_i^\alpha \xi_i^\beta \xi_i^\gamma \xi_i^\delta - c_s^2 \xi_i^\gamma \xi_i^\delta \delta^{\alpha\beta} \right) \right]$$

$$= A \sum_i w_i \xi_i^\gamma \xi_i^\delta + \frac{C^{\gamma\delta}}{2c_s^4} \left(\sum_i w_i \xi_i^\alpha \xi_i^\beta \xi_i^\gamma \xi_i^\delta - c_s^2 \delta^{\alpha\beta} \sum_i w_i \xi_i^\gamma \xi_i^\delta \right) . \tag{4-47}$$

Note that if we set $A = 0$ and $C^{\gamma\delta} = c^2 P g^{\gamma\delta}$, we have

$$\sqrt{g}\Pi^{(0)\gamma\delta} = \sum_i f_i^{eq} \xi_i^\gamma \xi_i^\delta = \sqrt{g}c^2 P g^{\gamma\delta} \tag{4-48}$$

as desired. Secondly, for the quantity $\vec{J}$,

$$\sqrt{g}J^\gamma = \sum_i f_i^{eq} \xi_i^\gamma = \sum_i w_i \left[\frac{B^\alpha \xi_i^\alpha \xi_i^\gamma}{c_s^2} \right]$$

$$= B^\alpha c_s^2 \delta^{\alpha\gamma} . \tag{4-49}$$

Thus, $B^\alpha = J^\alpha$ and the equilibrium distribution function obtained through this approach is

$$f^{eq} = \begin{cases} w_0\sqrt{g}P \left[\frac{1}{w_0} - \frac{c^2}{2c_s^2}g^{\alpha\alpha} \right] & \text{for } i = 0 \\ \frac{w_i\sqrt{g}}{c_s^2} \left[\vec{\xi}_i \cdot \vec{J}' + \frac{c^2}{2c_s^2}P\xi_i^\alpha g^{\alpha\beta} \xi_i^\beta - \frac{1}{2}Pc^2 g^{\alpha\alpha} \right] & \text{otherwise} \end{cases} , \tag{4-50}$$

where the value for f_0^{eq} has been obtained, as usual, from

$$f_0^{eq} = \sqrt{g}P - \sum_{i=1}^{\lambda} f_i^{eq}.$$
(4-51)

To test this model we perform two benchmarks. First, we tested the isotropic propagation of two-dimensional waves on rectangular cells. For this aim we choose the coordinate transformation

$$\begin{aligned} x &= \Delta_x i_x \\ y &= \Delta_y i_y \end{aligned}$$
(4-52)

where i_x and i_y are the integer indexes of the nodes in each direction and $\Delta_x = 0.8\Delta_y$. The geometric properties of this transformation, i.e. the metric tensor and the Christoffel symbols, can be found in Appendix C. Fig. 4-2 shows the wavefronts generated by a point source of sinusoidal pressure evolving on a rectangular grid.
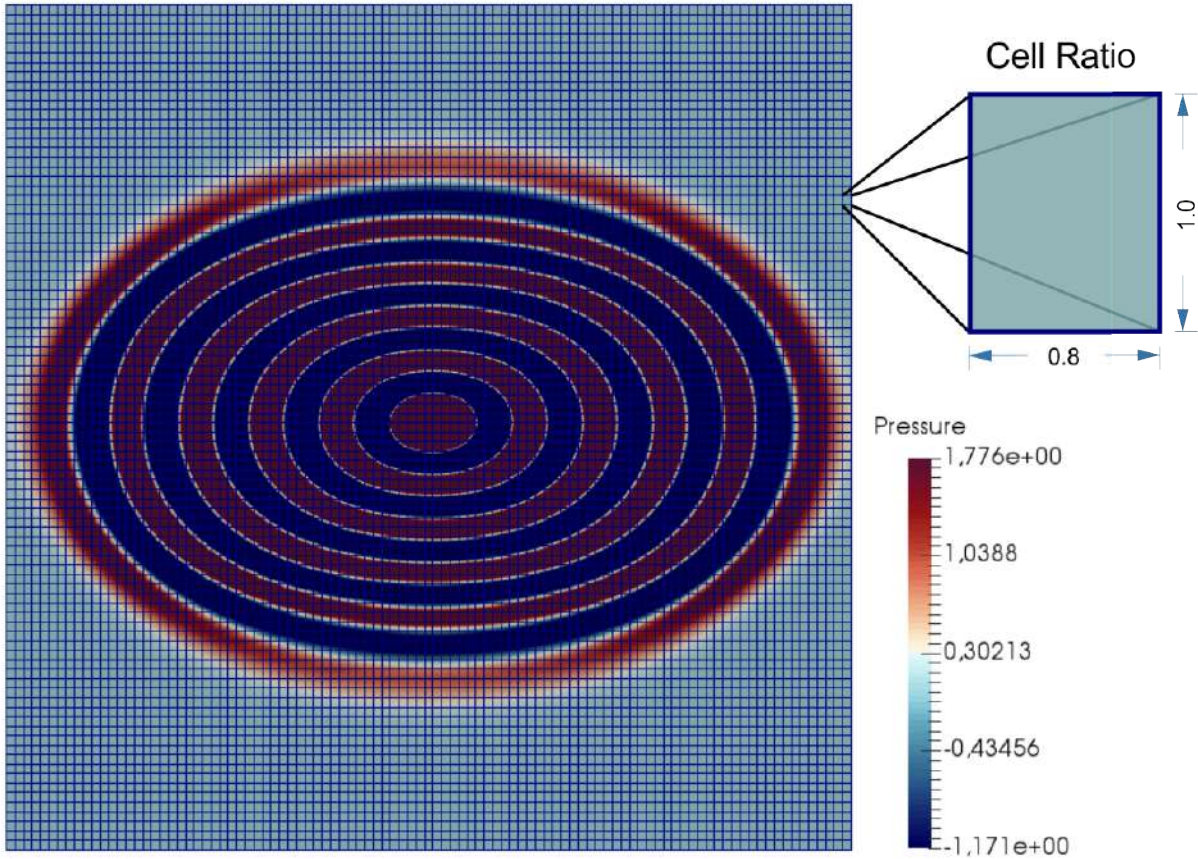

Figure 4-2.: Test of isotropic propagation in a rectangular grid for the LBM with f_i^{eq} found from the Moment Matching procedure.

We observe that the propagation of the wave is not isotropic. Although it tends to propagate faster in the direction where the cells are smaller, as expected, the effect is larger than required to maintain the isotropy. The reason why this model fails to recover an isotropic propagation in real space will be shown in Sec. 5.1.

Despite the lack of isotropy, this model has shown to be successful in modelling systems with axial symmetry and with approximately the same cell size in all directions. For example, it correctly simulates a radial wave in polar coordinates, as shown in Fig.**4-3**. For this simulation we choose an array of $500 \times 1 \times 1$ cells (i. e. the problem can be treated as one-dimensional in r) with periodic boundary conditions in the angular and axial directions (θ and z) and free boundary conditions in $r = 500$. This last boundary condition is achieved by copying to the boundary cell the distribution functions of the neighbouring cell normal to the boundary. In this case, $r_{min} = 1$ was chosen as the minimum value of r that is simulated due to the indetermination of the cylindrical coordinates at $r = 0$. Therefore, the functional form of the source is

$$P_{source}(r, \theta, z, t) = C \sin(\omega t) \, \delta(r - r_{\min}) \quad , \tag{4-53}$$

where δ is the Dirac's delta.

The analytical solution corresponds to a Bessel function $\mathcal{J}_0$,

$$P(r, \theta, z) = A \mathcal{J}_0(R_{max} r) \approx \frac{A}{\sqrt{r}} \cos(r \pm vt) \quad . \tag{4-54}$$

The simulated pressure profile perfectly agrees with the analytical solution (Fig. **4-3**). Note how an originally two-dimensional problem in Cartesian coordinates can be handled as one-dimensional by choosing a proper coordinate system that takes advantage of the system symmetries. This is only possible because our model is defined on generalized coordinates.
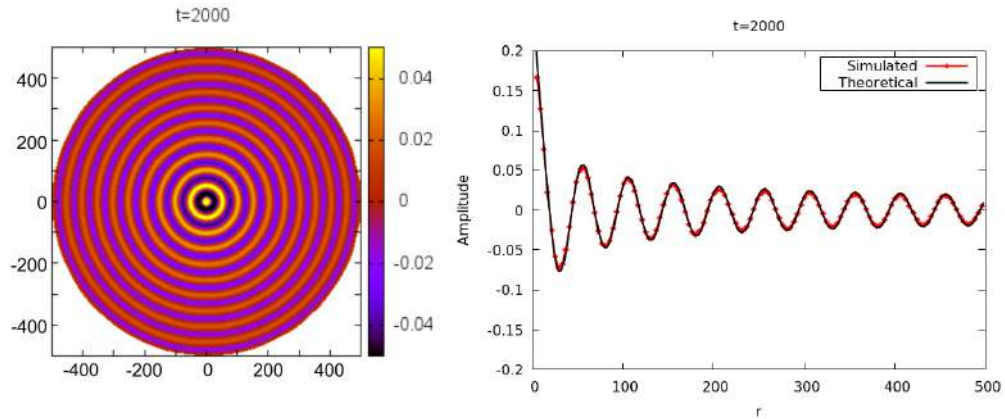

Figure 4-3.: Evolution of a point pressure source in the middle of a circular domain for 2000 times steps (left), simulated pressure profile compared with the theoretical expectation (right).

Next, we used this model to simulate pressure waves inside a pipe with an open end, like a flute, by using cylindrical coordinates. In this case the dimensions of the pipe are $200 \times 2\pi \times 1200$ in the continuous space (r, θ, ϕ) and $20 \times 4 \times 100$ cells respectively. The boundary conditions are the shown in Fig. **4-4**. The bounce back condition is defined by

$$f_{i_{out}} \left(\vec{x}_{\text{wall}}, \vec{\xi}_{out}, t \right) = D \cdot f_{i_{in}} \left(\vec{x}_{\text{wall}}, \vec{\xi}_{in}, t \right) \quad , \tag{4-55}$$

where $D > 1$ is a damping factor needed to add dissipation in the simulation, which is required to reach steady-stable oscillations after a transient. The indexes *in* and *out* are for the incident and reflected directions, respectively.

The source used for this simulation is

$$P_{source}(r, \theta, z, t) = C \sin(\omega t)\delta(r - r_{min})\delta z \tag{4-56}$$

with $r_{min} = 2$. This is an oscillating ring placed at the left end of the pipe with radius r_{min}. This choice allows the waves to have both radial and longitudinal modes but preserving the axial symmetry.
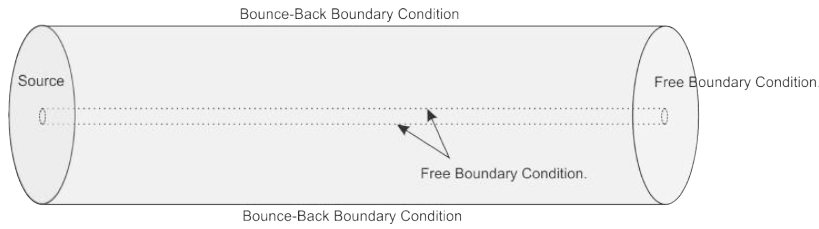

Figure 4-4.: Boundary conditions for the simulation of a wave inside a pipe

In addition, we identified the characteristic frequencies of the pipe by measuring the pressure at a sensing point near to the source for a range of frequencies in $0 < \omega < 0.3$. The theoretical values of these frequencies are found in Appendix B. Fig. **4-5** shows the pressure waves for a given frequency at $t = 8400$ timesteps and the intensities at the sensing point on the chosen frequency range. The frequency peaks are in good agreement with the expected values. More details of this simulations are described in Chapter 5.
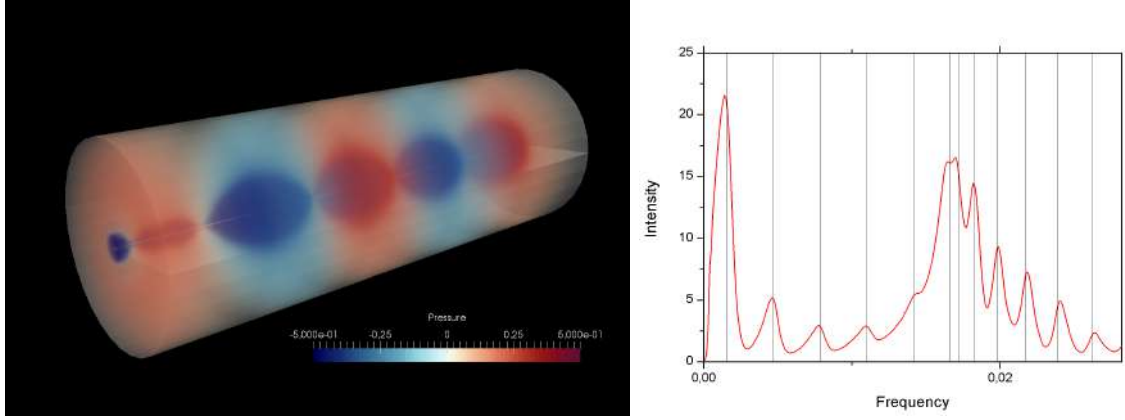
Figure 4-5.: Pressure waves inside a closed-open end pipe by using the f_i^{eq} found from the Moment Matching procedure. Pressure values after 8400 time steps (left). Pressure intensities at a sensing point close to the source on the frequency range $0 < \omega < 0.3$, the black vertical lines correspond to the theoretical natural frequencies (right).

Summarizing, this model can be used to simulate waves in general coordinates, but for systems with strong symmetries and with similar cell sizes in different directions. If not, the propagation is not isotropic.

4.4.2. By Hermite Polynomials

As a second approach, we extended the procedure shown in Sec. 3.2.2 to general coordinates. It consists in expanding the continuous equilibrium distribution in a series of Hermite polynomials. For our case, the continuous equilibrium function is

$$f^{eq}\left(\vec{\xi}\right) = \frac{P}{(\sqrt{2\pi RT})^D}\mathrm{e}^{-(\xi^\alpha(cg^{\alpha\beta}-c_s\delta^{\alpha\beta})\xi^\beta/2RT} \, , \tag{4-57}$$

which is just Eq. (3-32) written in general coordinates. The Hermite polynomials (Eq. (3-42)) remain unchanged. The new coefficients of the expansion (Eq. (3-41)) are

$$\begin{aligned}
a_0 &= \sqrt{g}P \, , \\
a_1 &= \sqrt{g}\frac{\vec{J}}{c_s} \, , \\
a_2 &= \frac{P}{2c_s^2}\left(g^{\alpha\beta}c^2 - c_s^2\delta^{\alpha\beta}\right) \, .
\end{aligned} \tag{4-58}$$

By replacing these coefficients into Eq. (3-39), we obtain

$$f_{i\neq0}^{eq} = w_i\sqrt{g}\left[P + \frac{\vec{\xi}_i \cdot \vec{J'}}{c_s^2} + \frac{P}{2c_s^4}\left(g^{\alpha\beta}c^2 - c_s^2\delta^{\alpha\beta}\right)\left(\xi_i^\alpha\xi_i^\beta - c_s^2\delta^{\alpha\beta}\right)\right] \, . \tag{4-59}$$

As usual, f_0^{eq} can be obtained from the relation

$$f_0^{eq} = \sqrt{g}P - \sum_{i=1} f_i^{eq}. \tag{4-60}$$

Finally, the equilibrium distribution function obtained from the Hermite expansion is

$$f_i^{eq} = \begin{cases} w_0\sqrt{g}P\left[\frac{1}{w_0} - \frac{c^2}{2c_s^2}g^{\alpha\alpha}\right] - \sqrt{g}P + \frac{5}{2}\sqrt{g}Pw_0 & \text{if } i = 0 \\ w_i\sqrt{g}\left[P + \frac{\vec{\xi}_i \cdot \vec{J}'}{c_s^2} + \frac{P}{2c_s^4}\left(g^{\alpha\beta}c^2 - c_s^2\delta^{\alpha\beta}\right)\left(\xi_i^\alpha \xi_i^\beta - c_s^2\delta^{\alpha\beta}\right)\right] & \text{if } i \neq 0 \end{cases}. \tag{4-61}$$

Note that it includes additional terms not present in the equilibrium function found by moment matching in the previous section (Eq. (4-50)). It worth to mention that Eq. (4-61) shows us an important fact: The coefficient $a_2 = \frac{P}{2c_s^2}\left(g^{\alpha\beta}c^2 - c_s^2\delta^{\alpha\beta}\right)$ is the difference between the real space propagation speed and the information propagation speed on the chosen lattice discretization. In order to maintain the stability of the model and to avoid negative distribution functions we should keep these two quantities of the same order of magnitude. Note also that the term $\frac{P}{2c_s^4}\left(g^{\alpha\beta}c^2 - c_s^2\delta^{\alpha\beta}\right)\left(\xi_i^\alpha \xi_i^\beta - c_s^2\delta^{\alpha\beta}\right)$ in the equilibrium distribution function contains the information about the coordinates and is the only that distinguish among different directions; therefore, it is the key to recover the real space isotropy. To determine if the model is isotropic or not, we simulated a circular wave in a rectangular domain, as we did in Sec. 4.4.1. The results are shown in Fig. 4-6

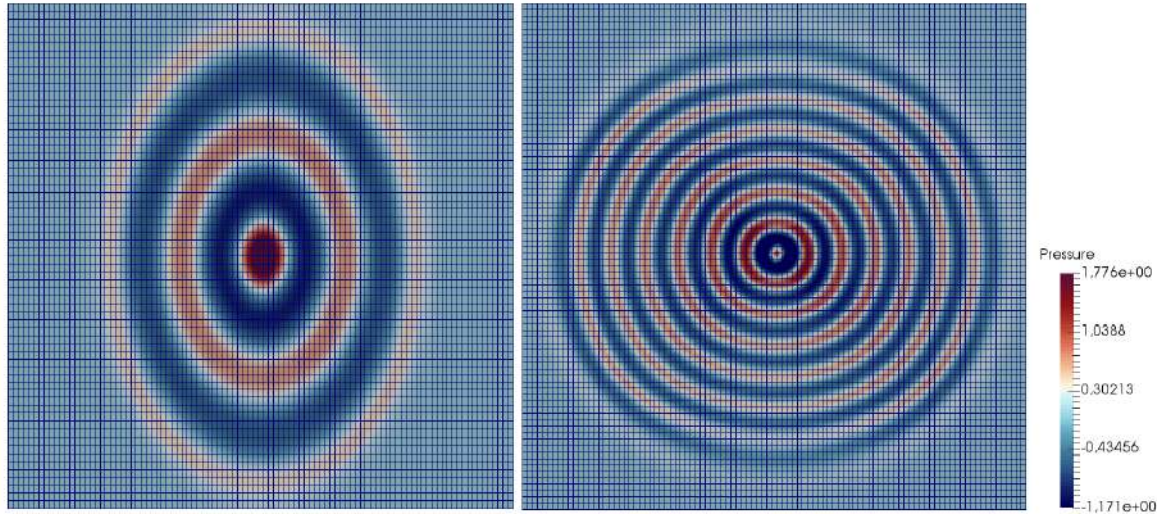**Figure 4-6**.: Test of isotropic propagation in a rectangular grid for LBM in general coordinates with f_i^{eq} found from the Hermite Polynomials procedure, for low wave velocity $c = 0.1$ (left) and higher wave velocity $c = 0.34$ (right)

Note that the the evolution of the wave is not isotropic. For low c values the information propagates faster than the wave ($c_s > c$) and, therefore, the wave travels faster in the

direction where the cells are larger. In other words, the action of the additional term in f_i^{eq} is not strong enough. In addition, by adjusting the value of c we can achieve a more isotropic propagation. For instance choosing $c = 0.34$ gives an almost isotropic propagations on the cells of aspect ratio $0.8 : 1$ we use in Fig. **4-6**.

Fig. **4-7** shows the pressure waves inside the open pipe with this new approach. The dimensions, the source and the boundary conditions are the same that the ones used in Sec. 4.4.1. The speed c has been adjusted to $c = 0.34$. In comparison with the previous result we see that that the amplitude of the wave decays while the wave propagates in space and that the nodal surfaces are not flat, as expected from the analytical solution, showing us that adjusting the velocity does not work properly.
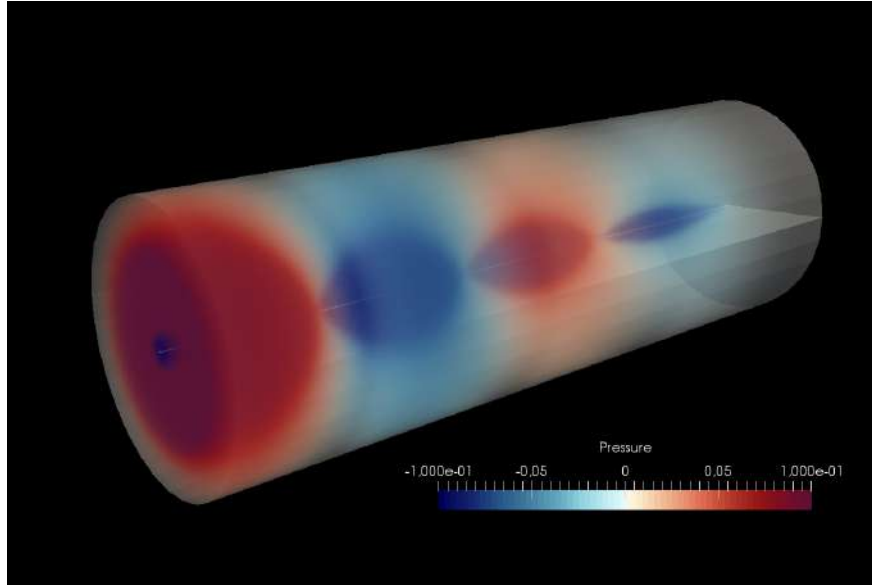

Figure 4-7.: Pressure waves inside a closed-open end pipe by using the f_i^{eq} found from the Hermite polynomials expansion after 8000 time steps. The open end is in the right.

Although the model is not isotropic, the additional terms in Eq. (4-61) make the model more stable and give us the possibility to perform simulations on more intricate geometries, even without axial symmetry. As an example we simulate a torus with $r_{min} = 5.12$, $r_{max} = 409.6$ and $R = 640$. The coordinate transformation to model this geometry is

$$x = (R + r\cos(\phi))\cos(\theta)$$
$$y = (R + r\cos(\phi)))\sin(\theta) \quad . \tag{4-62}$$
$$z = r\sin(\phi)$$

where the coordinates r, θ and ϕ and the constant R are described in the Appendix C. The simulation runs in a computational domain of 20 cells in the r direction, 200 cells in the θ

direction and 30 cells in ϕ. We set periodic boundary conditions in θ and ϕ, plus bounce-back conditions for the radial coordinate as defined in Eq. 4-55. The source is

$$P_{source}(r, \theta, \phi, t) = A \sin(\omega t) \, \delta(r - r_{min}) \, \delta(\theta) \tag{4-63}$$

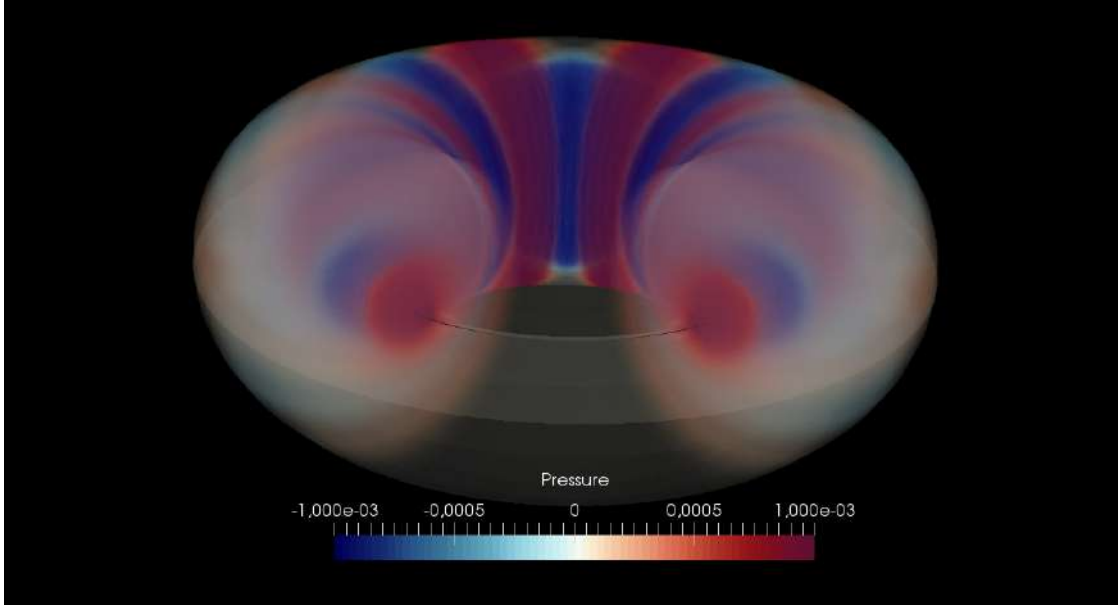Fig. **4-8** shows the evolution of the a wave generated inside the Torus,

Figure 4-8.: Pressure waves inside a torus by using the f_i^{eq} found from the Hermite polynomials expansion after 8400 time steps.

Summarizing, even though this second model allows to run simulations on geometries without axial symmetry, the solution of adjusting the wave velocity c is not satisfactory. Actually, the optimal value of c depends on the cell aspect ratio and, nothing guaranties that this adjustment will work if the aspect ratio changes from place to place. Nevertheless, constructing the equilibrium distribution function with Hermite polynomials shows that there is a problem with the term $\frac{P}{2c_s^4} \left(g^{\alpha\beta} c^2 - c_s^2 \delta^{\alpha\beta} \right) \left(\xi_i^\alpha \xi_i^\beta - c_s^2 \delta^{\alpha\beta} \right)$ of the equilibrium distribution function (Eq.(4-61)) and give us a target to solve. The improvement of the model and the recovering of the isotropy is explained in Chapter 5.

5. LBM for Acoustics in General Coordinates: General Isotropic Model.

5.1. The final proposal

To improve the approach presented in Sec. 4.4, it is important to prove that, in fact, such distribution fulfils the relations given in Eqs. (4-11)-(4-13) for this particular discretization scheme via the Eqs. (3-1). To this aim we compute

$$
\sum_i f_i^{eq} = f_0^{eq} + \sum_{i=1} w_i \sqrt{g} \left[P + \frac{\vec{\xi_i} \cdot \vec{J'}}{c_s^2} + \frac{P}{2c_s^4} \left(g^{\alpha\beta} c^2 - c_s^2 \delta^{\alpha\beta} \right) \left(\xi_i^{\alpha} \xi_i^{\beta} - c_s^2 \delta^{\alpha\beta} \right) \right]
$$
$$
= \sqrt{g} P \tag{5-1}
$$

which give us the desired result, but if we consider the third momentum,

$$
\sum_i f_i^{eq} \xi_i^{\gamma} \xi_i^{\delta} = \sum_i w_i \sqrt{g} \left[P \xi_i^{\gamma} \xi_i^{\delta} + \frac{\xi_i^{\alpha} J'^{\alpha} \xi_i^{\gamma} \xi_i^{\delta}}{c_s^2} + \frac{P}{2c_s^4} \left(g^{\alpha\beta} c^2 - c_s^2 \delta^{\alpha\beta} \right) \left(\xi_i^{\alpha} \xi_i^{\beta} \xi_i^{\gamma} \xi_i^{\delta} - c_s^2 \xi_i^{\gamma} \xi_i^{\delta} \delta^{\alpha\beta} \right) \right]
$$
$$
= \sqrt{g} P \sum_i w_i \xi_i^{\gamma} \xi_i^{\delta} + \frac{\sqrt{g} P}{2c_s^4} \left(g^{\alpha\beta} c^2 - c_s^2 \delta^{\alpha\beta} \right) \left(\sum_i w_i \xi_i^{\alpha} \xi_i^{\beta} \xi_i^{\gamma} \xi_i^{\delta} - c_s^2 \delta^{\alpha\beta} \sum_i w_i \xi_i^{\gamma} \xi_i^{\delta} \right) ,
$$
$$
\tag{5-2}
$$

we can use the relations (3-1) for the second and fourth order in $\vec{\xi_i}$ to find.

$$
\sum_i f_i^{eq} \xi_i^{\gamma} \xi_i^{\delta} = \sqrt{g} P c_s^2 \delta^{\gamma\delta}
$$
$$
+ \frac{\sqrt{g} P}{2c_s^4} \left(g^{\alpha\beta} c^2 - c_s^2 \delta^{\alpha\beta} \right) \left(c_s^4 \left(\delta^{\alpha\beta} \delta^{\gamma\delta} + \delta^{\alpha\gamma} \delta^{\beta\delta} + \delta^{\alpha\delta} \delta^{\beta\gamma} \right) - c_s^2 \delta^{\alpha\beta} c_s^2 \delta^{\gamma\delta} \right)
$$
$$
= \sqrt{g} P c_s^2 \delta^{\gamma\delta} + \frac{\sqrt{g} P}{2} \left(g^{\alpha\beta} c^2 - c_s^2 \delta^{\alpha\beta} \right) \left(\delta^{\alpha\gamma} \delta^{\beta\delta} + \delta^{\alpha\delta} \delta^{\beta\gamma} \right) \tag{5-3}
$$
$$
= \frac{\sqrt{g} P}{2} c^2 \left(g^{\gamma\delta} + g^{\delta\gamma} \right) = \sqrt{g} c^2 P g^{\gamma\delta} = \sqrt{g} \left(\Pi^{(0)} \right)^{\gamma\delta} ,
$$

Note that, to correctly retrieve the definition of the stress tensor by means of the equilibrium distribution function, it is necessary to assure that the discrete velocities set fulfils the isotropy relations (Eqs. (3-1)) up to fourth order. However, it is possible to show that the

used D3Q7 in the Cartesian model only satisfies these relations up to third order, for this reason, implementing the lattice-Boltzmann model in general curvilinear coordinates for the wave equation requires using a higher order velocities set, for example D3Q15 or D3Q19.

However, the lattice-Boltzmann scheme for the wave equation has shown being more stable for the D3Q7 scheme than for higher order schemes, therefore, to achieve the isotropy maintaining the discrete velocities set, we introduce the corrective forcing term

$$\mathcal{F}^{\alpha} = \partial_{\beta} \left[\left(\sqrt{g} \right) \left(c_s^2 \delta^{\alpha\beta} - c^2 g^{\alpha\beta} \right) \right] , \tag{5-4}$$

which is the needed to correct the dynamics when we write the equilibrium distribution function as

$$f_i^{eq} = \begin{cases} w_0 \sqrt{g} P & \text{if } i = 0 \\ w_i \sqrt{g} \left[P + \frac{\vec{\xi}_i \cdot \vec{J'}}{c_s^2} \right] & \text{if } i \neq 0 \end{cases} . \tag{5-5}$$

The derivatives in Eq. (5-4) can be obtained from the lattice-Boltzmann scheme itself as explained in the Appendix A, they have de form:

$$\partial_{\beta} \left[\left(\sqrt{g} \right) \left(c_s^2 \delta^{\alpha\beta} - c^2 g^{\alpha\beta} \right) \right] = \frac{1}{c_s^2} \sum_i w_i \xi_i^{\beta} \left[\left(\sqrt{g} \right) \left(c_s^2 \delta^{\alpha\beta} - c^2 g^{\alpha\beta} \right) \right] \Big|_{\left(x^{\beta} + \xi_i^{\beta} \right)} + \mathcal{O} \left(\delta x^2 \right) , \tag{5-6}$$

the second moment of the equilibrium distribution function is, therefore,

$$\sqrt{g} J'^{\alpha} = \sum_i f_i^{eq} \xi_i^{\alpha} - \frac{\delta_t}{2} c^2 P \Gamma_{\beta\gamma}^{\alpha} g^{\beta\gamma} \sqrt{g} + \frac{\delta_t}{2} \partial_{\beta} \left[\left(\sqrt{g} \right) \left(c_s^2 \delta^{\alpha\beta} - c^2 g^{\alpha\beta} \right) \right] , \tag{5-7}$$

With this modification we perform again our isotropy test, the result is shown in Fig. 5-1.
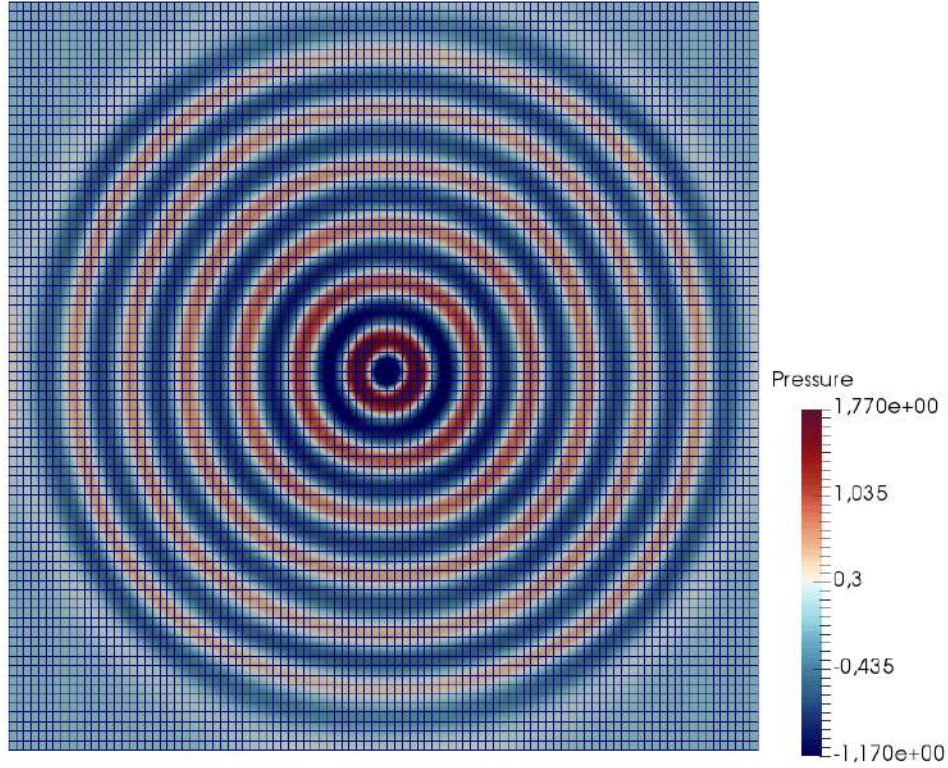
Figure 5-1.: Test of isotropic propagation in a rectangular grid for LBM in general coordinates with f_i^{eq} found from the improved Hermite Polynomials procedure

As expected, the isostropy of the model was recovered without the need of changing the stable discretization scheme D3Q7. Implementations of this model for higher order discretization schemes maintaining the stability is proposed as future work.

That closes the definition of our lattice-Boltzmann method for the simulation of acoustic waves in curvilinear coordinates. The information about the curvature of the system is included in the equilibrium distribution function and the macroscopic quantities, but the velocity set $\{\vec{\xi_i}\}$ remains the same. So, it is possible to adapt the geometry just by changing the metric tensor and Christoffel symbols, without altering the discretization scheme in the computer. This modified version will be used hereafter in our simulations. In this chapter we implement this model and describe the simulations in detail.

5.2.   Simulations

As examples, let us consider three cases cylinders, trumpets and torus. All the geometric properties of the coordinate systems needed in this model are consigned in the Appendix C.

5.2.1.   Polar Wave

To validate the method, let us start by simulating a radial cylindrical wave expanding from the z axis, whose theoretical solution is given by

$$P(r, \theta, z) = A\mathcal{J}_0(kr) \approx \frac{A}{\sqrt{r}} \cos(r \pm ct) \quad , \tag{5-8}$$

Where $\mathcal{J}_0$ is the zero-th order Bessel function. The simulation is done by imposing the macroscopic quantity P at the axis as a harmonic perturbation,

$$P_{source}(r, \theta, z, t) = C \sin(\omega t)\, \delta(r - r_{\min}) \quad , \tag{5-9}$$

where δ is the Dirac's delta, $\omega = 0.1256$ radians per timestep, $c = 0.5$ cells per timestep and $r_{min} = 1$ is the minimum value of r that can be simulated (since cylindrical coordinates have an indetermination at $r = 0$). For this simulation we use a cubic storage array of $200 \times 4 \times 4$ cells for the coordinates r, θ and z, respectively, with periodic boundary conditions in θ and z, plus free boundary conditions in $r = r_{max}$. Since our field does not depend on θ and z the simulation could be one-dimensional in r with a mesh $L_r \times 1 \times 1$; nevertheless, to validate a more general three-dimensional model that could be useful for future simulations, we simulated some few cells in the θ and z directions. The results for this benchmark (Fig. 5-2) are in excellent agreement with the theoretical expression Eq. (5-8). In contrast with previous schemes in the literature [7, 35, 36], no additional interpolation steps in the evolution are required. All the values of the quantities shown here and henceforth are in lattice units.
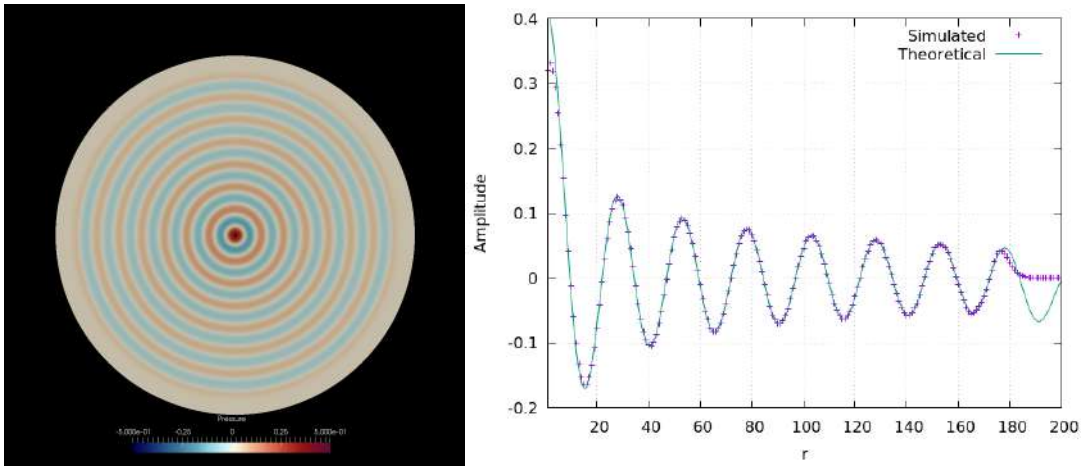

Figure 5-2.: Simulation of a cylindrical wave in cylindrical coordinates. Pressure profile at a cross section of the cylinder after $t = 365$ steps (Left). Pressure amplitude as a function of the radial coordinate r from the same simulation compared with the theoretical expression Eq.(5-8)(Right).

5.2.2.   Waves inside a open-closed end pipe

Now, let us simulate an acoustic wave inside an open-closed end pipe. The appropriate coordinate systems for this problem is the cylindrical one, given by the transformation

$$
\begin{aligned}
x &= r\cos\theta \\
y &= r\sin\theta \quad . \\
z &= z
\end{aligned}
\tag{5-10}
$$

Fig. **5-3** describes the boundary conditions imposed. Free conditions are imposed at the end of the pipe at $z = z_{max}$. In addition, because the axis $r = 0$ is now part of the simulation space (in contrast to the previous case, where the axis was a source boundary condition), we take care of the coordinates' singularity at $r = 0$ by imposing free boundary conditions at $r = r_{min} = 2$, too. Such free conditions are implemented as usual by copying the values of the neighbouring cell normal to the surface. Bounce-back boundary conditions are considered in the pipe walls at $r = r_{max}$ and in the closed end at $z = 0$. These boundary conditions can be described as follows: In the advection step each cell on the boundary would miss the incoming information from outside the simulation domain. Bounce-back boundary conditions copy to the unknown incoming distribution functions the values of the outgoing ones, reflected in the same direction, that is

$$
f_{i_{in}}\left(\vec{x}_{\text{wall}}, \vec{\xi}_{\text{in}}, t\right) = D\, f_{i_{out}}\left(\vec{x}_{\text{wall}}, \vec{\xi}_{\text{out}}, t\right) \quad ,
\tag{5-11}
$$

where the indexes *in* and *out* mean the incident and reflected directions, respectively. Here, some dissipation has been added by inserting a damping factor $D = 0.65$, which helps to reach steady-stable oscillations when the system is excited by an incoming oscillation of constant amplitude at the closed end. The resonant frequencies are identified by measuring the steady-state amplitude at the point $\left(\frac{r_{max}}{10}, 0, 0\right)$
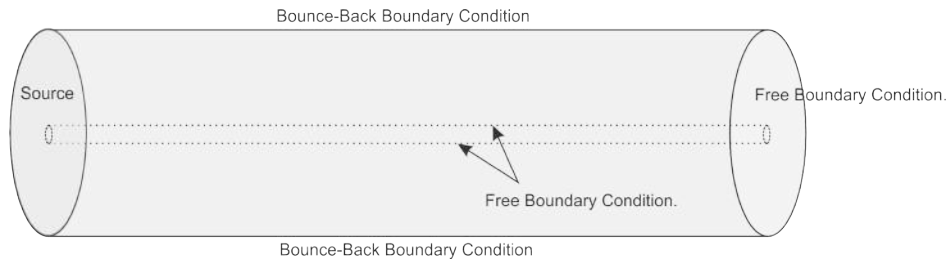

Figure 5-3.: Boundary conditions for the simulation of a wave inside a pipe

As a first functional form for the pressure source, let us consider that the left end oscillates as a whole like a flat rigid body, $P_{source}(r, \theta, z, t) = C\sin(\omega t)\,\delta(z)$. This wave propagates along the z direction only, as in a one-dimensional cord; thus, we would expect that the resonant

frequencies correspond to those of the chord with one end free and one end fixed,

$$\omega_n = \frac{2\pi c(2n+1)}{4L_z} \quad .$$

(5-12)

However, the results (the blue dashed line in Fig.5-5) shows that it only works well for the first normal modes; thereafter, the radial dimensions affect too much and the approximation is no longer valid.

As a more general perturbation that allows the radial modes to be exited, let us consider that the left end at $z = 0$ is a fixed wall plus an oscillating ring in front of it at $z = 1$. The radius of the ring is chosen to be $r_{min} = 2$, such that the ring fits just around the cylinder at $r = 0$ that was excluded from the simulation space. The functional form of this source is $P_{\text{source}}(r, \theta, z, t) = C \sin(\omega t)\delta(r - r_{min})\delta z$. Fig. 5-4 shows the pressure waves inside the pipe at the steady-state condition ($t = 8000$ steps) for a given wavelength ($\lambda = 4z_{max}/9$) with the ring source at its left end. The computational domain for this simulation was 20 cells in r from $r_{min} = 2$ to $r_{max} = 200$, 100 cells in z from $z_{min} = 0$ to $z_{max} = 1200$ and 4 cells in θ with periodic boundary conditions.
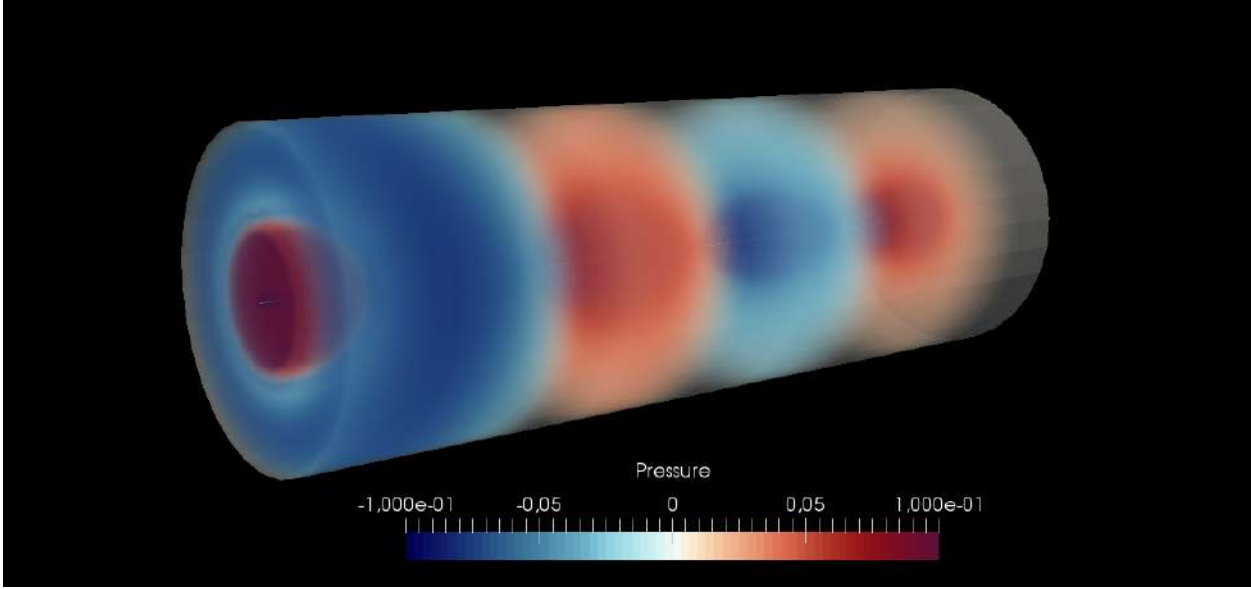

Figure 5-4.: Pressure profile inside a pipe after $t = 8000$ time steps, $\lambda = 4zmax/9$.

The expected normal modes are now three-dimensional with axial symmetry. The pipe imposes a von Newmann boundary condition at the cylindrical wall,

$$\left(\frac{\partial}{\partial r} + \frac{1}{r}\right) P(r_{max}, \theta, z) = 0 \quad .$$

(5-13)

It is possible to show (see Appendix B) that this condition, together with the previous one

at the pipe ends, leads to the following characteristic frequencies:

$$\omega_{j,0,n} = c \left[\zeta_l^2 + \left(\frac{(2n+1)\pi}{4L_z} \right)^2 \right]^{1/2} \quad , \tag{5-14}$$

where ζ_l are the zeros of

$$f(\zeta r_{max}) = J_0(\zeta r_{max}) - \zeta R J_1(\zeta r_{max}) . \tag{5-15}$$

and correspond to the radial normal modes. The first three values of ζ_l are shown in Table
5-1

Order	Value
1	1,2556
2	4,0793
3	7,1390

Table 5-1.: First three zeros of the Eq. 5-15

Fig. **5-5** shows measured intensity (the amplitude squared) at the sensing point as a function
of the frequency. The solid vertical lines are the expected values of the resonant frequencies
obtained from Eq.(5-14). Note that in the case of the oscillating ring longitudinal modes
are more defined but shifted due to the appearance of the first radial mode at $\omega = 0.164$.
In addition, we observe that this way of perturbation reduces the resonant amplitude of
some longitudinal modes. The resonant frequencies simulated with the oscillating ring as
source are in great agreement with the expected values, with an mean deviation between the
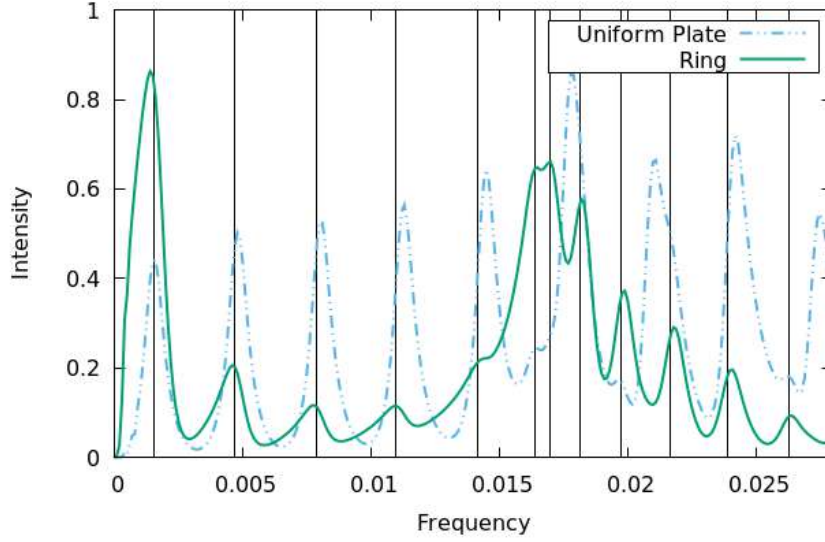maxima and the black vertical lines below 1 %.

Figure 5-5.: Frequency spectrum inside a pipe for waves generated by an uniform plate and
an oscillating ring compared with the theoretical expectations (Solid vertical
lines).

5.2.3.   Waves inside a Trumpet

The coordinate system implemented for the cylinder simulations can be modified to include
a flared end resembling a trumpet's bell. In this work, we consider a particular shape named
Bessel Horn, given by the following coordinate system:

$$
\begin{aligned}
x &= r\cos(\theta)\mathcal{Z}^{-\lambda}\\
y &= r\sin(\theta)\mathcal{Z}^{-\lambda} \quad ,\\
z &= z
\end{aligned}
\tag{5-16}
$$

with λ a positive real number and $\mathcal{Z} = z_{max} - z$, where z_{max} is the longitude of the pipe.
The surfaces for $r = $ const resembles the shape of a different horn for each value of λ (Fig.
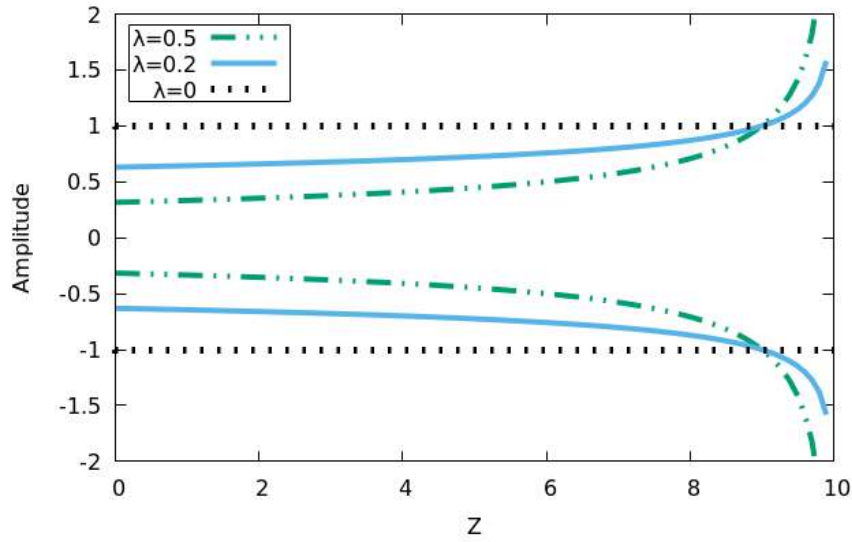**5-6**).Note that we can retrieve the cylindrical case just by making $\lambda = 0$.

Figure 5-6.: Shape of the trumpet for different values of λ.

By using the equations (5-16), and with the geometric properties of that transformation Eqs. (C-20) and (C-17) (Appendix C), it is possible to simulate the acoustical waves inside a trumpet with the present lattice-Boltzmann method for general coordinates as a two-dimensional problem. The simulation space and boundary conditions are very similar to the ones for the pipe with an oscillating ring (Sec. 5.2.2 and Fig. 5-3). Fig. 5-7 shows a snapshot of the pressure profile for an axisymmetric Bessel horn with $\lambda = 0.2$ with $r_{min} = 2$, $r_{max} = 150$ and $z_{max} = 750$ after 8400 timesteps. As expected, the pressure wave intensity is reduced at the end of the trumpet due to the bell.
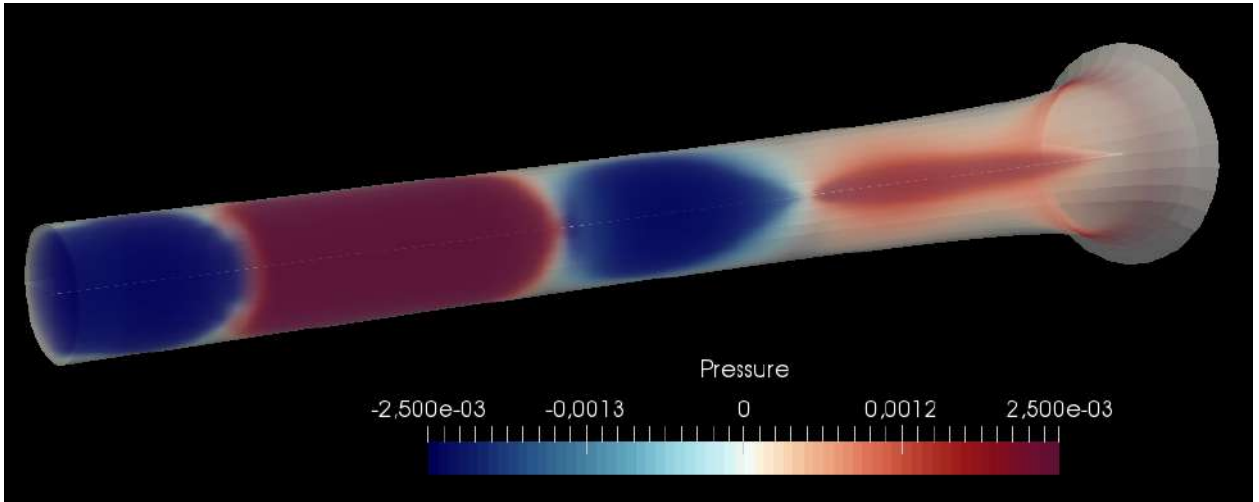

Figure 5-7.: Pressure profile inside a trumpet at $t = 8400$ time steps and $\lambda = 4z_{max}/9$.

Fig. 5-8 compares the pressure oscillation envelope along the z axis at a fixed value of r (3

cells) when the ring oscillates at a given frequency $\omega = 0.005$. Results are shown for two values of λ: $\lambda = 0.1$, which corresponds to a trumpet, and $\lambda = 0$ which models a pipe. Note that the oscillation amplitude in the trumpet decreases near the bell, as has been reported in experiments [42].
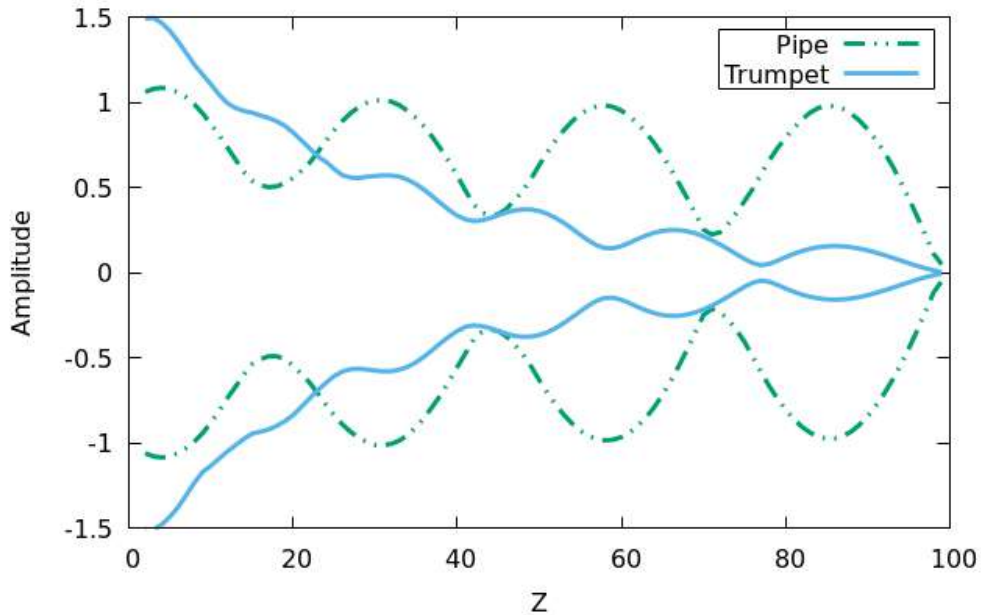
Figure 5-8.: Envelope of oscillation for the pipe ($\lambda = 0$) and the trumpet ($\lambda = 0.1$)

Let us now study how the natural frequencies change by the inclusion of the bell. Fig. 5-9 shows the resonant peaks for a trumpet with $\lambda = 0.1$ compared with the previously obtained results for $\lambda = 0$. As expected, for the case of the trumpet the longitudinal normal modes are less defined. Furthermore, the second radial modes are strongly suppressed by the bell, something similar to what is observed in real pipes [42].
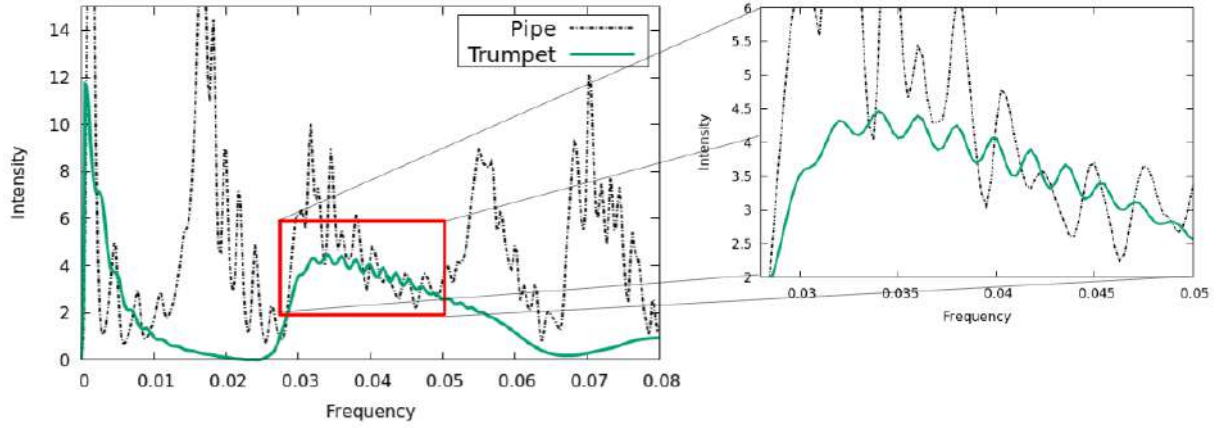
Figure 5-9.: Comparison between the vibrational modes of a pipe and a trumpet with $\lambda = 0.1$ and zoom over the red square.

Finally we measured the model convergence. To this aim, we chose a theoretically known quantity (namely, the third characteristic frequency of a closed-open end pipe) and we compare it with its simulated value. As the resolution increases, we expect that the smaller the cell size, the smaller the difference between the theoretical value and the simulated one. Such behaviour is shown in Fig. **5-10**. The figure shows a power-law dependence of the error with the cell size, with exponent 2.1052 ± 0.08006; so, the model has second order accuracy. This is the same accuracy order of the standard lattice-Boltzmann scheme.

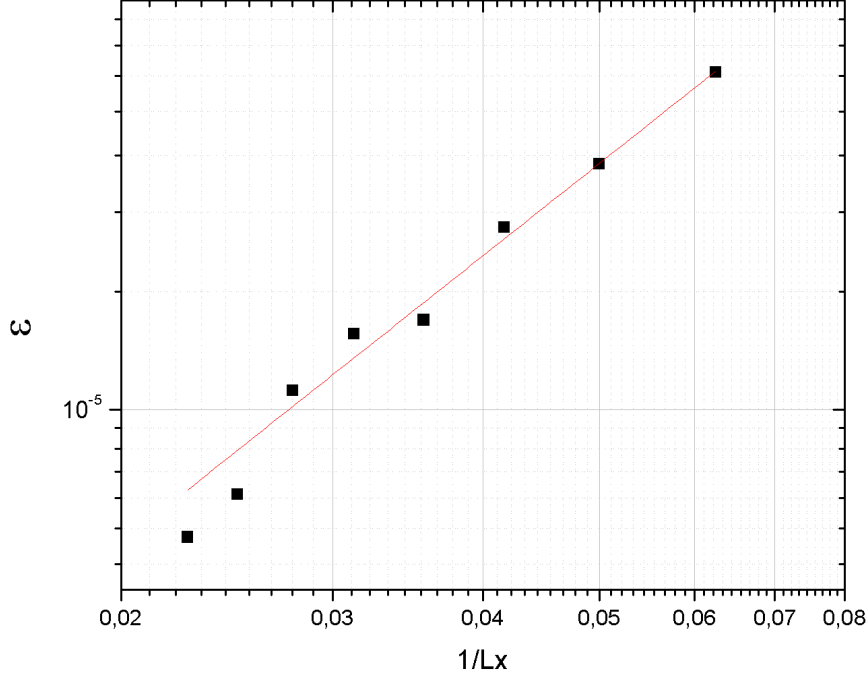**Figure 5-10**.: Simulation error for the third characteristic frequency of an closed-open end pipe ($\omega_{theo} = 0.00608$ for $n = 3$, $z_{max} = 345.6$ and $c = 0.5$, see Eq.5-14) as a function of the cell size. The red line is a power fit $\epsilon = A\left(1/L_x\right)^B$ with $A = 0.019 \pm 0.005$ and $B = 2.105 \pm 0.080$.

5.2.4. Waves inside a torus

As a third benchmark, we study the pressure waves inside a torus. A torus can be seen as a circle of radius r_{max} whose center travels along a larger circle of radius R (See Appendix C). It can be described by the coordinate transformation

$$
\begin{aligned}
x &= (R + r\cos(\phi))\cos(\theta) \\
y &= (R + r\cos(\phi))\sin(\theta) \quad . \\
z &= r\sin(\phi)
\end{aligned}
\tag{5-17}
$$

The chosen torus has $R = 640$, $5.12 < r < 409.6$, $0 < \theta < 2\pi$ and $0 < \phi < 2\pi$. For the simulations we used 20 cells in r, 200 cells in θ and 30 cells in ϕ. The boundary conditions imposed are bounce-back in r_{max}, free in r_{min} and periodic both in θ and ϕ.
The pressure source is located in three ways. The first source is a ring along the major circle of radius R, and its functional form is $P_{source}(r, \theta, \phi, t) = A\sin(\omega t)\delta(r - r_{min})$. Fig.

5-11 shows the evolution of the pressure wave for two values of ω. It can be seen that the generated wavefronts have the expected radial symmetry.
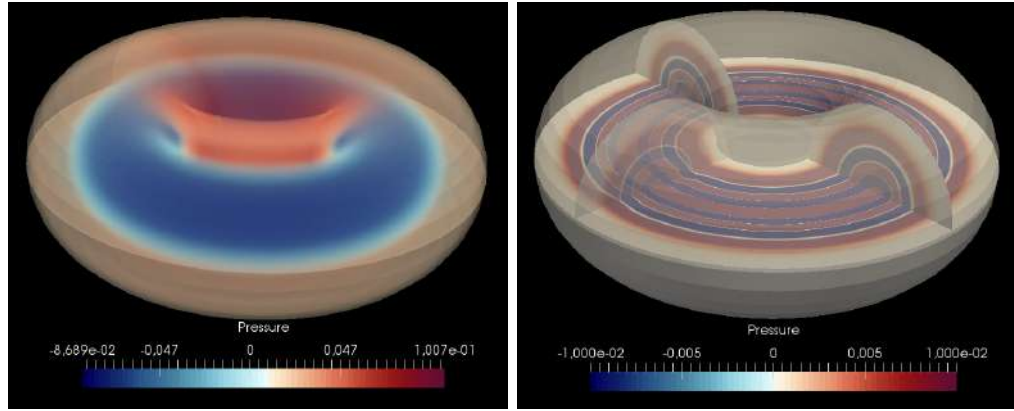
Figure 5-11.: Pressure waves inside a torus. The waves were generated from the inner torus with $r = r_{min}$ and for all the values of θ and ϕ.

The second source is similar to the small ring employed in pipes and trumpets, with functional form $P_{source}(r, \theta, \phi, t) = A \sin(\omega t)\delta(r - r_{min})\delta(\theta)$. This source allows the excitation of normal modes in both r and θ directions. The results for different frequencies are shown in Fig. **5-12**.
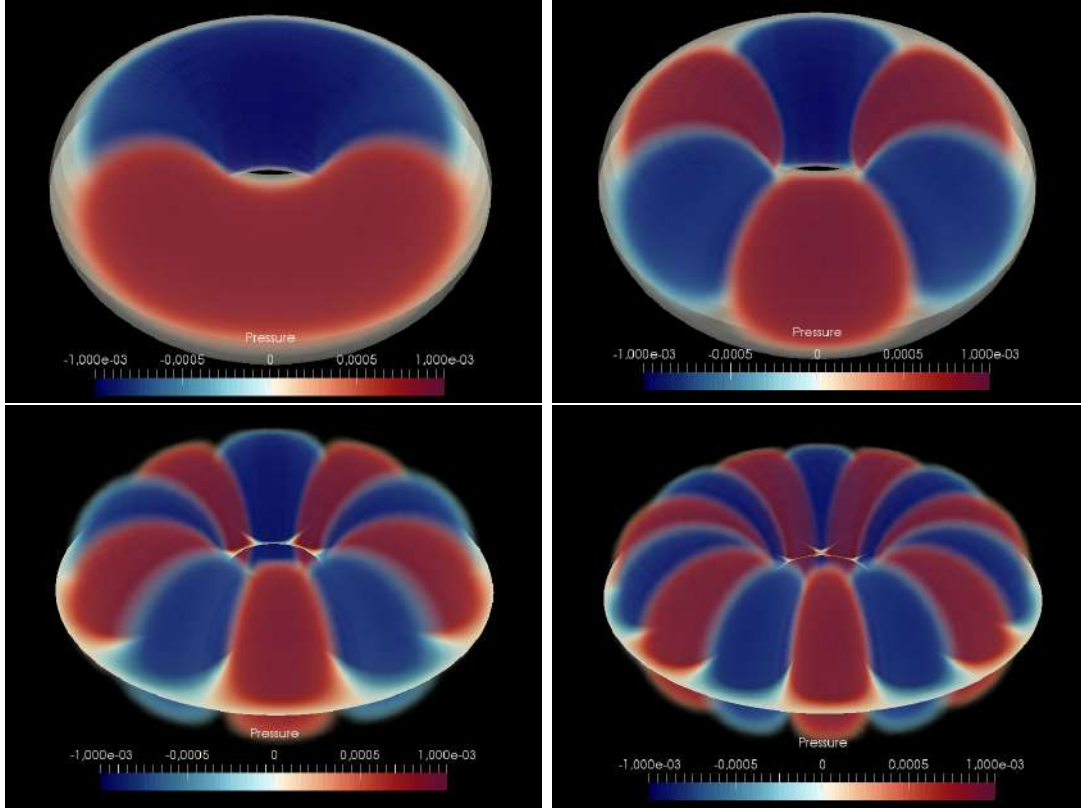
Figure 5-12.: Pressure waves inside a torus. The waves were generated from a ring with $r = r_{min}$ and $\theta = 0$ for all the values of ϕ, the wavelengths λ are $2\pi R/n$ where $n = 2, 4, 9, 19$ (left to right and top to bottom). The frequency $\omega = 2\pi c/\lambda$

Next, we study the resonant frequencies for this geometry. To this aim we locate the small oscillating ring at $\theta = 0$ and measure the pressure intensity at the opposite point on the major circle (i. e. at $\theta = \pi$) after 8000 time steps, when the wave has reached a steady-stable condition. Then, we vary the frequency within the range $(0, 0.5)$. The results are shown in Fig. **5-13**.
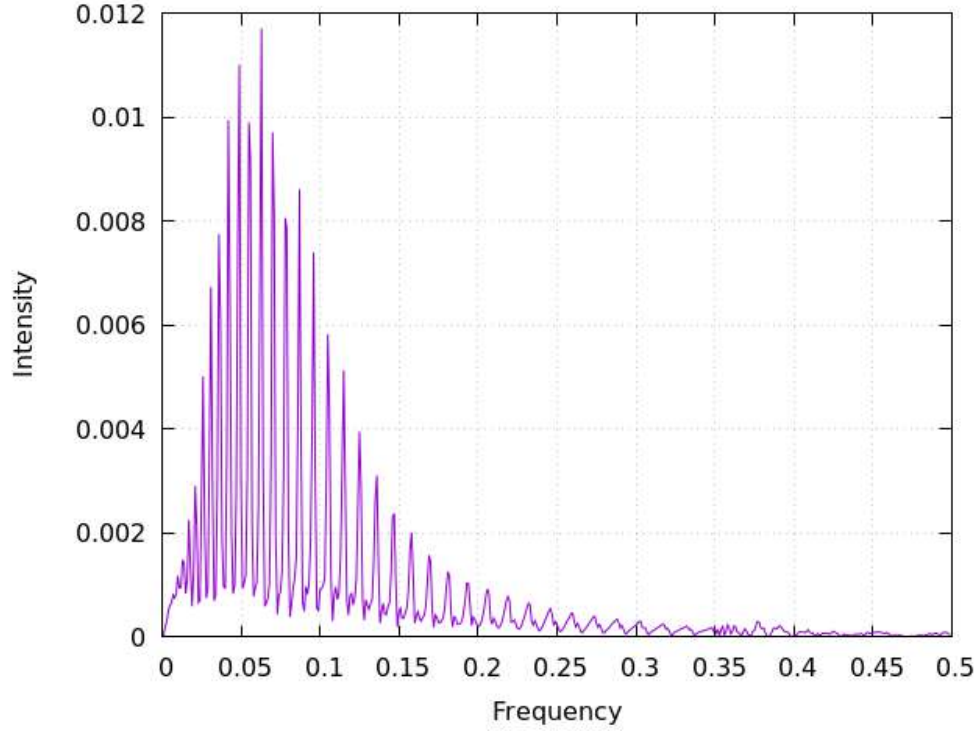
Figure 5-13.: Wave intensity at $(r_{max}, \pi, 0)$ after 8000 timesteps for $0 < \omega < 0.5$

Note that the larger resonant peaks are placed whitin 0.05 and 0.1 radians per click. There is also a cutoff frequency near to 0.25 radians per click. Although the analytical solution for the normal modes of the torus was not found in the literature, it is interesting to point out that the pattern is very similar to the one for a trumpet with an open bell (Fig. **5-14**) shows impedance measurements of a real trumpet, reported by Rossing [42].

FIG. 11.6
Impedance curve for a 140-cm length
of trumpet tubing with a trumpet bell
attached. Compare this with Fig. 11.4
(From *Fundamentals of Musical
Acoustics* by Arthur H. Benade.
Copyright © 1976 by Virginia
Benade. Reprinted by permission.)
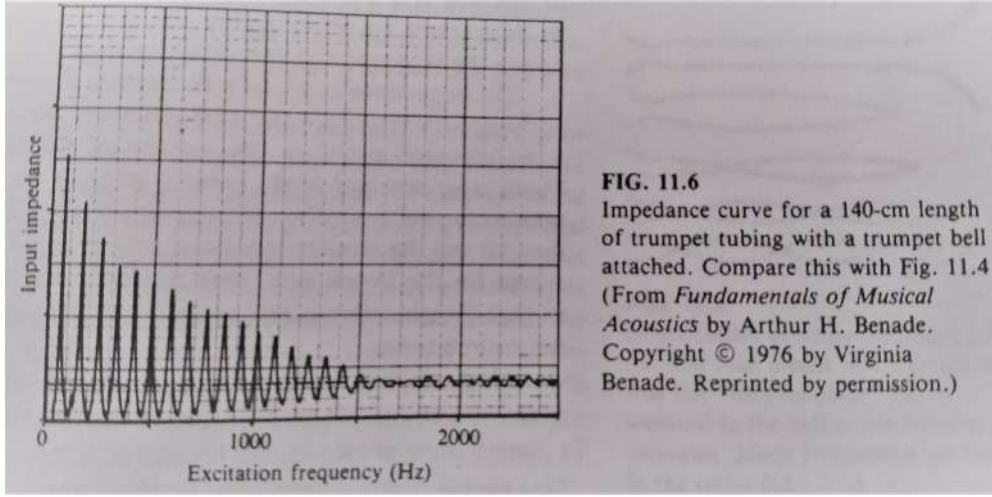
Figure 5-14.: Experimental impedance measurements of reported in [42] for a large trumpet.

Finally, in order to simulate more general perturbations, the third source we used is an oscillating point outside any symmetry axis, i.e. at $r = \frac{r_{max} - r_{min}}{2}$, $\theta = 0$, and $\phi = \pi/2$. The functional form of the source is, therefore, $P_{source}(r, \theta, \phi) = A \sin(\omega t)\delta\left(r - \frac{r_{max} - r_{min}}{2}\right)\delta(\theta)\delta(\phi - \pi/2)$. The resulting pattern is shown in Fig. 5-15. We can observe that the pattern is no longer symmetric in ϕ it shows variations along r.

Figure 5-15.: Pressure waves inside a torus generated from a general source.

For this last case, the evolution inside the torus is general, since it is not restricted to any type of symmetry; Therefore, this model can be applied to more complicated systems, like the Cochlea. Its study is the subject of Chapter 6.

6. Acoustic waves inside the Cochlea.

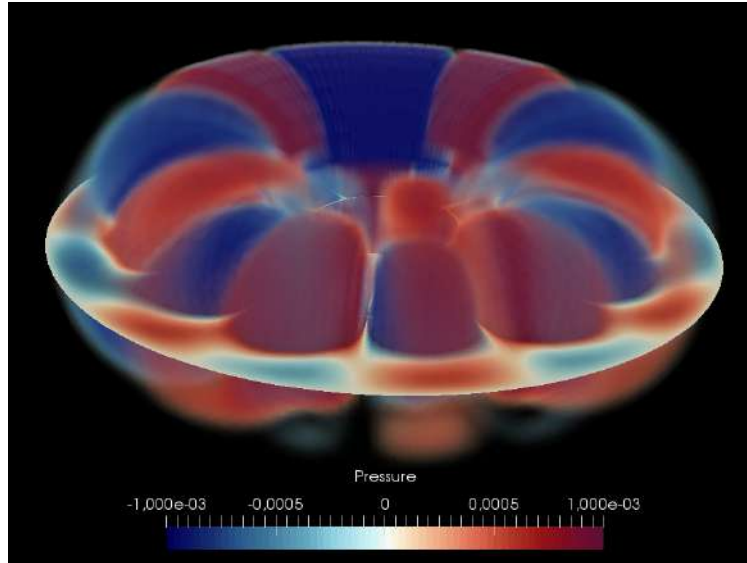Once the LBM for acoustics in general coordinates has been constructed an tested, we are able to use it in a very complicated geometry: the Cochlea. Based on its anatomy and physiology (Chapter 2), we propose a coordinate transformation that allow us to model a very realistic and detailed Cochlea and set the boundary conditions to simulate the acoustic processes inside. In fact, we are more interested in the pressure waves than in the fluid dynamics inside the coiled tube. In this work we will measure the pressure difference on the surface the basilar membrane located. However, the way the geometric model is build allows to study also the Reissner's membrane effortlessly, the study of the Reissner's membrane is left for future works.

This Chapter starts by describing how we model such complex system, both geometrically and physically (Sec. 6.1). Afterwards we study the acoustic response of the cochlea by using the new LBM and the results and important remarks are summarized Sec. 6.2.

6.1. Modelling the Cochlea

6.1.1. Geometry

As shown in Sec. 2.1 we can model the cross section of the Cochlea as a cardioid. The parametric equations in two dimensions are

$$x := r \cos(\phi) \left(1 + \cos(\phi)\right) , \tag{6-1}$$
$$z := r \sin(\phi) \left(1 + \cos(\phi)\right) , \tag{6-2}$$

Thus, if we replace the generator circle of the Torus in Subsection 5.2.4 by these equations we obtain a Torus with a cardioid as cross section,

$$x := \cos\left(\theta\right) \left(R + r \cos\left(\phi\right) \left(1 + \cos\left(\phi\right)\right)\right) \tag{6-3}$$
$$y := \sin\left(\theta\right) \left(R + r \cos\left(\phi\right) \left(1 + \cos\left(\phi\right)\right)\right) \tag{6-4}$$
$$z := r \sin\left(\phi\right) \left(1 + \cos\left(\phi\right)\right) . \tag{6-5}$$

We need the tube to whirl 2.5 turns, i. e. $0 < \theta < 5\pi$, and the Torus's radius should decrease with the advance of θ it is to deform the major circle of the Torus into a spiral. In this work, we propose a linear decrement $R \to R - a\theta$, where a can be adjusted for realism. As a third modification, we elongate the spiral in the vertical direction (z). This avoids the cochlea to

turn into itself. Again we propose this increment on the coiling axis as linear, $z \rightarrow z + A\theta$. Finally, as the coclea is a tampered tube, we reduce the cross section by multiplying the cardioid by a function of θ. For our purposes that factor is $\cos\left(\frac{\theta}{F}\right)$ and F can be varied to correctly model the tamppering.

Summarizing, the coordinate transformation which better models the cochlea is

$$x := \cos(\theta)\left(R - a\theta + r\cos(\phi)(1 + \cos(\phi))\cos\left(\frac{\theta}{F}\right)\right) \tag{6-6}$$

$$y := \sin(\theta)\left(R - a\theta + r\cos(\phi)(1 + \cos(\phi))\cos\left(\frac{\theta}{F}\right)\right) \tag{6-7}$$

$$z := r\sin(\phi)(1 + \cos(\phi))\cos\left(\frac{\theta}{F}\right) + A\theta, \tag{6-8}$$

where the variables $0.09\text{mm} < r < 0.9\text{mm}, 0 < \theta < 5\pi,$ and $-\pi < \phi < \pi$ are described in Fig. 6-1. The geometry defined in this way allows us to control the tampering of the cochlear cavity and the reduction of the spiral radius just fitting the values of F and a, respectively, and the parameter A controls the vertical elongation of the spiral.
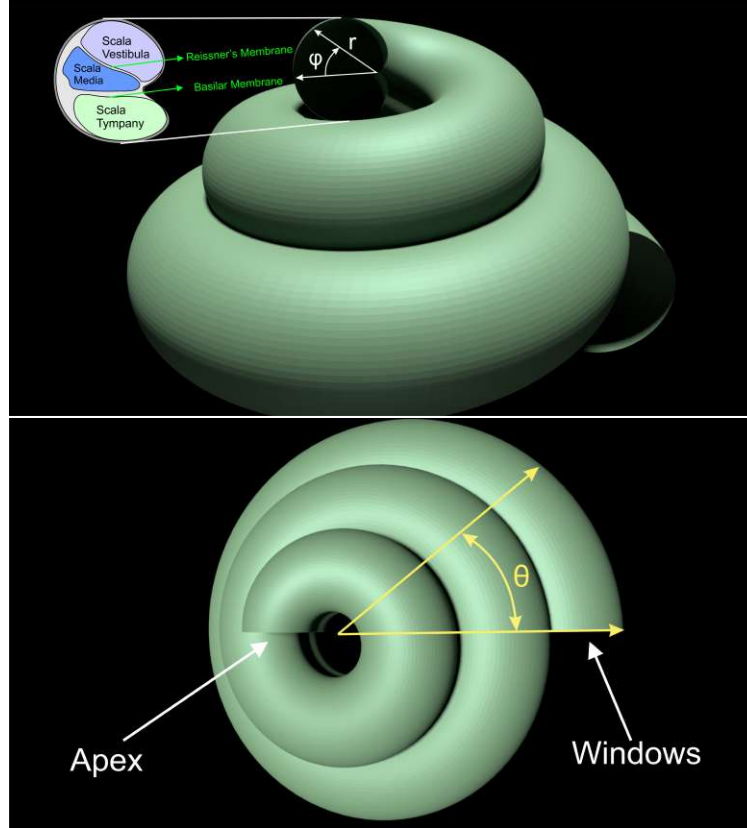

Figure 6-1.: Cochlea's Geometry generated from Eq. (6-6). Side view (top), upper view (bottom)

The parameters was tuned to obtain a very realistic cochlea. Its values are:

$$
\begin{aligned}
A &= 0.2366 \, \text{mm} \,, \\
a &= 0.1648 \, \text{mm} \,, \\
R &= 2.8125 \, \text{mm} \,, \\
F &= 18.67 \,.
\end{aligned}
$$

(6-9)

With this choice of parameters the dimensions of the cochlea are the desired ones (Fig. **6-2**).
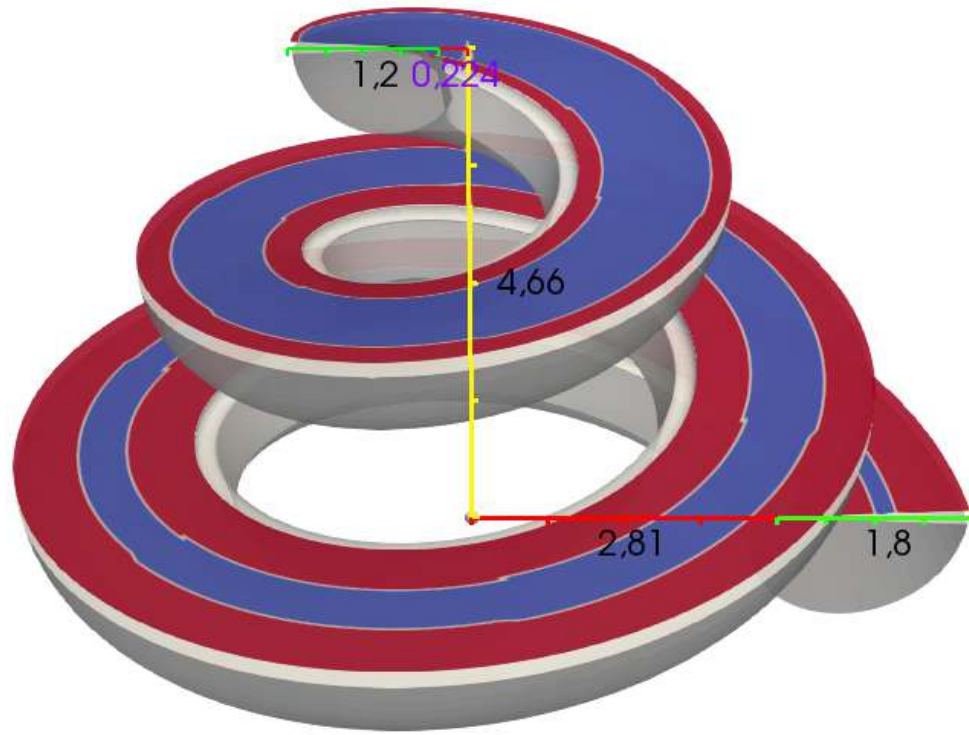
Figure 6-2.: Longitudinal section of the cochlea ($\phi < 0$) (gray volume) that evidences the position of the Bassilar Membrane (blue strip) embed in the surface $\phi = 0$ (red). The dimensions are in milimeters [mm]

An important advantage of using this parametrization of the geometry is that the plane on which the Bassilar membrane lies is just a surface of constant ϕ, actually $\phi = 0$. Furthermore, it also would allow us to model the Reissner membrane in the future, just by setting $\phi = k > 0$ at the right place in the Cochlea.

6.1.2. Physics

The next step, after correctly defining the geometry, is to model the physical parameters and boundary conditions to represent the process as realistic as possible.

First, let us recall that in this work we do not simulate the fluid mechanics inside the tubular geometry. Instead, we generate pressure waves at the round and oval windows (see Sec. 2.1) with a certain phase shift between them. In our model, the Scala Vestibuli and the Scala Tympani are disconnected, finishing in a wall at $\theta = 5\pi$, where we impose free boundary conditions. In addition, since the cochlea is surrounded by bone, we implement damped bounce-back conditions at the remaining walls.

The pressure sources at the round and oval windows have the following functional form:

$$P_{source}\left(r,\,\theta,\,\phi\right)) = \begin{cases} \mathcal{A}\sin(\omega t)\delta\left(\theta\right)\Omega\left(r - \frac{r_{max}-r_{min}}{2}\right)\Omega\left(\phi - \pi/2\right) & \text{if } \phi > 0 \\ \mathcal{A}\sin(\omega t - \mathcal{P} + \pi)\delta\left(\theta\right)\Omega\left(r - \frac{r_{max}-r_{min}}{2}\right)\Omega\left(\phi + \pi/2\right) & \text{if } \phi < 0 \end{cases},$$

(6-10)

where $\mathcal{A}$ is the amplitude, $\mathcal{P}$ is the phase shift between the two windows and ω is the frequency of the incoming sound. The function δ is the Dirac's delta and

$$\Omega(x) = \begin{cases} 1 & \text{if } |x| < d \\ 0 & \text{if } |x| > d \end{cases}.$$

(6-11)

We have chosen $d = 3$ cells in ϕ.

The amplitude $\mathcal{A}$ for the vibration, taken as the characteristic sound pressure, the audible frequency range and the corresponding wavelengths λ for a sound speed $c = 344000$ mm/s are shown in the Table 6.1.2.

Magnitude	Lower Value	Larger Value
$\mathcal{A}\left[\frac{\text{N}}{\text{mm}^2}\right]$	2×10^{-11}	6×10^{-5}
ω [Hz]	20	20000
λ [mm]	17,2	17200

Table 6-1.: Audible sound values for pressure, frequency and wavelength

The phase $\mathcal{P}$ has been chosen as twice the time taken by the wave to reach the apex. The reason for this choice is to model that wave starts in the oval window, goes to the apex through the Scala Vestibula and travels back to the round window through the Scala Tympany. The oscillation on the round window is almost in counterphase respect to the one at the oval window. This keeps the fluid volume constant inside the Cochlea. This counterphase adds the additional π in the second expression of Eq. (6-10).

6.2. Waves simulated by LBM

The simulations are implemented on a computational domain of 20 cells in the r direction, 200 cells in the θ direction and 20 in ϕ. Fig. 6-3 shows the simulated waves inside the Cochlea

and the pressure values on the surface with $\phi = 0$, where the Basilar membrane lays. For this picture we have chosen the E7 tone whose wavelength is λ=130.8mm.
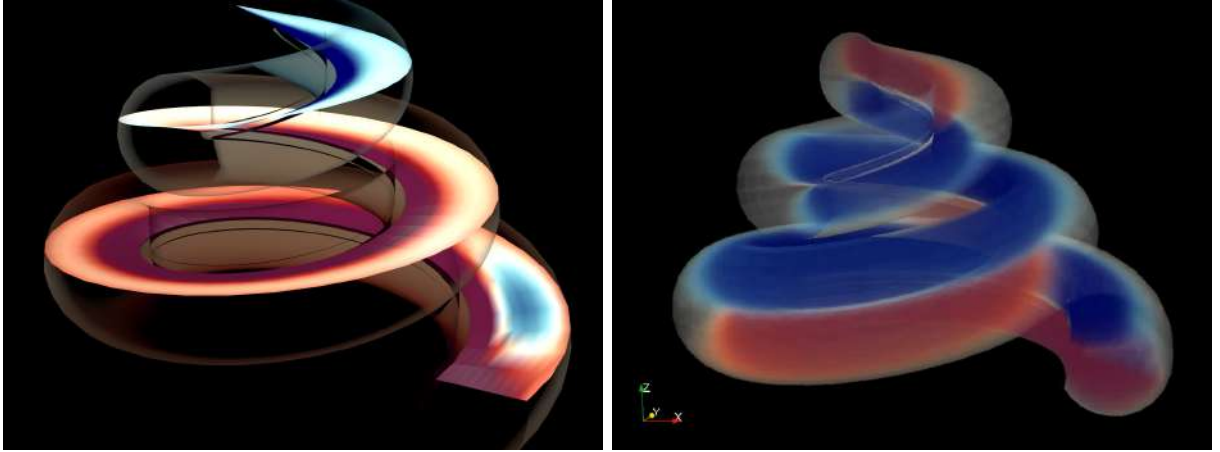
Figure 6-3.: Net pressure on $\phi = 0$, the surface where the Basilar Membrane lays (Left) and Pressure waves inside the Cochlea(Right)

Let us recall that the main function of the Cochlea is to separate the frequencies of the incoming sound. As Békésy [2] found, higher frequencies generate wider vibrations of the Basilar membrane near to the windows and, the location of the maximal amplitude goes closer to the apex when the frequency gets lower. This effect can be seen in Fig. **6-4**, where we have plotted the difference of the pressure over and under the surface $\phi = 0$ where the Basilar membrane is placed.
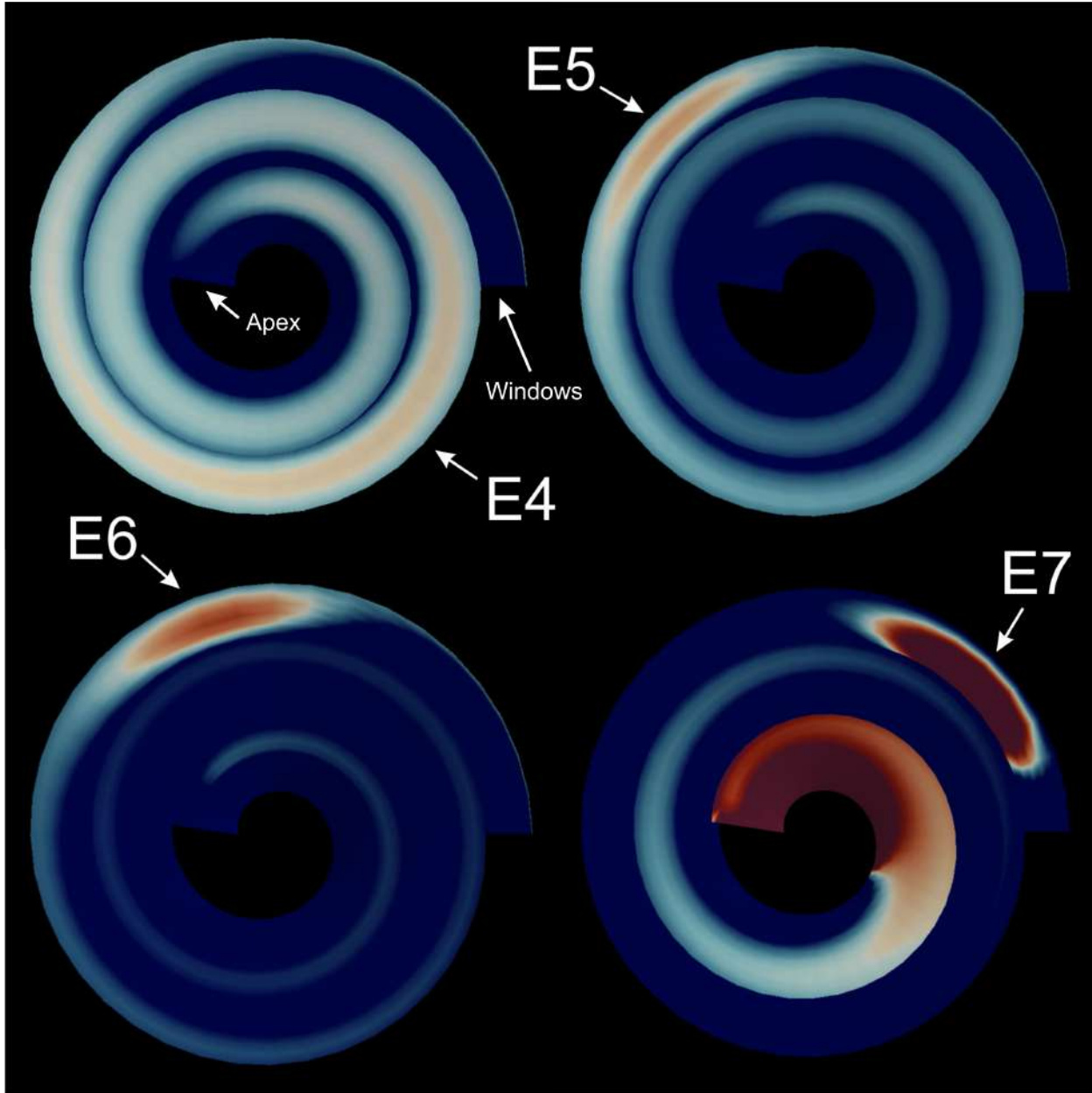
Figure 6-4.: Pressure waves on the surface with $\phi = 0$, where the Basilar Membrane lays. For 4 different wavelengths 1046.6 mm, 523.3 mm, 261.7 mm and 130.8 mm corresponding to the standard tones E4, E5, E6 and E7 respectively.

The tones in Fig.**6-4** are separated by one octave each. At high frequencies the vibration has maximal amplitude close to the windows and, lower frequencies shift this maximal amplitude to the apex. Furthermore, the regions corresponding to the higher frequencies are also more defined and delimited, as expected [3, 4].

To perform a thorough study of the frequency response of the cochlea, we proceed in two ways: First, we choose three points on the Basilar membrane and measure the pressure

intensity as a function of the frequency, as we did in last Chapter for other geometries. Results are shown in Fig. **6-5** .
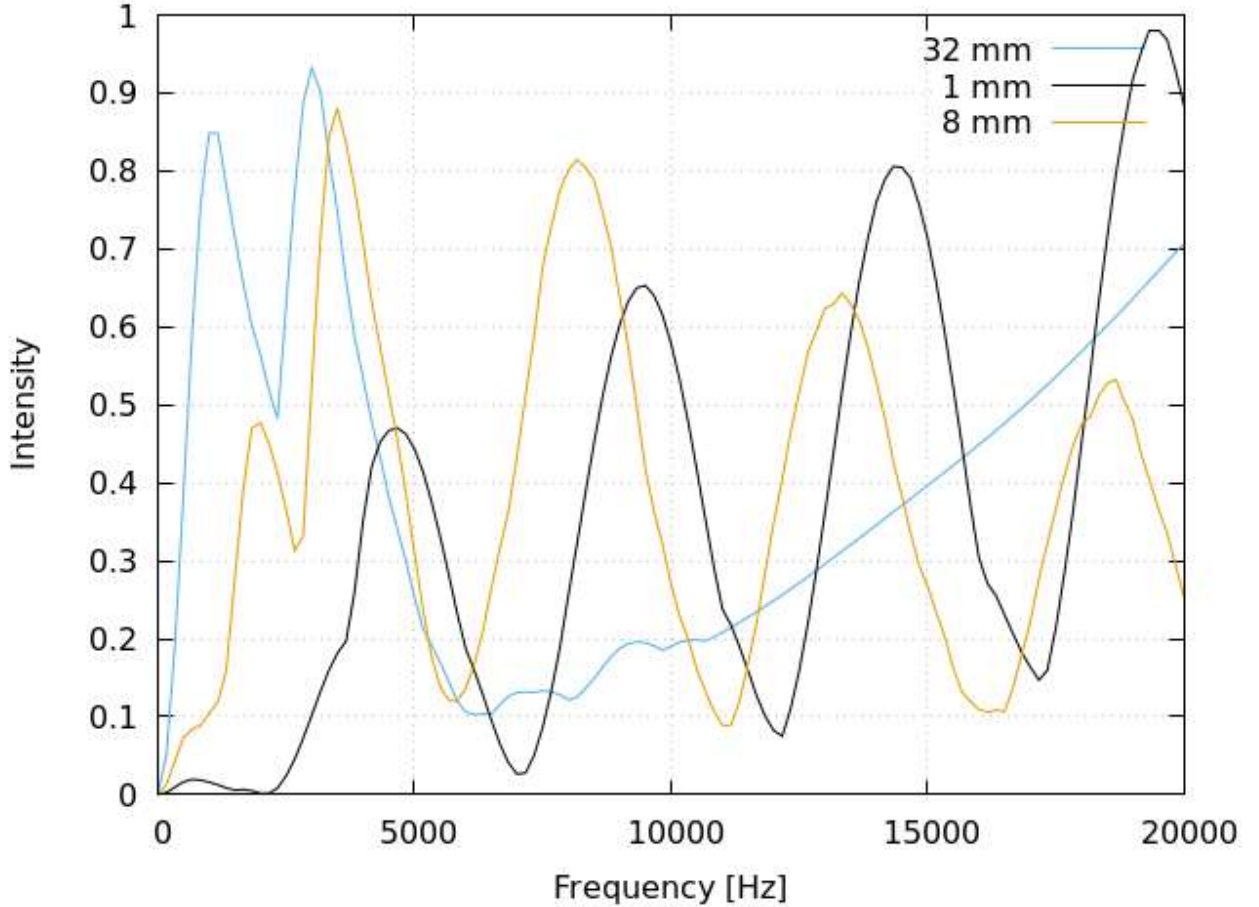
Figure 6-5.: Pressure intensity inside the cochlea measured in three different points for a range of frequencies $0 < \omega < 20$kHz. The distance is measured from the oval and round windows, 0 mm means $\theta = 0$ and 32 mm is at $\theta = 5\pi$. In this measurements $r = \bar{r}$ and $\phi = 0$

Lower frequencies show larger amplitudes for points near to the apex while the higher ones exert a maximum of pressure at points near to the windows, as before. The point at the apex (light blue line) experiments larger intensities at low frequencies. In contrast, a point placed at 8mm from the windows will experiment higher values of pressure for intermediate frequencies; actually, this is the point that experiments the largest values of pressure when $\omega \approx 7000$Hz. At very high frequencies (20kHz), the point located close to the base has the largest intensity. It can be seen, in addition, that all three points have a relatively high value of pressure within 2500Hz and 5000Hz. Indeed, at these frequencies the maximum of intensity is more distributed along the Cochlea, as can be observed in Fig **6-4**.

Second, we measure the pressure intensity along the whole Cochlea for different values of
the input frequency (Fig. **6-6**).
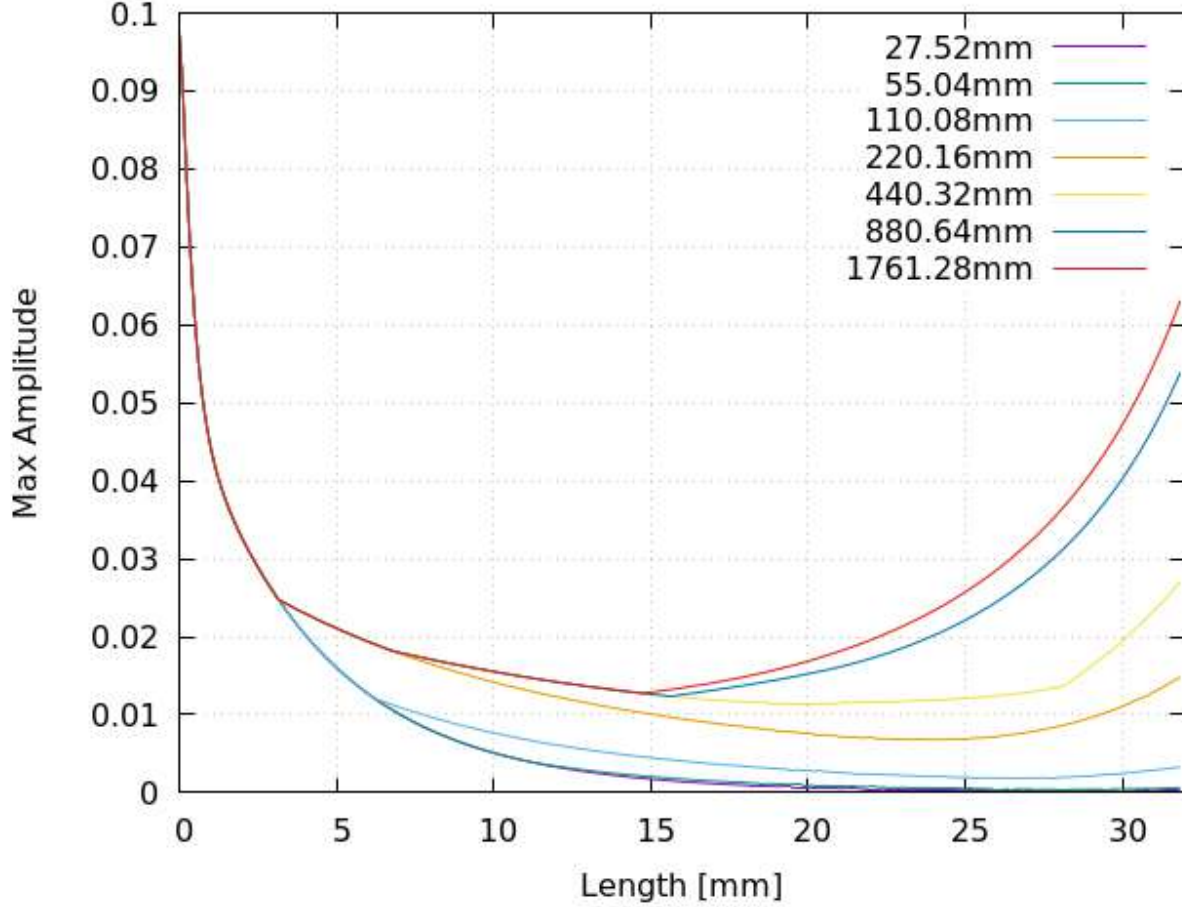
Figure 6-6.: Maximum amplitude after 15000 time-steps along the cochlea for different
input wavelengths. 0 mm means $\theta = 0$ and 32 mm is at $\theta = 5\pi$. In this
measurements $r = \bar{r}$ and $\phi = 0$

As expected, lower frequencies shown peaks of intensity near to the Cochlea's windows.
When the frequency increases, the peak becomes less sharp, which again explains that at
low frequencies the pressure is more distributed along the Cochlea. High frequencies show
peaks of intensity near to the apex as expected.

Now we have constructed a lattice-Boltzmann model which allow us to simulate the acoustic
waves inside the cochlea and measure the pressure difference exerted on the surface where
basilar membrane is located. This completes the main aim of this work. It is worth to point
out that the acoustic waves alone show already the effect of frequency segregation along the
Cochlea, something that is usually attributed to the Basilar membrane only. Nevertheless, it
could be interesting to use the simulated pressure profile on the basilar membrane to study

its displacement, since it has been reported to be the main actor in the frequency segregation, and find out how the simulated pressure waves act to bolster this process. Due to the lattice-Boltzmann model can not simulate the elastic behaviour of the basilar membrane, this should be done, for example, by using the finite element method.

In the next Chapter we describe a finite element model of the basilar membrane and construct a novel immersed boundary method to couple the finite elements with the pressure data obtained from lattice-Boltzmann.

7. The Bassilar Membrane

In the previous chapter we have obtained the net pressure profiles on the surface $\phi = 0$, now, it is interesting to focus on the realistic geometry of the Basilar Membrane (The blue strip of Fig. **6-2**) in order to, in future, study its dynamical behaviour due to the simulated pressure waves. The geometry can be obtained imposing an additional restriction in r on the surface $\phi = 0$, the restriction is

$$\bar{r} - \left(\frac{13(r_{max} - r_{min})}{36 \times 5\pi} \theta + \frac{(r_{max} - r_{min})}{18} \right) \leq r \leq \bar{r} + \left(\frac{13(r_{max} - r_{min})}{36 \times 5\pi} \theta + \frac{(r_{max} - r_{min})}{18} \right),$$

$$(7\text{-}1)$$

where $\bar{r} = 0.5(r_{max} + r_{min})$. This conditions allow us to model the realistic dimensions of the Basilar membrane in the r direction. That region is shown in Fig. **7-1**
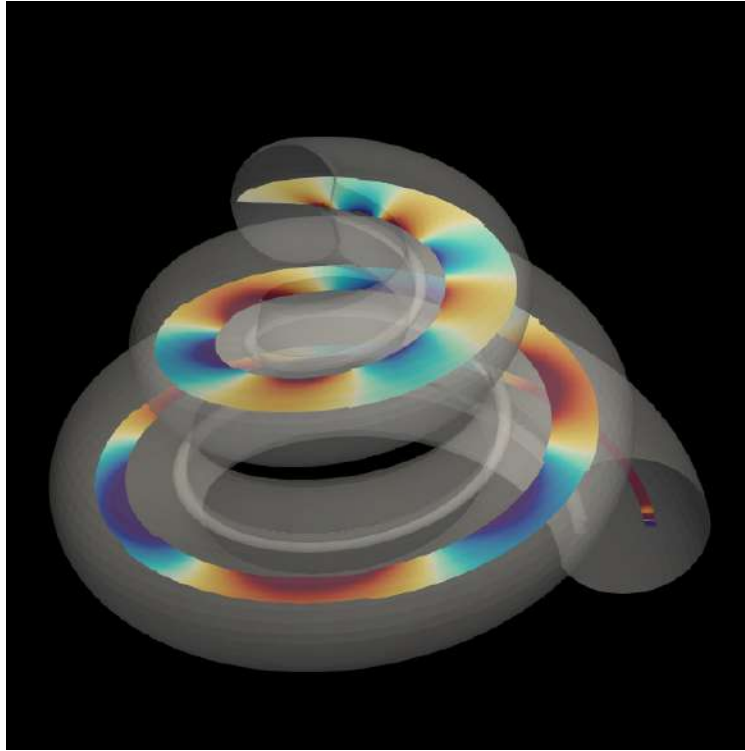
Figure 7-1.: Basilar Membrane inside the Cochlea

To simulate the dynamics of the basilar membrane we need two new models: First, the

basilar membrane modelled as an elastic beam and simulated via Finite Element Method (FEM), and second, an immersed boundary model to couple the pressure profiles from LBM with FEM. In the following sections we describe the FEM of the Basilar Membrane and the construction of a novel immerse boundary method for the interaction between acoustic waves and solid movable objects.

7.1. Finite Elements Model

With the geometry of the basilar membrane established, Professor Martin Estrada and Professor Dorian Linero from the Civil Engineering Department of the Universidad Nacional de Colombia designed a Finite Element model of the Basilar membrane (Fig. 7-2). Let us recall that the width of the basilar membrane is 0.1 mm at the base and 0.5 mm at the apex, while its thickness goes from 7.5×10^{-3} mm at the base to 2.5×10^{-3} mm at the apex.

Figure 7-2.: Basilar Membrane inside the Cochlea modelled in Finite Elements

The finite elements are shell type. The membrane is clamped both in rotation and displacement in three of its borders and free in the border at the apex. It Resembles exactly the boundary conditions of the real Basilar membrane. With the Finite element model, Professor Estrada and Professor Linero performed an linear dinamic modal analysis to find the normal vibrational modes of the Basilar membrane in the software Ansys. Some of these modes are shown in Fig. **7-3**.
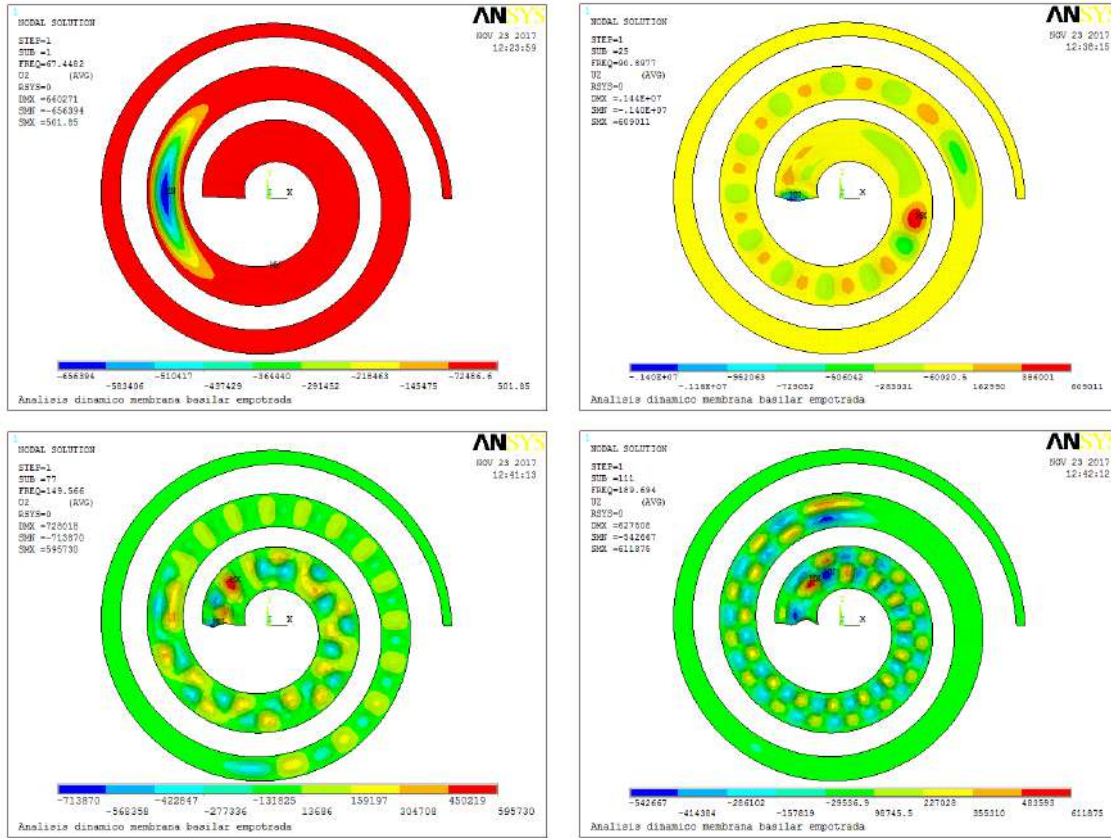
Figure 7-3.: Some normal modes of the Basilar membrane found from Finite Element simulation. The frequency increases left to right and top to bottom

Note that here, higher frequencies normal modes also reaches points closer to the base of the cochlea. A coupling between a dynamical Finite Elements simulation and our lattice-Boltzmann method could show the bidirectional interaction between the acoustics of the Cochlea and the mechanical behaviour of the Basilar membrane. To be able to perform these future simulations we constructed a novel lattice-Boltzmann method for solid movable objects immersed in a compressible medium. This approach is based on the immersed boundary method proposed by Favier, Revell and Pinelli [43] for the coupling between immersed solid structures and fluids. We describe our model below.

7.2.   Immerse boundary method for the interaction between waves and solid movable objects.

7.2.1.   Action of the wave on the solid.

In a lattice-Boltzmann method the information is located on the lattice nodes, which remain fixed in space during the simulation. In contrast, the solid immersed object moves in space as time goes on. Let us divide the boundary of the solid immersed object into a set of M discrete surfaces, each one almost flat, with surface vector $\Delta \vec{s}_k$ pointing out of the object and centered at point $\vec{\bar{R}}_k$. Let us remember that we know the wave presure on each lattice node,

$$P = \sum_i f_i^{eq} \quad ; \tag{7-2}$$

therefore, it is only necessary to determine how this pressure acts on the body surface. For this end, we interpolate among the nodes to find the value of the pressure at each point $\vec{\bar{R}}_k$ with a kernel function $\tilde{\delta}(r)$,

$$P\left(\vec{\bar{R}}_k\right) \simeq \sum_l P\left(\vec{y}_l\right) \tilde{\delta}\left(\vec{y}_l - \vec{\bar{R}}_k\right) \quad , \tag{7-3}$$

where the sum extends on all positions y_l of the lattice Boltzmann nodes. In the present work we will use the kernel $\tilde{\delta}$ defined as (Fig. **7-4**)

$$\tilde{\delta}(r) = \begin{cases} \frac{1}{6}\left(5 - 3|r| - \sqrt{-3(1-|r|)^2 + 1}\right) & \text{if } 1/2 \leq |r| \leq 3/2 \\ \frac{1}{3}\left(1 + \sqrt{-3r^2 + 1}\right) & \text{if } |r| \leq 1/2 \\ 0 & \text{otherwise} \end{cases} \tag{7-4}$$

The total force exerted by the fluid on the immersed solid is, therefore,

$$\vec{F}_{ws} = -\sum_{k=1}^{M} P\left(\vec{\bar{R}}_k\right) \Delta \vec{s}_k \quad . \tag{7-5}$$

Once the force acting on the object has been found, we can use any integrator to move the object and update its velocity and position on each timestep.

7.2.2.   Action of the solid on the wave

Following the proposal of Favier, Revell and Pinelli, we introduce a forcing term at the discrete boundary solid points which ensures that the displacement velocity of the wave in the boundary matches the velocity of the discrete solid. Since the first moment $\vec{J}$ of

the lattice-Boltzmann model is proportional to the velocity displacement $\vec{D}$ (Eq. 3-21), the forcing term will be indeed a change of the quantity $\vec{J}$, i. e.

$$\vec{F}(\vec{R}_k) = \frac{B\vec{U}_k - \mathcal{I}\left(\vec{J}\right)(\vec{R}_k)}{\Delta t} \quad . \tag{7-6}$$

Here $\vec{R}_k$ is the position of the k-th boundary solid point, $\vec{U}_k$ is the velocity of that solid point (obtained from integrating its movement equations), and $\mathcal{I}\left(\vec{J}\right)(\vec{R}_k)$ is the interpolated value of $\vec{J}$ at $\vec{R}_k$,

$$\mathcal{I}\left(\vec{J}\right)(\vec{R}_k) = \sum_l \vec{J}(\vec{y}_l)\,\tilde{\delta}\left(\vec{y}_l - \vec{R}_k\right) \quad , \tag{7-7}$$

where $\vec{y}_l$ is the position of the l-th lattice node within the influence area (which, for the kernel Eq.(7-4) is just three cells width, see Fig. 7-4).
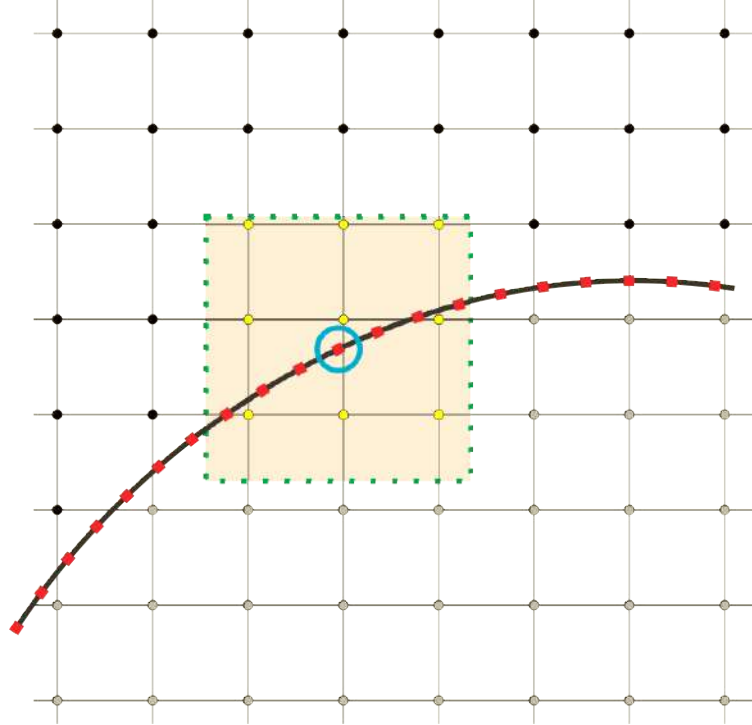
Figure 7-4.: Influence area for a given discrete boundary point (within the circle)

Because this forcing term is located at the discrete boundary points, it is necessary to spread it out to the lattice nodes in order to force the wave simulated by the lattice-Boltzmann. This can be done by using the same interpolation kernel. The force on the l-th lattice node is

$$\vec{f}(\vec{y}_l) = \sum_{k=1}^{M} \vec{F}_{bp}(\vec{R}_k)\,\tilde{\delta}\left(\vec{y}_l - \vec{R}_k\right)\epsilon_k \quad , \tag{7-8}$$

where ϵ_k is a value that ensures the consistency between the interpolation and posterior spreading process, as follows. Let us fix a force at a certain solid point $\vec{R}_k$. Spread the force forth to the lattice nodes Eq. (7-8) and back to the point $\vec{R}_k$ Eq. (7-7). If the returned value is the same as the original one, the value of ϵ_k is right.

Unlike the model proposed by Favier, Revell and Pinelli, and as shown in Sec. 4.3 the force Eq. (7-8) will not be included in the collision term, because $\tau = 0.5$, but just in the definition of the macroscopic quantity $\vec{J}$,

$$\vec{J}(\vec{y_l}) = \sum_i \vec{\xi_i} f_i^{eq} + \frac{\Delta t}{2} \vec{f}(\vec{y_l}) \tag{7-9}$$

That completes the wave-solid interaction.

The proposed method is completely general and can implement the interactions between wave and solid in many different phenomena. Furthermore, if desired, it also allows to propagate waves inside the solid, with the same or a different propagation speed, as we will illustrate with some examples.

7.2.3. Simulations and discussion

To test our model, we first study the effect of a mechanical wave on the movement of an object initially at rest. To this aim, we place a two-dimensional solid disk at the center of the computational domain and we define a sinusoidal perturbation coming from a corner of the domain. The boundary conditions at the walls are bounce-back with a damping factor equal to 0.6 in order to control the amplitude of the perturbation and achieve an stationary state. The resulting movement and the pressure profile is shown in the Figure **7-5**
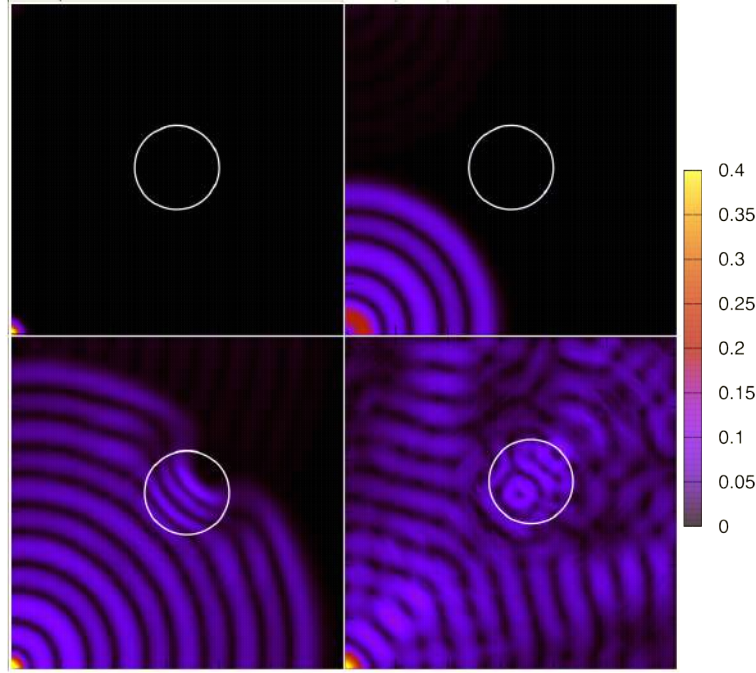
Figure 7-5.: Displacement of a solid disc generated by a polar wave

Note how the disc is displaced from the center in the same direction of the wave and the circular wavefront is disturbed by the change of velocity within the solid (bottom-left image). In order to track the displacement and make a more detailed study of the interaction, we trace the trajectory of the disk for simulations of different wave frequency and velocities ratio $n = v_s/c$ where v_s is the wave velocity inside the solid and $c = 0.1$ in the medium, Figure **7-6** shows the result
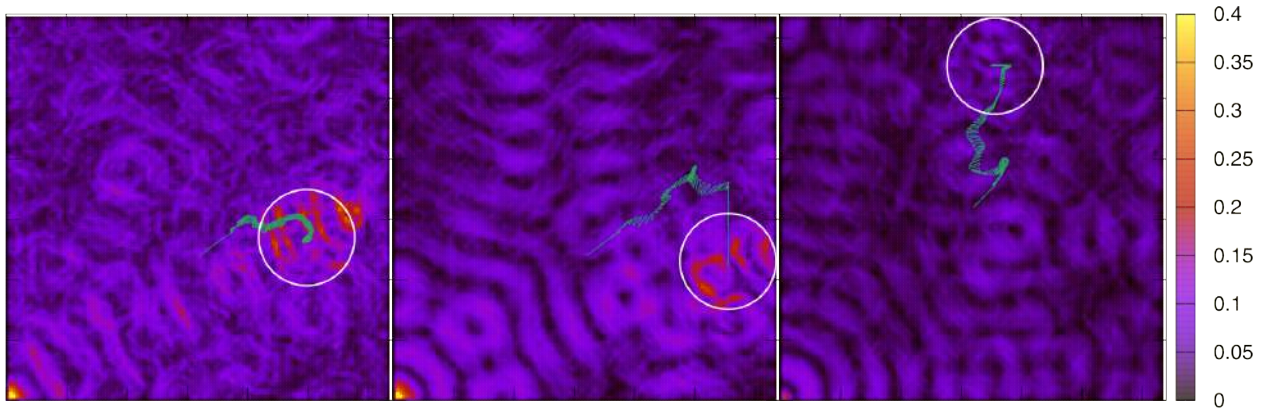
Figure 7-6.: Trajectory of the disk after 3000 time steps for frequencies 5.25, 5.25 and 5.75, and velocity ratios 0.6, 0.5, and 0.6 respectively from left to right

Where the frequency and velocity are measured in units of time steps $\Delta t = 1$ computing

clock pulse and unitary cells. Note that the trajectory greatly depends on the value of n and the frequency of the wave. The Figure 7-7 shows the relation between the displacement of the disk as a function of the frequency, for different values of n of a straight line trajectory.
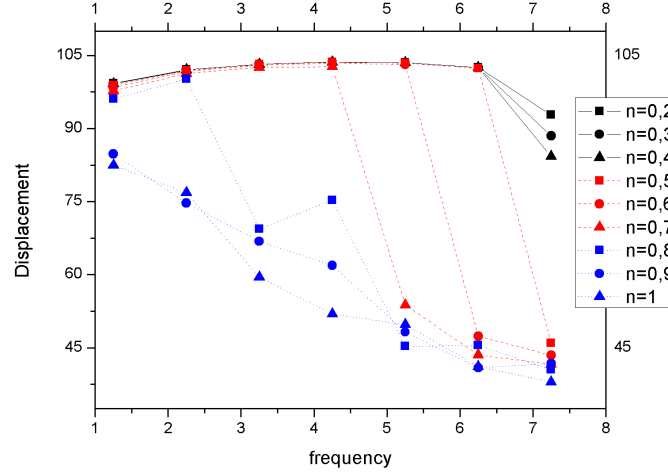
Figure 7-7.: Displacement of the disk as a function of the wave frequency for different values of n

As expected, disks whose wave velocity at the interior is lower show a greater displacement than disks that do not present such a high resistance to the pressure vibrations. Respect to the frequency the displacement has a decreasing behavior, higher frequencies displaces the disk a shorter distance. This effect is stronger when the velocity of the wave inside the disk is 0.8, 0.9 and 1 times c (blue dotted lines), i.e. when the material has a low rigidity, for values of n equal to 0.5 0.6 and 0.7,(red dashed lines) there is a cutoff frequency from which the wave crosses the disk displacing it a considerably shorter distance. Note that the lower the velocities ratio is, the higher the cutoff frequency gets, this means that it is necessary a higher frequency to overpass a more rigid object. Furthermore, the relation between the displacement and the frequency for values of $n < 0.7$ is increasing for frequencies under the cutoff, even for n equal to 0.2, 0.3 and 0.4, where the skip is not too abrupt and the cutoff frequency does not appear clearly.

As a second part of our tests we start from a medium at rest and apply a force to the solid object in order to study the generated wakes. Figure 7-8 shows the wake generated by a disk with $n = 0.6$ at different time steps until it crashes with the bottom boundary.
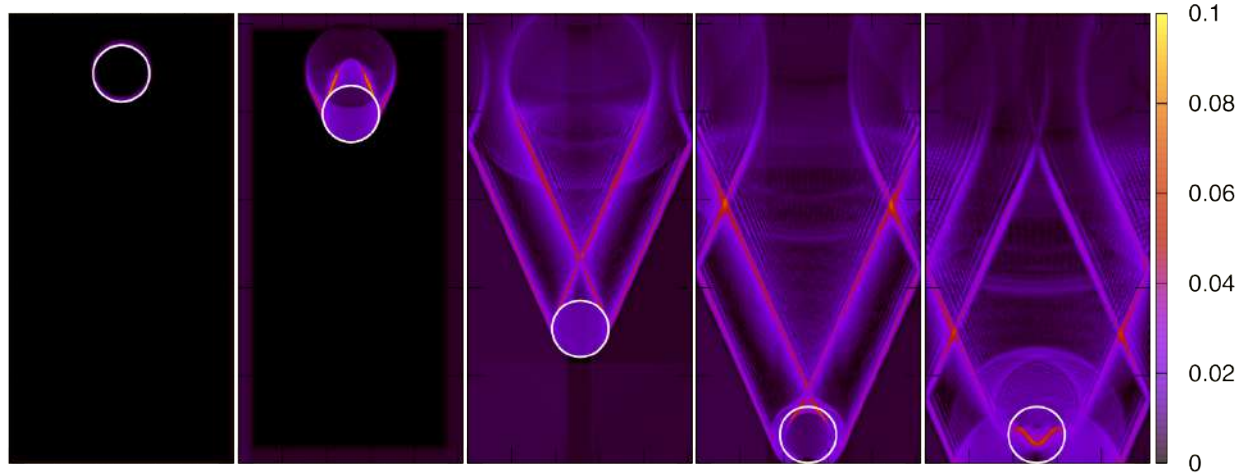
Figure 7-8.: Accelerated disk moving downwards in a medium. Frames taken at 10, 100, 600, 900, and 1200 time steps

The resulting wake is qualitatively as expected, it expands as the disk advances and a new wave moving out of the disk is generated when it hits the bottom wall. It is also interesting to study how the shape of the solid object influences the creation of the wake. Simulations of the same system for different shapes of the solid are shown here in Figure **7-9**.
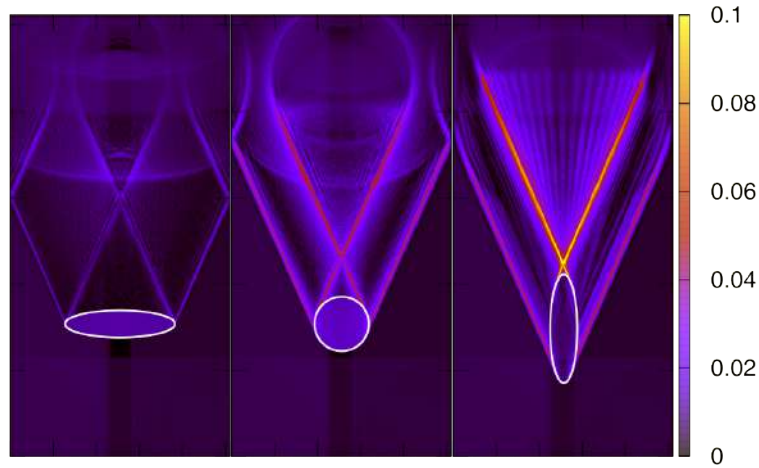
Figure 7-9.: Wake generated from accelerated objects of different shapes.

The results show that a sharper front of the moving object generates a stronger wake, i. e. the vertical ellipse generates a higher pressure behind it and the triangle formed by the intersection of the both sides of the wake tends to disappear when the solid becomes sharper. The value of the angle formed by the wake respect with the vertical axis is compared with the theoretical expextations, this angle, known as Kelvin's angle [44] should be of 19.5° . Our results shown a deviation of 15 % approximately (Fig. **7-10**), which can be due to the low order aproximation on the lattice velocities discretization(D2Q5).
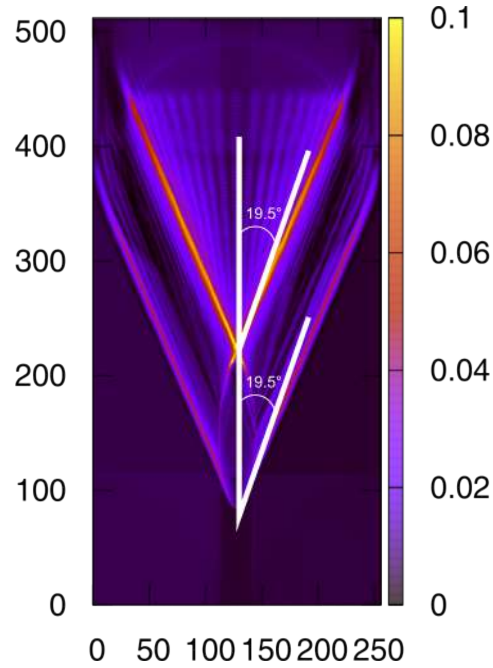
Figure 7-10.: Comparison between the obtained wake angle and the expected Kelin's Angle.

In addition, we study the convergence of our model by measuring the displacement of a rigid object due to the interaction with a pressure pulse as a function of the cell size ε, the result is shown here
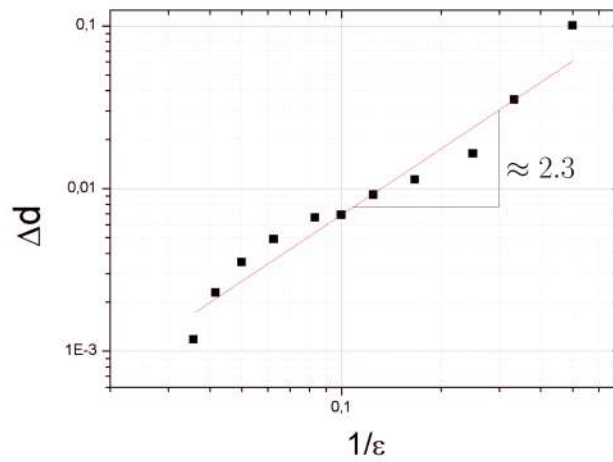
Figure 7-11.: Logarithmic graph of the error in displacement of an object as a function of the lattice resolution.

where Δd is the difference between the measured displacement and a theoretically known value. Fig. **7-11** shows that our model has second order accuracy, since the slope found was

2.3 approximately.

This proposed method simplifies the Immersed Boundary method for hydrodynamic simulations since it is not interested in the fluid dynamics but in the linear behaviour of the waves. The model is easy to implement and allows us to control some physical variables like the pressure of the medium and the velocity of propagation inside and outside the solid object, in addition, the shape of the object is controlled by the position of the boundary points, whose dynamics is updated every time step, due to this fact, the shape of the object can be easily modelled and the simulation of flexible objects can be include naturally just by changing the dynamics of the rigid body. Therefore, the constructed immersed boundary model is adequate to couple with the finite elements simulations of the basilar membrane. This dynamical by-directional coupling is left for future works.

8. Conclusions

This work constructs a lattice-Boltzmann model for the simulation of acoustic waves in general coordinates and successfully applies it to the simulation of the Cochlea. The method is capable to simulate the wave equation in any coordinate system. Although it keeps the standard structure of the lattice-Boltzmann on Cartesian coordinates in the computer memory, it reproduces the wave equation in general coordinates in the macroscopic limit. This is achieved by rescaling the macroscopic quantities by the cell volume and by adding as forcing terms the additional expressions that appear in the wave equation due to the coordinate transformation. As consequence, the method allow us to easily change the geometry just by setting the proper metric tensor and Christoffel symbols. The proposed lattice-Boltzmann maintains second-order accuracy and keeps the isotropic propagation of waves, even if the lattice is not isotropic. In addition, it allows to take advantage of axial or radial symmetries to handle three-dimensional problems with two-dimensional computational domains. Compared with previous attempts, our approach does not need any additional interpolation step and, the boundary conditions can be applied as usual on the Cartesian lattice of the simulation domain, even though the boundaries are curved. Summarizing, our proposal is a really valuable contribution to the implementation of acoustic simulations via the lattice-Boltzmann model.

Achieving the correct construction of the model was not an easy task; as a matter of fact, it is the culmination of a process with several attempts. Three different functional forms for the equilibrium distribution were proposed. The first one was obtain by following the moment matching procedure with an Anzatz satisfying the definition of the macroscopic fields. This first approach was easy to implement and correctly simulated radial waves and normal modes of a cylinder. Nevertheless, its weak stability restricted the application to systems with axial symmetry and the evolution in the real space was not isotropic. Our second approach was based on a Hermite series expansion of the equilibrium distribution function. The result adds some terms to the one before that increase the stability of the model and, allowed us to simulate more general systems without axial symmetry. However, the lack of isotropy was still present in the evolution. This second approach enlightened the cause of the problem and guided us to design an additional forcing term to recover the isotropy. The third approach corrects the equilibrium distribution function by moving an element from there to the forcing terms. The modification allowed us to retrieve correctly the isotropy in real space and to recover both stability and second order accuracy.

With this third approach in hand we simulated the pressure waves inside a cylinder, a trumpet and a torus. The cylinder had an open end and the pressure waves inside were generated in two ways: from an uniform plate of equal radius at the closed end or from a small ring there, which also excited the radial modes. With the oscillating ring as source, the method successfully reproduces the normal vibrational modes inside the cylinder in both longitudinal and radial directions. The characteristic frequencies we obtain laid between $1\,\%$ respect to the theoretical expectations. A bell was added at one end of the cylinder by introducing a suited coordinate system. The bell suppresses the resonances at high frequencies and reduces the pressure amplitude at the open end, as expected. For the torus, three different wave sources were employed: An oscillating ring along major circle of the Torus, a ring along the minor circle of the torus and a point source placed in a general general place inside the torus. Each of these sources activates different normal modes. Interestingly, the intensity shows against frequency a similar pattern to the one of a trumpet.

Once the model was tested,we addressed the simulation of the Cochlea. That was achieved by designing a coordinate transformation that resembles the its geometry in a very realistic way. First, the cross section of the torus was modified from a circle to a cardioid. After, a linear decrease of the radius of the major circle of the torus was added as a function of the whirl angle and, its maximum was chosen to give 2.5 turns. Next, a linear vertical elongation was imposed to generate the spiral helix. Finally, the cross section was multiplied by a decreasing factor to model the tube tampering. The geometry constructed in this way allow us to add the Basilar membrane (and the Reissner membrane in future works, too) as a surface with a constant value of ϕ. The whole geometry is defined by 4 parameters which were adjusted to closely fit the real anatomic shape. The physiological performance of the Cochlea was modelled by adding two plane sources, one at the entrance to the Scala Vestibula simulating the oval window and, the other at the entrance of the Scala Tympany simulating the round window. The two sources oscillate in counter-phase, an additional phase shift was added to model the wave starting from the oval window, going to the apex through the Scala Vestibula and travelling back to the round window through the Scala Tympany. An additional simulation with just one source placed at the oval window generates waves going to the apex and back to the round window showed similar results but it was less stable.

When the system was excited with high frequencies we found that the net pressure on the Basilar membrane shows larger amplitudes near to the windows, while the oscillations at lower frequencies located closer to the apex (the end of the cochlea). Additionally, the signal for high frequencies is more defined an bounded, whereas for lower frequencies we have more distributed pressure profiles. These results are in agreement with the reported in the literature for the Basilar membrane alone, oscillating as a rigid plate. That behaviour of the basilar membrane was also reproduced with the help of Profesors Martin Estrada and Dorian

Linero from the Civil Engineering department by running Ansys to find the normal modes of the Basilar membrane. It is remarkable that the geometrical shape of Cochlea alone can reproduce the frequencies segregation, strengthening the localization effect of the mechanical response on the basilar membrane. In addition, an immersed boundary lattice-Boltzmann method for acoustic waves was constructed and tested. That would allow to couple our acoustic simulation to the mechanical model of the Basilar membrane. Such coupling is a very relevant subject for future work.

The constructed method shows to be very efficient and requires very low computational resources. The simulations ran on an Intel core i7 processor whose operation frequency was 3.4GHz. The computational time was less than 3 minutes per simulation (around 10000 timesteps). Furthermore, since all the information needed to update the values of the distribution functions are stored in the same cell, lattice-Boltzmann method is highly parallelizable. As consequence, running the presented method in parallel, written for example in CUDA, would reduce the computational time by three orders of magnitude. This is something to do in the near future.

The presented lattice-Boltzmann model can be used to simulate further musical instruments with complex shapes, the acoustics inside theatres or urban noise, among others. The applicability range is really wide, because the simulations can be made for very complex shapes just by choosing the appropriate coordinate transformation. Indeed, the model allows for continuous coordinate transformations in real time, just by varying the transformation parameters and, the transformation itself could be modified to reach higher resolutions in some regions of space. Even though, the coordinate transformation would not be restricted to analytical expressions, since the metric tensor and the Christoffel symbols could be computed numerically to match a very general set of points. Those features would expand the applicability and generality of the developed model. In addition, the procedure shown here can be also used to design lattice-Boltzmann methods on curvilinear coordinates for other physical phenomena, like diffusion or electrodynamics. All these are interest topics for future research. It is also worth to mention that our model for the Cochlea is available to perform further physiological studies, like the effect of the Reissner membrane or the otoacoustic emissions, among others, and it can be useful to design better hearing aid devices.

This work designs and implements a lattice-Boltzmann model for waves on curvilinear coordinates. The model is completely general and, thus, offers a huge amount of possible applications and future developments in different research areas. Furthermore, the model draws a path to overcome the limitations of standard lattice Boltzmann models on Cartesian coordinates. The method constitutes, therefore, a valuable contribution to the field of lattice-Boltzmann simulations.

A. Appendix:Fields Derivatives using lattice-Boltzmann Scheme

In some cases, it is necessary to compute the derivative of any scalar or vectorialField during a lattice-Boltzmann calculation, this can be done by implementing a discretization scheme likeFinite differences scheme, however, it can either reduce the accuracy order of the overall scheme or increase the computational time and model complexity. However, there is an useful alternative to compute the gradients of theFields that are involved in the lattice-Boltzmann simulation.

The procedure toFind these gradients is described here. Let us startFrom a Taylor expansion of theField in the direction of a given discrete velocityFrom the discrete set used in the lattice-Boltzmann calculations.

$$\phi\left(\vec{x}+\delta_t\vec{\xi_i}\right) = \phi\left(\vec{x}\right) + \delta_t\vec{\xi_i}\nabla\phi\left(\vec{x}\right) + \delta_t^2\frac{\xi_i^\alpha\xi_i^\beta}{2}\nabla_\alpha\nabla_\beta\phi\left(\vec{x}\right) + \dots, \tag{A-1}$$

now, we multiply the whole expansion by $w_i\vec{\xi_i}$

$$w_i\vec{\xi_i}\phi\left(\vec{x}+\vec{\xi_i}\right) = w_i\vec{\xi_i}\phi\left(\vec{x}\right) + w_i\vec{\xi_i}\vec{\xi_i}\cdot\vec{\nabla}\phi\left(\vec{x}\right) + w_i\frac{\vec{\xi}\vec{\xi}\vec{\xi}:\vec{\nabla}\vec{\nabla}}{2}\phi\left(\vec{x}\right) + \dots, \tag{A-2}$$

if we sum over i, we can use the isotropy conditions (3-1) to cancel the terms of odd order in $\vec{\xi_i}$

$$\sum_i w_i\vec{\xi_i}\phi\left(\vec{x}+\vec{\xi_i}\right) = \sum_i w_i\vec{\xi_i}\vec{\xi_i}\cdot\vec{\nabla}\phi\left(\vec{x}\right) + \mathcal{O}\left(\delta x^4\right) \tag{A-3}$$

and use

$$\sum_i w_i\vec{\xi_i}\vec{\xi_i} = \sum_i w_i\xi_i^\alpha\xi_i^\beta = \delta^{\alpha\beta}c_s^2 \tag{A-4}$$

to write

$$\sum_i w_i\vec{\xi_i}\phi\left(\vec{x}+\vec{\xi_i}\right) = c_s^2\vec{\nabla}\phi\left(\vec{x}\right) + \mathcal{O}\left(\delta x^4\right) \tag{A-5}$$

finally, if we divide by c_s^2 we obtain the required expression to compute the gradient of a scalar field by using the same discretization scheme implemented in the lattice-Boltzmann.

$$\vec{\nabla}\phi = \frac{1}{c_s^2}\sum_i w_i\vec{\xi_i}\phi\left(\vec{x}+\vec{\xi_i}\right) + \mathcal{O}\left(\delta x^2\right) \tag{A-6}$$

It can also be generalized to compute the gradient of any tensor $A^{\alpha\beta}$

$$\partial_\alpha A^{\alpha\beta} = \frac{1}{c_s^2} \sum_i w_i \xi_i^\alpha A^{\alpha\beta} \left(x^\alpha + \xi_i^\alpha \right) + \mathcal{O}\left(\delta x^2 \right) \tag{A-7}$$

Note that the order of accuracy is the same of the overall lattice-Boltzmann scheme, even if the chosen discrete velocities set is only second order as in our case (D3Q7).

B. Appendix:Characteristic Frequencies of a Rigid Open-Closed end Pipe

In order to define correctly the boundary condition for the rigid walls of the pipe andFind a theoretical expressionFor the vibrational modes along the radial direction, letsFirst write the differential equationFor r obtainedFrom the variables separation of the wave equation

$$\left(\frac{\partial^2}{\partial r^2} + \frac{1}{r}\frac{\partial}{\partial r} + \zeta^2 - \frac{m^2}{r^2} \right) P_r = 0 \tag{B-1}$$

whose solution is

$$P_r = A_r J_m\left(\zeta r\right) + B_r Y_m\left(\zeta r\right) \tag{B-2}$$

where $J_m\left(\zeta r\right)$ and $Y_m\left(\zeta r\right)$ are the Bessel functions of first and second kind respectively, the constants A_r and B_r can be obtained from the boundary conditions at $r = 0$ and $r = r_{max}$.For $r = 0$, since the pressure have to be finite and the Bessel function of the second kind $Y_m(\zeta r)$ diverges at $r = 0$, we have $B_r = 0$. Now replacing the Eq. B-2 into the Eq. 5-13, we find the condition

$$\zeta r \frac{\partial}{\partial \zeta r} J_m(\zeta r_{max}) + J_m(\zeta r_{max}) = 0 \tag{B-3}$$

which can be numerically solved for ζ to find the characteristic radial frequencies of the pipe. In order to simplify the above equation and its solution we use the property

$$\zeta r J'_m(\zeta r) = m J_m(\zeta r) - \zeta r J_{m+1}(\zeta r) \tag{B-4}$$

to find the function

$$f(\zeta r_{max}) = (m + 1) J_m(\zeta r_{max}) - \zeta R J_{m+1}(\zeta r_{max}) \tag{B-5}$$

whose zeros correspond to $\zeta_l r_{max}$, where ζ_l is the l-th radial characteristic frequency of the pipe.

For the simulations done in this work, we assume axial symmetry of the waves and therefore we choose $m = 0$, the figure **B-1** shows the graphic of the Eq. B-5 as a function of ζr_{max} For $m = 0$
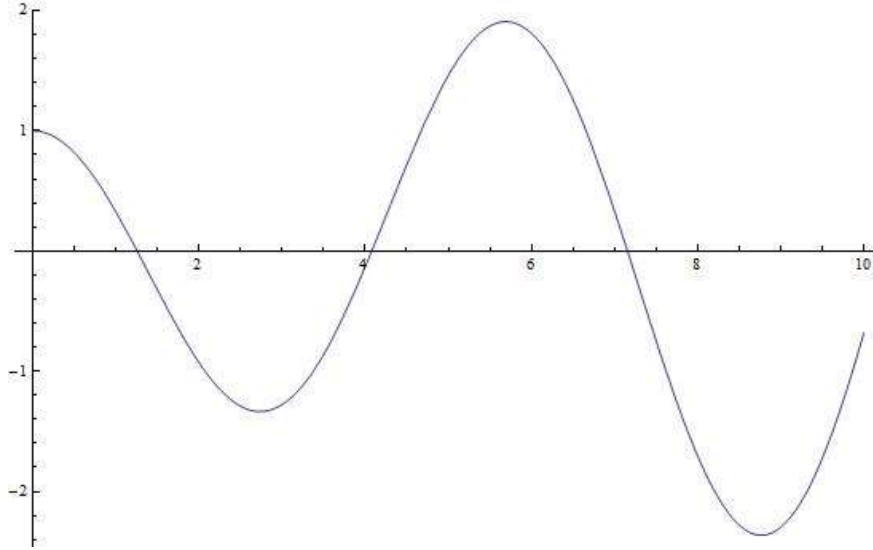
Figure B-1.: Graph of the function given by the Eq. B-5

The first three zeros of the function happen to be

Order	Value
1	1,2556
2	4,0793
3	7,1390

Table B-1.: First three zeros of the Eq. B-5

Finally, the theoretical expression for the vibrational modes inside the pipe with $m = 0$ considering both the radial and longitudinal vibrations is given by

$$\omega_{j,0,n} = c \left[\zeta_l^2 + \left(\frac{(2n+1)\pi}{2L_z} \right)^2 \right]^{1/2} \qquad . \tag{B-6}$$

C. Appendix:Geometric properties of the Systems

In this appendix we describe the coordinate transformations used to define the systems we simulate as well as the geometric properties needed to implement the LBM.

C.1. Rectangular Cells

The two-dimensional transformation done to prove the models isotropy in rectangular cells, is defined by

$$x = \Delta_x i_x$$
$$y = \Delta_y i_y$$

(C-1)

where i_x, i_y are the integers running along the lattice nodes in each direction and $\Delta_x \neq Delta_y$ is a scalingFactor that allow us to have rectangular cells in the real world. The metric tensorFor these coordinates is

$$g_{\mu,\nu} = \begin{pmatrix} \Delta_x^2 & 0 \\ 0 & \Delta_y^2 \end{pmatrix} \quad,$$

(C-2)

and its inverse

$$g_{\mu,\nu} = \begin{pmatrix} \Delta_x^{-2} & 0 \\ 0 & \Delta_y^{-2} \end{pmatrix} \quad,$$

(C-3)

the determinant of the metric tensor is

$$g = \Delta_x^2 \Delta_y^2$$

(C-4)

In this plane coordinate system all the Christoffel symbols are zero.

C.2. Cylinder

Cylindrical coordinates are given by the transformation

$$x = r \cos \theta$$
$$y = r \sin \theta \quad.$$
$$z = z$$

(C-5)

These coordinates generates the geometry shown in Fig. **C-1**
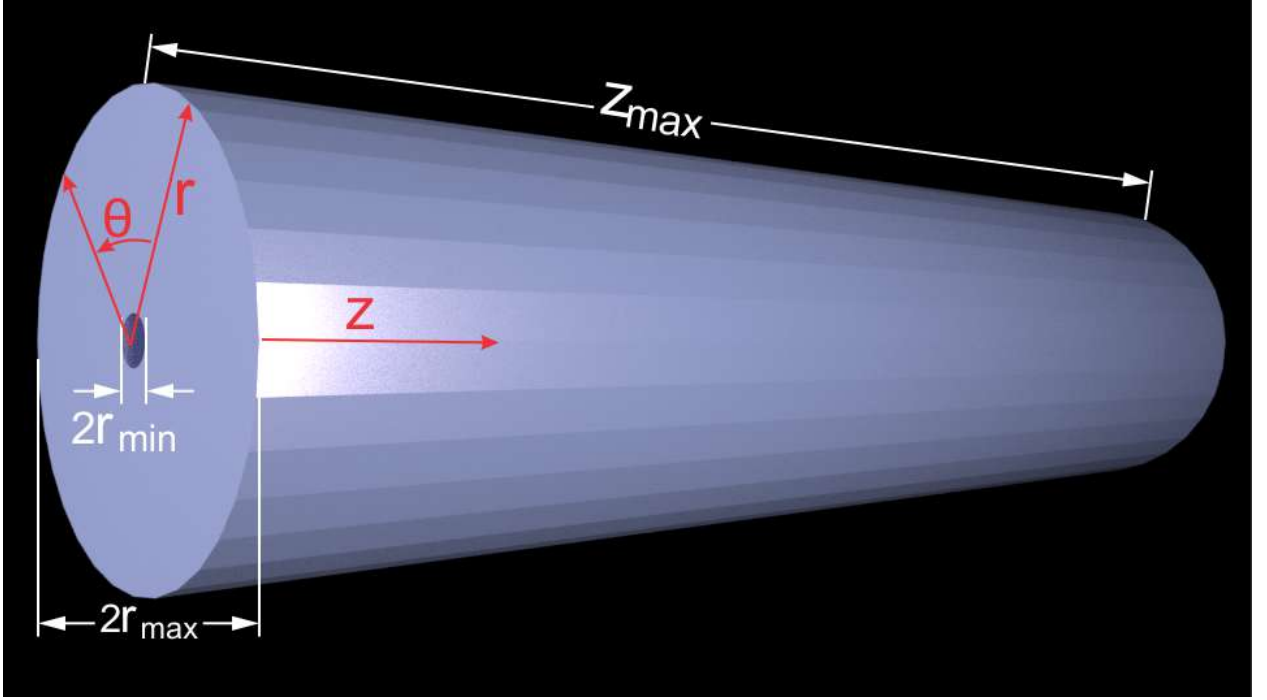
Figure C-1.: Cylinder formed by the transformation defined by the Eq. C-5

In this case, r, θ and z are continuous coordinates, we scale them and transform them to the integer number of each lattice node, this let us to control the system size and resolution independently as well as the limits of these continuous coordinates. The additional transformation reads:

$$r = i_r \Delta_r + r_{min} \tag{C-6}$$
$$\theta = i_\theta \Delta_\theta \tag{C-7}$$
$$z = z_{max} - i_z \Delta_z \tag{C-8}$$

where $\Delta_r = (r_{max} - r_{min})/L_r$, $\Delta_\theta = 2\pi/L_\theta$ and $\Delta_z = z_{max}/L_z$, and L_r, L_θ and L_z are the number of cells in each direction respectively. The metric tensor reads asFollows:

$$g_{\mu,\nu} = \begin{pmatrix} \Delta_r^2 & 0 & 0 \\ 0 & \Delta_\theta^2 r^2 & 0 \\ 0 & 0 & \Delta_z^2 \end{pmatrix} \quad , \tag{C-9}$$

its inverse

$$g^{\mu,\nu} = \begin{pmatrix} \Delta_r^{-2} & 0 & 0 \\ 0 & \Delta_\theta^{-2} \frac{1}{r^2} & 0 \\ 0 & 0 & \Delta_z^{-2} \end{pmatrix} \quad , \tag{C-10}$$

the determinant of the metric tensor

$$g = r^2 \Delta_r^2 \Delta_\theta^2 \Delta_z^2 \tag{C-11}$$

and the non-zero Christoffel symbols are

$$\Gamma^r_{\theta\theta} = \left(\frac{\Delta_\theta \Delta_\theta}{\Delta_r}\right)(-r), \quad \Gamma^\theta_{r\theta} = \Gamma^\theta_{\theta r} = \left(\frac{\Delta_\theta \Delta_r}{\Delta_\theta}\right)\left(\frac{1}{r}\right) \quad . \tag{C-12}$$

C.3. Trumpet

For the case of the trumpet, we add a modulation to the radius of the cylindrical coordinates via the parameter λ, the coordinate transformation reads

$$
\begin{aligned}
x &= r\cos(\theta)\mathcal{Z}^{-\lambda} \\
y &= r\sin(\theta)\mathcal{Z}^{-\lambda} \quad , \\
z &= z
\end{aligned}
\tag{C-13}
$$

where $\mathcal{Z} = z_{max} - z$. Again, we have the second transformation

$$
\begin{aligned}
r &= i_r \Delta_r + r_{min} \tag{C-14} \\
\theta &= i_\theta \Delta_\theta \tag{C-15} \\
z &= z_{max} - i_z \Delta_z , \tag{C-16}
\end{aligned}
$$

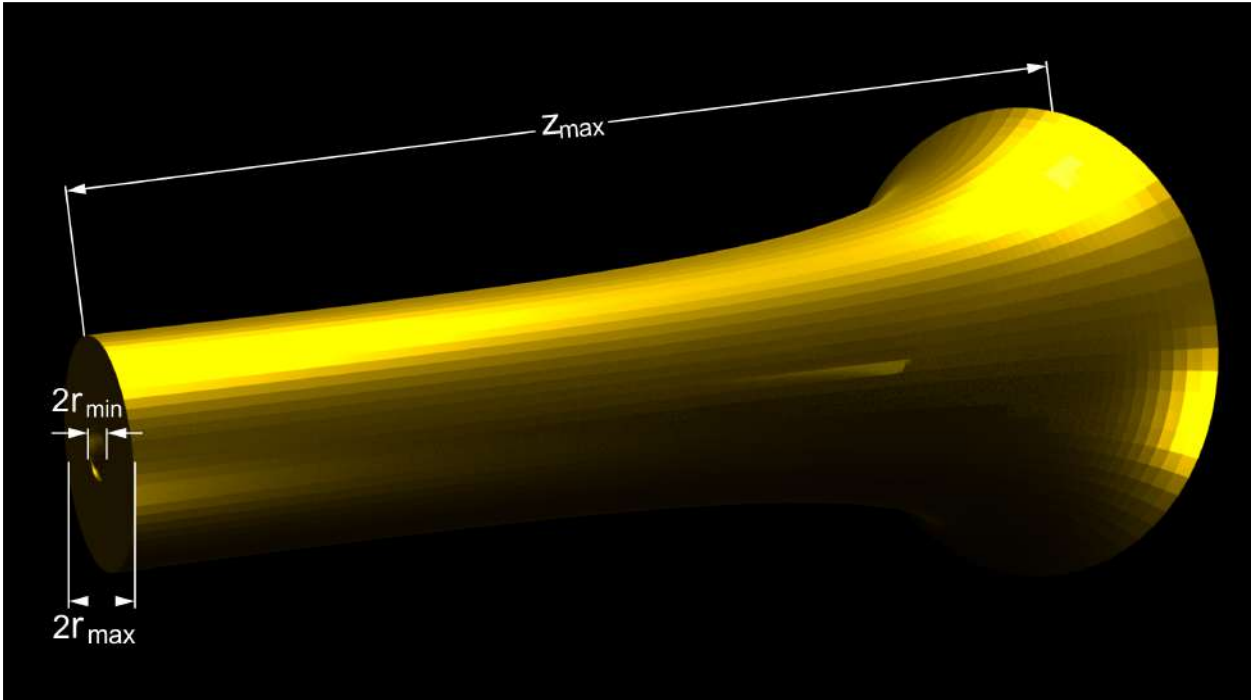the transformation give us a flared end of the cylinder as shown in Fig. C-2

Figure C-2.: Trumpet formed from the transformation defined in the Eq. C-13

the metric tensor can be defined by

$$
g = \begin{pmatrix} \Delta_r^2 \mathcal{Z}^{-2\lambda} & 0 & \Delta_r \Delta_z \mathcal{Z}^{-2\lambda-1} \lambda\, r \\ 0 & \Delta_\theta^2 \mathcal{Z}^{-2\lambda} r^2 & 0 \\ \Delta_r \Delta_z \mathcal{Z}^{-2\lambda-1} \lambda\, r & 0 & \Delta_z^2 \frac{\mathcal{Z}^{-2\lambda}\lambda^2 r^2 + \mathcal{Z}^2}{\mathcal{Z}^2} \end{pmatrix} \quad , \tag{C-17}
$$

its inverse

$$
g = \begin{pmatrix} \frac{\mathcal{Z}^{2\lambda+2}+\lambda^2 r^2}{\Delta_r^2 \mathcal{Z}^2} & 0 & \frac{-r\lambda}{\Delta_r \Delta_z \mathcal{Z}} \\ 0 & \frac{\mathcal{Z}^{2\lambda}}{\Delta_\theta^2 r^2} & 0 \\ \frac{-r\lambda}{\Delta_r \Delta_z \mathcal{Z}} & 0 & \frac{1}{\Delta_z^2} \end{pmatrix} \quad , \tag{C-18}
$$

the determinant of the metric tensor reads,

$$
g = \frac{r^2}{\mathcal{Z}^{4\lambda}} \Delta_r^2 \Delta_\theta^2 \Delta_z^2 \, , \tag{C-19}
$$

and the Christoffel symbols are

$$
\begin{aligned}
\Gamma_{rz}^r &= \left(\frac{\Delta_r \Delta_z}{\Delta_r} \right) \frac{\lambda}{\mathcal{Z}} = \Gamma_{zr}^r, \quad \Gamma_{zz}^r = \left(\frac{\Delta_z \Delta_z}{\Delta_r} \right) \frac{r\lambda(\lambda+1)}{\mathcal{Z}^2}, \\
\Gamma_{z\theta}^\theta &= \left(\frac{\Delta_z \Delta_\theta}{\Delta_\theta} \right) \frac{\lambda}{\mathcal{Z}^2} = \Gamma_{\theta z}^\theta, \quad \Gamma_{\theta\theta}^r = \left(\frac{\Delta_\theta \Delta_\theta}{\Delta_r} \right) (-r), \quad \Gamma_{r\theta}^\theta = \left(\frac{\Delta_r \Delta_\theta}{\Delta_\theta} \right) \frac{1}{r} = \Gamma_{\theta r}^\theta .
\end{aligned} \tag{C-20}
$$

C.4. Torus

The simulations done inside a torus required the following transformation

$$
\begin{aligned}
x &= (R + r\cos(\phi))\cos(\theta) \\
y &= (R + r\cos(\phi)))\sin(\theta) \quad . \\
z &= r\sin(\phi)
\end{aligned} \tag{C-21}
$$

In this case, the discrete-continuous transformation is

$$
\begin{aligned}
r &= i_r \Delta_r & \text{(C-22)} \\
\theta &= i_\theta \Delta_\theta & \text{(C-23)} \\
\phi &= i_\phi \Delta_\phi & \text{(C-24)}
\end{aligned}
$$

where $\Delta_r = r_{max}/L_r$, $\Delta_\theta = 2\pi/L_\theta$ and $\Delta_\phi = 2\pi/L_\phi$. The resulting Torus is shown in Fig. C-3
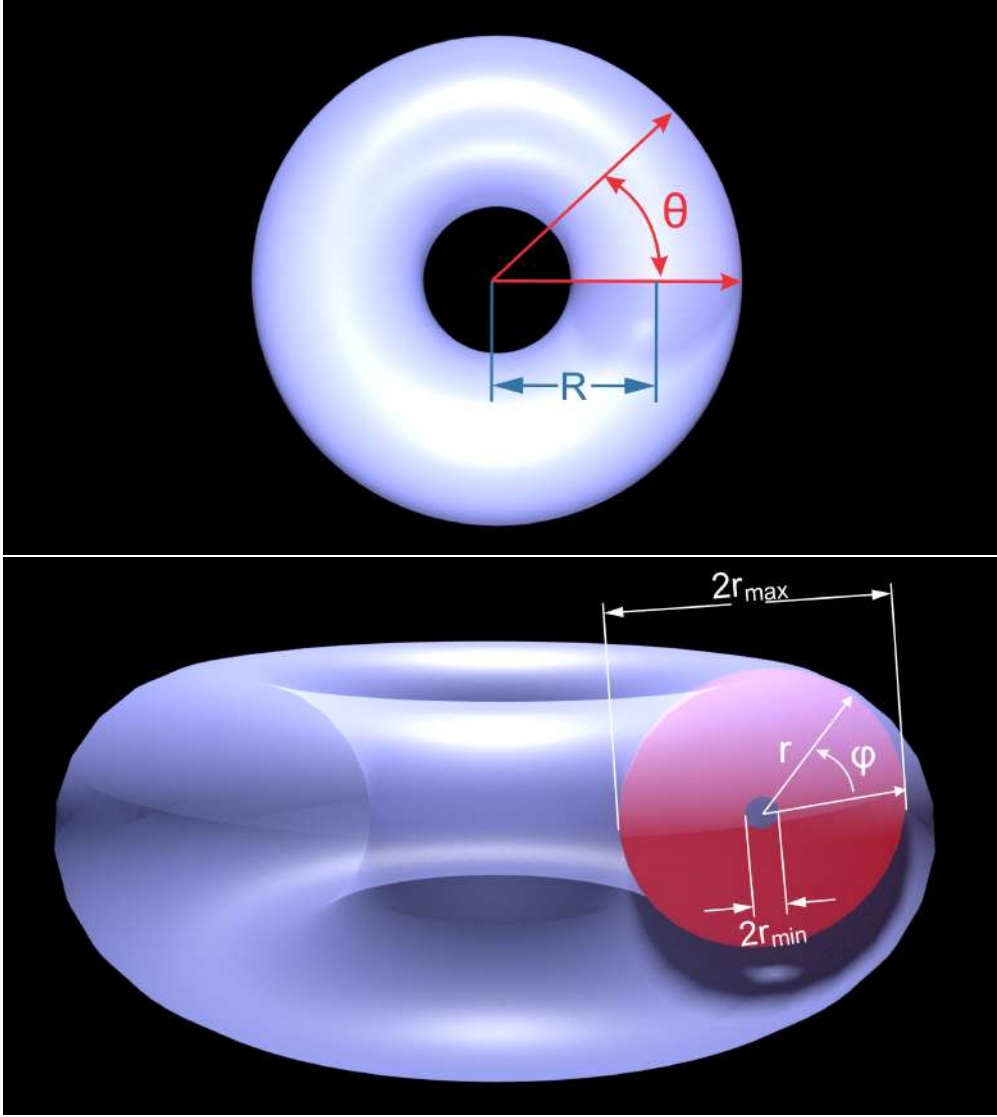
Figure C-3.: Torus formed by the transformation defined by the Eq. C-21

the resulting metric tensor for these coordinates is

$$g = \begin{pmatrix} \Delta_r^2 & 0 & 0 \\ 0 & \Delta_\theta^2 \left(R + r\cos(\phi) \right)^2 & 0 \\ 0 & 0 & \Delta_\phi^2 r^2 \end{pmatrix} \quad , \tag{C-25}$$

and its inverse

$$g = \begin{pmatrix} \frac{1}{\Delta_r^2} & 0 & 0 \\ 0 & \frac{1}{\Delta_\theta^2 (R + r\cos(\phi))^2} & 0 \\ 0 & 0 & \frac{1}{\Delta_\phi^2 r^2} \end{pmatrix} \quad , \tag{C-26}$$

the determinant reads,

$$g = r^2 \left(R + r \cos(\phi)\right)^2 \Delta_r^2 \Delta_\theta^2 \Delta_\phi^2,$$ (C-27)

and the non-zero Christoffel symbols are

$$\Gamma_{\theta\theta}^r = \left(\frac{\Delta_\theta \Delta_\theta}{\Delta_r}\right)(R + r \cos(\phi))\cos(\phi), \quad \Gamma_{\phi\phi}^r = \left(\frac{\Delta_\phi \Delta_\phi}{\Delta_r}\right)(-r),$$

$$\Gamma_{r\theta}^\theta = \left(\frac{\Delta_r \Delta_\theta}{\Delta_\theta}\right)\frac{\cos(\phi)}{(R + r \cos(\phi))} = \Gamma_{\theta r}^\theta, \quad \Gamma_{\theta\phi}^\theta = \left(\frac{\Delta_\phi \Delta_\theta}{\Delta_\theta}\right)\frac{-\sin(\phi)r}{(R + r \cos(\phi))} = \Gamma_{\phi\theta}^\theta,$$ (C-28)

$$\Gamma_{r\phi}^\phi = \left(\frac{\Delta_r \Delta_\phi}{\Delta_\phi}\right)\frac{1}{r} = \Gamma_{\phi r}^\phi, \quad \Gamma_\phi^{\theta\theta} = \left(\frac{\Delta_\theta \Delta_\theta}{\Delta_\phi}\right)\frac{(R + r \cos(\phi))\sin(\phi)}{r}.$$

C.5. Cochlea

The coordinates transformation we proposed to model the geometry of the cochlea is given by the set of equations

$$x = \cos(\theta)\left(R - a\theta + r \cos(\phi)(1 + \cos(\phi))\cos\left(\frac{\theta}{F}\right)\right)$$

$$y = \sin(\theta)\left(R - a\theta + r \cos(\phi)(1 + \cos(\phi))\cos\left(\frac{\theta}{F}\right)\right)$$ (C-29)

$$z = r \sin(\phi)(1 + \cos(\phi))\cos\left(\frac{\theta}{F}\right) + A\theta$$

the parameter values are:

$$\begin{aligned} A &= 0.2366\,\text{mm} \\ a &= 0.1648\,\text{mm} \\ R &= 2.8125\,\text{mm} \\ F &= 18.67 \end{aligned}$$ (C-30)

the second transformation in this case is

$$r = i_r \Delta_r + r_{min}$$ (C-31)
$$\theta = i_\theta \Delta_\theta$$ (C-32)
$$\phi = i_\phi \Delta_\phi - \pi$$ (C-33)

where $\Delta_r = (r_{max} - r_{min})/L_r$, $\Delta_\theta = 5\pi/L_\theta$, $\Delta_\phi = 2\pi/L_\phi$, $r_{min} = 0.09$ and $r_{max} = 0.9$ the obtained geometry is shown in Fig. C-4
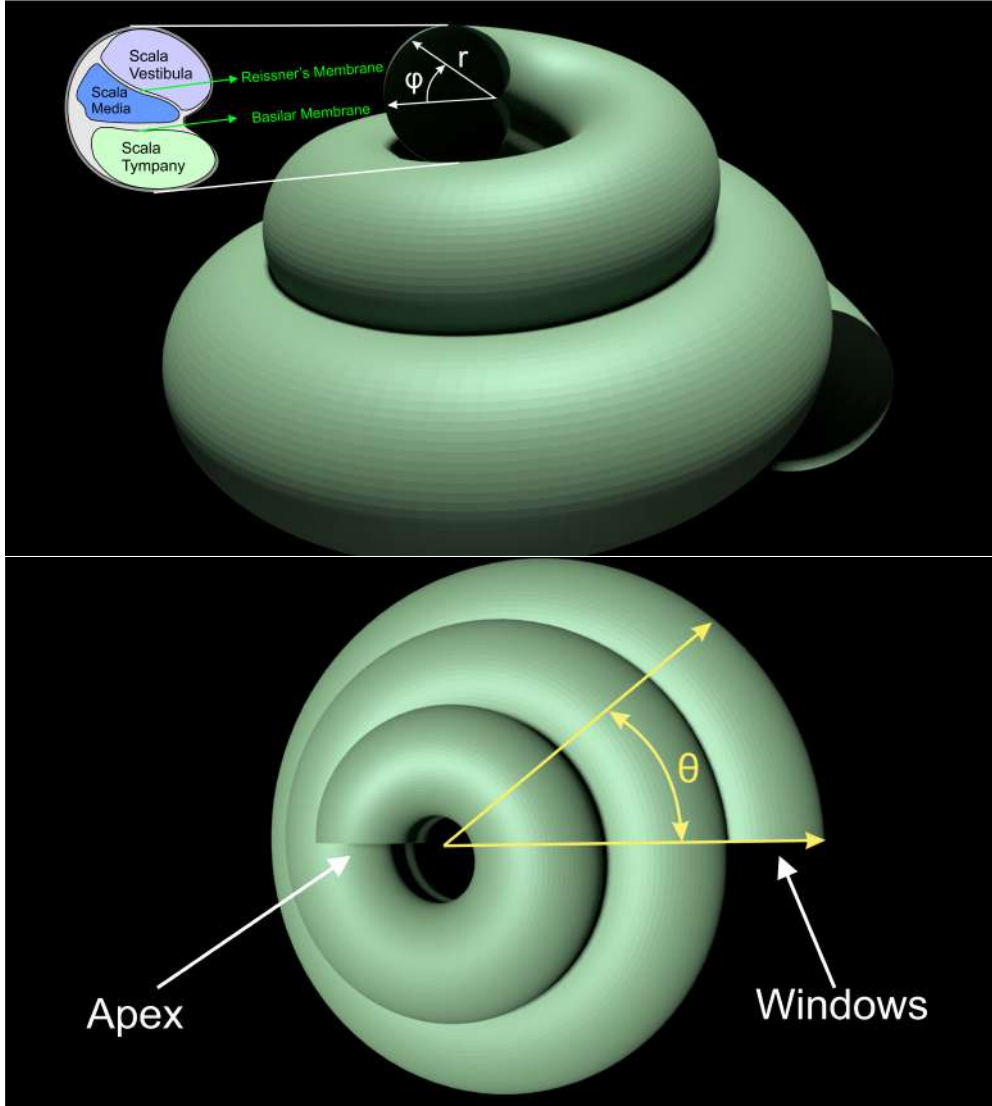
Figure C-4.: Cochlea's Geometry generated from Eq. C-29

The components of the metric tensor are

$$g_{11} = \left(\cos \left(\frac{\theta}{F} \right) \right)^2 (1 + \cos(\phi))^2 \tag{C-34}$$

$$g_{12} = g_{21} = \frac{1 + \cos(\phi)}{F} \cos \left(\frac{\theta}{F} \right)$$
$$\left(-r(1 + \cos(\phi)) \sin \left(\frac{\theta}{F} \right) + F(A \sin(\phi) - a \cos(\phi)) \right) \tag{C-35}$$

$$g_{13} = g_{31} = - \left(\cos \left(\frac{\theta}{F} \right) \right)^2 \sin(\phi) r (1 + \cos(\phi)) \tag{C-36}$$

$$g_{22} = \frac{1}{F^2} \left(r^2 \left(1 + \cos\left(\phi\right)\right)^2 \left(F \cos\left(\phi\right) - 1\right) \left(F \cos\left(\phi\right) + 1\right) \left(\cos\left(\frac{\theta}{F}\right)\right)^2 \right.$$
$$+ 2\,rF^2 \cos\left(\phi\right) \left(1 + \cos\left(\phi\right)\right) \left(-a\theta + R\right) \cos\left(\frac{\theta}{F}\right)$$
$$- 2\,rF \left(1 + \cos\left(\phi\right)\right) \left(A \sin\left(\phi\right) - a \cos\left(\phi\right)\right) \sin\left(\frac{\theta}{F}\right) + r^2 \left(\cos\left(\phi\right)\right)^2$$
$$\left. + 2 \cos\left(\phi\right) r^2 + \left(\left(\theta^2 + 1\right) a^2 - 2\,Ra\theta + A^2 + R^2\right) F^2 + r^2 \right)$$

(C-37)

$$g_{23} = g_{32} = \frac{r}{F} \left(r \sin\left(\phi\right) \left(1 + \cos\left(\phi\right)\right) \sin\left(\frac{\theta}{F}\right) \right.$$
$$\left. + 2 \left(A \left(\cos\left(\phi\right)\right)^2 + \left(\sin\left(\phi\right) a + A/2\right) \cos\left(\phi\right) + 1/2 \, \sin\left(\phi\right) a - A/2\right) F \right) \cos\left(\frac{\theta}{F}\right)$$

(C-38)

$$g_{33} = 2 \left(\cos\left(\frac{\theta}{F}\right)\right)^2 r^2 \left(1 + \cos\left(\phi\right)\right)$$

(C-39)

its inverse has the following components

$$g^{11} = \frac{1}{F^2 \left(1 + \cos\left(\phi\right)\right)^3 \left(\cos\left(\frac{\theta}{F}\right)\right)^2 \left(-a\theta + R + r \cos\left(\phi\right) \left(1 + \cos\left(\phi\right)\right) \cos\left(\frac{\theta}{F}\right)\right)^2}$$
$$\times \left(2\,r^2 \left(1 + \cos\left(\phi\right)\right)^2 \left(F^2 \left(\cos\left(\phi\right)\right)^2 - 1/2 \, \cos\left(\phi\right) - 1/2\right) \left(\cos\left(\frac{\theta}{F}\right)\right)^2 \right.$$
$$+ 4\,rF^2 \cos\left(\phi\right) \left(1 + \cos\left(\phi\right)\right) \left(-a\theta + R\right) \cos\left(\frac{\theta}{F}\right)$$
$$- \left(-4\,a \left(\cos\left(\phi\right)\right)^2 + 4 \left(A \sin\left(\phi\right) - a/2\right) \cos\left(\phi\right) + 2\,A \sin\left(\phi\right) + 2\,a\right) F\,r \left(1 + \cos\left(\phi\right)\right) \sin\left(\frac{\theta}{F}\right)$$
$$+ \left(r^2 + \left(-4\,A^2 + 4\,a^2\right) F^2\right) \left(\cos\left(\phi\right)\right)^3 + \left(-8\,AF^2 \sin\left(\phi\right) a + 3\,r^2\right) \left(\cos\left(\phi\right)\right)^2$$
$$+ \left(3\,r^2 + \left(3\,A^2 - 3\,a^2\right) F^2\right) \cos\left(\phi\right) + 2\,AF^2 \sin\left(\phi\right) a + r^2$$
$$\left. + \left(\left(2\,\theta^2 + 1\right) a^2 - 4\,Ra\theta + A^2 + 2\,R^2\right) F^2 \right)$$

(C-40)

$$g^{12} = \frac{r \left(1 + \cos\left(\phi\right)\right)^2 \sin\left(\frac{\theta}{F}\right) - \left(-2\,a \left(\cos\left(\phi\right)\right)^2 + 2 \left(A \sin\left(\phi\right) - a/2\right) \cos\left(\phi\right) + A \sin\left(\phi\right) + a\right) F}{F \left(1 + \cos\left(\phi\right)\right)^2 \left(\cos\left(\frac{\theta}{F}\right)\right) \left(-a\theta + R + r \cos\left(\phi\right) \left(1 + \cos\left(\phi\right)\right) \cos\left(\frac{\theta}{F}\right)\right)^2}$$

$$(C\text{-}41)$$

$$g^{13} = \frac{1}{rF\,(1+\cos{(\phi)})^3\left(\cos\left(\frac{\theta}{F}\right)\right)^2\left(-a\theta+R+r\cos{(\phi)}\,(1+\cos{(\phi)})\cos\left(\frac{\theta}{F}\right)\right)^2}$$

$$\times\left(r^2F\,(\cos{(\phi)})^2\sin{(\phi)}\,(1+\cos{(\phi)})^2\left(\cos\left(\frac{\theta}{F}\right)\right)^2\right.$$

$$+2\,rF\,\cos{(\phi)}\sin{(\phi)}\,(1+\cos{(\phi)})\,(-a\theta+R)\cos\left(\frac{\theta}{F}\right)$$

$$-r\,(1+\cos{(\phi)})^2\,(A\cos{(\phi)}+\sin{(\phi)}\,a)\sin\left(\frac{\theta}{F}\right)$$

$$+\Big(-4\,Aa\,(\cos{(\phi)})^3+2\,\big((A^2-a^2)\sin{(\phi)}-Aa\big)(\cos{(\phi)})^2$$

$$+2\,\big((1/2\,A^2-1/2\,a^2)\sin{(\phi)}+3/2\,Aa\big)\cos{(\phi)}$$

$$\left.+2\,\big((1/2\,\theta^2+1/2)\,a^2-Ra\theta+1/2\,R^2\big)\sin{(\phi)}+Aa\Big)F\right)$$

$$(C\text{-}42)$$

$$g^{22} = \left(-a\theta+R+r\cos{(\phi)}\,(1+\cos{(\phi)})\cos\left(\frac{\theta}{F}\right)\right)^{-2} \tag{C-43}$$

$$g^{23} = \frac{-A\cos{(\phi)}-\sin{(\phi)}\,a}{r\,(1+\cos{(\phi)})\cos\left(\frac{\theta}{F}\right)\left(-a\theta+R+r\cos{(\phi)}\,(1+\cos{(\phi)})\cos\left(\frac{\theta}{F}\right)\right)^2} \tag{C-44}$$

$$g^{33} = \frac{1}{r^2\,(1+\cos{(\phi)})^2\left(\cos\left(\frac{\theta}{F}\right)\right)^2\left(-a\theta+R+r\cos{(\phi)}\,(1+\cos{(\phi)})\cos\left(\frac{\theta}{F}\right)\right)^2}$$

$$\times\left(r^2\,(\cos{(\phi)})^2\,(1+\cos{(\phi)})^2\left(\cos\left(\frac{\theta}{F}\right)\right)^2\right.$$

$$+2\,r\cos{(\phi)}\,(1+\cos{(\phi)})\,(-a\theta+R)\cos\left(\frac{\theta}{F}\right)$$

$$\left.+(A^2-a^2)\,(\cos{(\phi)})^2+2\,A\cos{(\phi)}\sin{(\phi)}\,a+(\theta^2+1)\,a^2-2\,Ra\theta+R^2\right)$$

$$(C\text{-}45)$$

the determinant of the metric tensor is

$$g = r^2\,(1+\cos{(\phi)})^4\left(\cos\left(\frac{\theta}{F}\right)\right)^4\left(-a\theta+R+r\,\cos{(\phi)}\,(1+\cos{(\phi)})\cos\left(\frac{\theta}{F}\right)\right)^2\Delta_r{}^2\Delta_\theta{}^2\Delta_\phi{}^2$$

$$(C\text{-}46)$$

Finally, the Christoffel symbols are the following

$$\Gamma^r_{r\theta} = \frac{\Delta_\theta}{(1+\cos(\phi))\,F\cos\left(\frac{\theta}{F}\right)\left(-r\cos(\phi)(1+\cos(\phi))\cos\left(\frac{\theta}{F}\right)+a\theta-R\right)}$$
$$\times\left(\cos(\phi)\left(-(\cos(\phi))^2\,a+(A\sin(\phi)-a/2)\cos(\phi)+1/2\,A\sin(\phi)+a/2\right)F\,\cos\left(\frac{\theta}{F}\right)\right.$$
$$\left.-1/2\,\sin\left(\frac{\theta}{F}\right)(1+\cos(\phi))(a\theta-R)\right),$$

$$\text{(C-47)}$$

$$\Gamma^r_{\theta\theta} = -4\,\frac{\Delta_\theta{}^2}{\Delta_r\,(1+\cos(\phi))^2\,F^2\cos\left(\frac{\theta}{F}\right)\left(-r\,\cos(\phi)(1+\cos(\phi))\cos\left(\frac{\theta}{F}\right)+a\theta-R\right)}$$
$$\times\left(-1/2\,\cos(\phi)(1+\cos(\phi))^3\left(F^2(\cos(\phi))^2-1/2\,F^2\cos(\phi)-1/2\right)r^2\left(\cos\left(\frac{\theta}{F}\right)\right)^2\right.$$
$$+(1+\cos(\phi))^2\left(F^2(\cos(\phi))^2-1/2\,F^2\cos(\phi)+1/4\right)(a\theta-R)\,r\cos\left(\frac{\theta}{F}\right)$$
$$+(1+\cos(\phi))\,F\,\left(-(\cos(\phi))^3\,a+(A\sin(\phi)-a/2)(\cos(\phi))^2+1/2\,\cos(\phi)\,A\sin(\phi)-a/2\right)$$
$$r\sin\left(\frac{\theta}{F}\right)-1/2\,(\cos(\phi))^4\,r^2-3/2\,(\cos(\phi))^3\,r^2$$
$$+\left(-3/2\,r^2-1/2\left((\theta^2+2)\,a^2-2\,Ra\theta+R^2\right)F^2\right)(\cos(\phi))^2$$
$$+\left(A\sin(\phi)\,aF^2-1/2\,r^2-1/4\left((\theta^2+2)\,a^2-2\,Ra\theta+R^2\right)F^2\right)\cos(\phi)$$
$$+1/2\left(A\sin(\phi)\,a+(1/2\,\theta^2+1)\,a^2-Ra\theta+1/2\,R^2\right)F^2\right)$$

$$\text{(C-48)}$$

$$\Gamma^r_{\theta\phi} = 4\,\frac{\Delta_\theta\Delta_\phi\,(\cos(\phi)+1/2)\,r}{\Delta_r\,(1+\cos(\phi))\,F\left(-r\cos(\phi)(1+\cos(\phi))\cos\left(\frac{\theta}{F}\right)+a\theta-R\right)}$$
$$\left(1/2\sin(\phi)\,r\Delta_r\,(1+\cos(\phi))\sin\left(\frac{\theta}{F}\right)\right.\qquad\qquad\text{(C-49)}$$
$$\left.+\left(A(\cos(\phi))^2+(\sin(\phi)\,a-A/2)\cos(\phi)-1/2\sin(\phi)\,a-A/2\right)F\right)$$

$$\Gamma^r_{\phi\phi} = -3\,\frac{\Delta_\phi{}^2\,r}{\Delta_r(1+\cos(\phi))},\qquad\qquad\qquad\qquad\qquad\text{(C-50)}$$

$$\Gamma^\theta_{r\theta} = \frac{(1+\cos(\phi))\,\Delta_r\cos(\phi)\cos\left(\frac{\theta}{F}\right)}{\left(-a\theta+R+r\cos(\phi)(1+\cos(\phi))\cos\left(\frac{\theta}{F}\right)\right)}\qquad\qquad\text{(C-51)}$$

$$\Gamma^{\theta}_{\theta\theta} = -2\frac{\Delta_{\theta}\left(\Delta_r \cos\left(\phi\right) r \left(1+\cos\left(\phi\right)\right)\sin\left(\frac{\theta}{F}\right) + aF\right)}{F\left(-a\theta + R + r\cos\left(\phi\right)\left(1+\cos\left(\phi\right)\right)\cos\left(\frac{\theta}{F}\right)\right)}, \tag{C-52}$$

$$\Gamma^{\theta}_{\theta\phi} = -\frac{2\sin\left(\phi\right)\left(\cos\left(\phi\right)+1/2\right) r \Delta_{\phi} \cos\left(\frac{\theta}{F}\right)}{\left(-a\theta + R + r\cos\left(\phi\right)\left(1+\cos\left(\phi\right)\right)\cos\left(\frac{\theta}{F}\right)\right)} \tag{C-53}$$

$$\Gamma^{\phi}_{r\theta} = \frac{\Delta_{\theta}\left(A\cos\left(\phi\right)+\sin\left(\phi\right)a\right)\cos\left(\phi\right)}{\Delta_{\phi} r \left(-r\cos\left(\phi\right)\left(1+\cos\left(\phi\right)\right)\cos\left(\frac{\theta}{F}\right)+a\theta - R\right)}, \tag{C-54}$$

$$\Gamma^{\phi}_{r\phi} = r^{-1} \tag{C-55}$$

$$\Gamma^{\phi}_{\theta\theta} = -2\frac{\Delta_{\theta}{}^2}{\Delta_{\phi}\left(1+\cos\left(\phi\right)\right) F r \cos\left(\frac{\theta}{F}\right)\left(-r\cos\left(\phi\right)\left(1+\cos\left(\phi\right)\right)\cos\left(\frac{\theta}{F}\right)+a\theta - R\right)}$$
$$\left(1/2\left(\cos\left(\phi\right)\right)^2 \sin\left(\phi\right) r^2 F \left(1+\cos\left(\phi\right)\right)^2 \left(\cos\left(\frac{\theta}{F}\right)\right)^2\right.$$
$$- \cos\left(\phi\right)\sin\left(\phi\right) r F \left(1+\cos\left(\phi\right)\right)\left(a\theta - R\right)\cos\left(\frac{\theta}{F}\right) \tag{C-56}$$
$$+ \cos\left(\phi\right) r \left(1+\cos\left(\phi\right)\right)\left(A\cos\left(\phi\right)+\sin\left(\phi\right)a\right)\sin\left(\frac{\theta}{F}\right)$$
$$\left.+ F\left(\cos\left(\phi\right) Aa + 1/2\sin\left(\phi\right)\left(\left(\theta^2+2\right)a^2 - 2Ra\theta + R^2\right)\right)\right),$$

$$\Gamma^{\phi}_{\theta\phi} = -2\frac{\Delta_{\theta}}{\left(1+\cos\left(\phi\right)\right) F \cos\left(\frac{\theta}{F}\right)\left(-r\cos\left(\phi\right)\left(1+\cos\left(\phi\right)\right)\cos\left(\frac{\theta}{F}\right)+a\theta - R\right)}$$
$$\left(\left(-1/2\cos\left(\phi\right) r \left(1+\cos\left(\phi\right)\right)^2 \sin\left(\frac{\theta}{F}\right)\right.\right.$$
$$\left.+ \left(\cos\left(\phi\right)+1/2\right) F \left(\cos\left(\phi\right) A\sin\left(\phi\right)-\left(\cos\left(\phi\right)\right)^2 a + a\right)\right)\cos\left(\frac{\theta}{F}\right) \tag{C-57}$$
$$\left.+ 1/2\sin\left(\frac{\theta}{F}\right)\left(1+\cos\left(\phi\right)\right)\left(a\theta - R\right)\right),$$

$$\Gamma^{\phi}_{\phi\phi} = -2\frac{\Delta_{\phi}\sin\left(\phi\right)}{1+\cos\left(\phi\right)} \tag{C-58}$$

Bibliografía

[1] John J Guinan, Alec Salt, Mary Ann Cheatham, and Mary Ann Cheatham. Progress in cochlear physiology after Békésy. *Hearing research*, 293(1-2):12–20, nov 2012.

[2] Georg von Békésy. Georg von Békésy - Nobel Lecture: Concerning the Pleasures of Observing, and the Mechanics of the Inner Ear.

[3] Elizabeth S Olson, Hendrikus Duifhuis, and Charles R Steele. Von Békésy and cochlear mechanics. *Hearing research*, 293(1-2):31–43, nov 2012.

[4] John J Guinan and Jr. New insights into cochlear amplification. *Biophysical journal*, 105(4):839–40, aug 2013.

[5] Katharina Braun, Frank Böhnke, and Thomas Stark. Three-dimensional representation of the human cochlea using micro-computed tomography data: Presenting an anatomical model for further numerical calculations. *Acta Oto-Laryngologica*, 132(6):603–613, jun 2012.

[6] P. L. Bhatnagar, E. P. Gross, and M. Krook. A model for collision processes in gases. I. Small amplitude processes in charged and neutral one-component systems. *Physical Review*, 94(3):511–525, may 1954.

[7] Francesca Nannelli and Sauro Succi. The lattice Boltzmann equation on irregular lattices. *Journal of Statistical Physics*, 68(3-4):401–407, aug 1992.

[8] Xiaoyi He and Gary D. Doolen. Lattice Boltzmann method on a curvilinear coordinate system: Vortex shedding behind a circular cylinder. *Physical Review E*, 56(1):434–440, jul 1997.

[9] Q. Li, Y. L. He, G. H. Tang, and W. Q. Tao. Improved axisymmetric lattice Boltzmann scheme. *Physical Review E - Statistical, Nonlinear, and Soft Matter Physics*, 2010.

[10] S. A. Reijers, H. Gelderblom, and F. Toschi. Axisymmetric multiphase lattice Boltzmann method for generic equations of state. *Journal of Computational Science*, 2016.

[11] Ljubomir Budinski. Lattice Boltzmann method for 2D flows in curvilinear coordinates. *Journal of Hydroinformatics*, 2012.

[12] M. Mendoza. Relativistic Fluid Dynamics in Complex Systems, 2012.

[13] H Rask-Andersen, W Liu, E Erixon, A Kinnefors, K Pfaller, A Schrott-Fischer, and R Glueckert. Human cochlea: Anatomical characteristics and their relevance for cochlear implantation. *Anatomical Record*, 295(11):1791–1811, 2012.

[14] L.-J. Ren, C Hua, G.-H. Ding, L Yang, P.-D. Dai, and T.-Y. Zhang. Hydrodynamic modeling of cochlea and numerical simulation for cochlear traveling wave with consideration of fluid-structure interaction. *Journal of Hydrodynamics*, 25(2):167–173, 2013.

[15] Richard P Beyer, Richard P., and Jr. A computational model of the cochlea using the immersed boundary method. *Journal of Computational Physics*, 98(1):145–162, jan 1992.

[16] Anand A. Parthasarathi, Karl Grosh, and Alfred L. Nuttall. Three-dimensional numerical modeling for global cochlear dynamics. *http://dx.doi.org/10.1121/1.428352*, dec 1999.

[17] E. Givelberg, J. Bunn, and M. Rajan. Detailed Simulation of the Cochlea: Recent Progress Using Large Shared Memory Parallel Computers. jan 2001.

[18] Hongxue Cai, Daphne Manoussaki, and Richard Chadwick. Effects of coiling on the micromechanics of the mammalian cochlea. *Journal of the Royal Society, Interface*, 2(4):341–8, sep 2005.

[19] Elisabeth Edom, Dominik Obrist, Rolf Henniger, Leonhard Kleiser, Jae Hoon Sim, and Alexander M. Huber. The effect of rocking stapes motions on the cochlear fluid flow and on the basilar membrane motion. *The Journal of the Acoustical Society of America*, 134(5):3749–3758, nov 2013.

[20] Liu Jie Ren, Cheng Hua, Guang Hong Ding, Lin Yang, Pei Dong Dai, and Tian Yu Zhang. Hydrodynamic modeling of cochlea and numerical simulation for cochlear traveling wave with consideration of fluid-structure interaction. *Journal of Hydrodynamics*, 25(2):167–173, apr 2013.

[21] Doron Sabo, Oded Barzelay, Shlomo Weiss, and Miriam Furst. Fast evaluation of a time-domain non-linear cochlear model on GPUs. *Journal of Computational Physics*, 265:97–112, may 2014.

[22] X He and L.-S. Luo. Theory of the lattice Boltzmann method: From the Boltzmann equation to the lattice Boltzmann equation. *Physical Review E - Statistical Physics, Plasmas, Fluids, and Related Interdisciplinary Topics*, 56(6):6811–6817, 1997.

[23] D A Wolf-Gladrow. *Lattice-Gas Cellular Automata and Lattice Boltzmann Models: An Introduction*. Lecture Notes in Mathematics. Springer Berlin Heidelberg, 2004.

[24] S. Succi. *The lattice Boltzmann equation for fluid dynamics and beyond.* Clarendon Press, 2001.

[25] A J Wagner and K Strand. Fluctuating lattice Boltzmann method for the diffusion equation. *Physical Review E - Statistical, Nonlinear, and Soft Matter Physics*, 94(3), 2016.

[26] Yan Guangwu. A Lattice Boltzmann Equation for Waves. *Journal of Computational Physics*, 161(1):61–69, jun 2000.

[27] M. Mendoza and J. D. Muñoz. Three-dimensional lattice Boltzmann model for electrodynamics. *Physical Review E*, 82(5):056708, nov 2010.

[28] B. Chopard, P.O. Luthi, and J.-F. Wagen. Lattice Boltzmann method for wave propagation in urban microcells. *IEE Proceedings - Microwaves, Antennas and Propagation*, 144(4):251, 1997.

[29] Yanbing Li and Xiaowen Shan. Lattice Boltzmann method for adiabatic acoustics. *Philosophical transactions. Series A, Mathematical, physical, and engineering sciences*, 369(1944):2371–80, jun 2011.

[30] Chenghai Sun, Franck Pérot, Raoyang Zhang, Phoi Tack Lew, Adrien Mann, Vinit Gupta, David M. Freed, Ilya Staroselsky, and Hudong Chen. Lattice Boltzmann formulation for flows with acoustic porous media, oct 2015.

[31] Erik M. Salomons, Walter J. A. Lohman, and Han Zhou. Simulation of Sound Waves Using the Lattice Boltzmann Method for Fluid Flow: Benchmark Cases for Outdoor Sound Propagation. *PLOS ONE*, 11(1):e0147206, jan 2016.

[32] Bastien Chopard. Cellular Automata Modeling of Physical Systems. In *Encyclopedia of Complexity and Systems Science*, pages 865–892. Springer New York, New York, NY, 2009.

[33] W C Elmore, W C Elmore, and M A Heald. *Physics of Waves.* Dover Books on Physics Series. Dover Publications, 1969.

[34] Timm Krüger, Halim Kusumaatmaja, Alexandr Kuzmin, Orest Shardt, Goncalo Silva, and Erlend Magnus Viggen. *The Lattice Boltzmann Method.* Graduate Texts in Physics. Springer International Publishing, Cham, 2017.

[35] Xiaoyi He and Li-Shi Luo. Some Progress in Lattice Boltzmann Method. Part I. Nonuniform Mesh Grids. *Journal of Computational Physics*, 129(2):357–363, dec 1996.

[36] Olga Filippova and Dieter Hänel. Grid Refinement for Lattice-BGK Models. *Journal of Computational Physics*, 147(1):219–228, nov 1998.

[37] J.-D. Debus, M. Mendoza, and H. J. Herrmann. Dean instability in double-curved channels. *Physical Review E*, 90(5):053308, nov 2014.

[38] M. Mendoza, S. Succi, and H. J. Herrmann. Flow Through Randomly Curved Manifolds. *Scientific Reports*, 3(1):3106, dec 2013.

[39] J.-D. Debus, M. Mendoza, S. Succi, and H. J. Herrmann. Energy dissipation in flows through curved spaces. *Scientific Reports*, 7:42350, feb 2017.

[40] Derek F. Lawden. *Introduction to tensor calculus, relativity, and cosmology*. Dover Publications, 2002.

[41] Zhaoli Guo, Chuguang Zheng, and Baochang Shi. Discrete lattice effects on the forcing term in the lattice Boltzmann method. *Physical Review E*, 65(4):046308, apr 2002.

[42] Thomas D. Rossing, Paul (Paul A.) Wheeler, and F. Richard. Moore. *The science of sound*. Addison Wesley, 2002.

[43] Julien Favier, Alistair Revell, and Alfredo Pinelli. A Lattice Boltzmann Immersed Boundary method to simulate the fluid interaction with moving and slender flexible objects. *Journal of Computational Physics*, 261:145–161, 2014.

[44] J. H. (John Harvard) Biles. *The design and construction of ships. vol II, Stability, resistance, propulsion and oscillations of ships*. Salzwasser-Verlag, 2009.